Development of coherently synthesized two-color electro-optic frequency combs and its application to absolute distance measurement

Li Runmin

The University of Electro-Communication

Department of Engineering Science

Doctor of Philosophy

SEPTEMBER 2023

Development of coherently synthesized two-color electro-optic frequency combs and its application to absolute distance measurement

Doctoral dissertation review committee:

Chair:

Prof. Kaoru MINOSHIMA, Advisor

Members:

Prof. Masayuki KATSURAGAWA

Prof. Mitsuru MUSHA

Prof. Eriko WATANABE

Assis. Prof. Akifumi ASAHARA

論文の和文概要

光周波数コム（OFC）は、コヒーレントかつ等間隔な多数の離散的周波数モードを生成可能なレーザー光源である。同時に、時間領域においては、高強度な超短パルスであり、そのパルス間隔はコムのモード間隔の逆数に等しい。OFC の魅力的な特性により、その発生と広範な分野に及ぶ応用研究が盛んである。中でも、電気光学変調コム（EO コム）は、光周波数コム発生法として広く用いられており、コム間隔の広範囲かつ高速な掃引が可能な利点がある。同時に、EO コムは、一般的に、自由空間光学系を持たないため、構成が単純で高いロバスト性を持つ。従って、EO コムは、高精度距離測定、光通信、テラヘルツ波発生などの多くの応用分野で期待されている。

本論文では、新規な EO コムの発生と応用について研究した。発生においては、2 色 EO コムのコヒーレント合成手法による広帯域スペクトルと低位相雑音の実現法を提案して、実証した。特に、EO コムの原理的課題である、モード数の増加とともに増大する蓄積位相ノイズ（accumulated phase noise）を、コヒーレント合成によって抑制する手法を、本研究によって初めて提案・実証した。

さらに、発生されたコヒーレント合成による2色EOコムを距離測定に適用し、低ノイズかつ広帯域な光源の特性を活用することで、干渉計測の位相の繰り返し不定性を回避して距離を決定できる非曖昧範囲（non-ambiguity range）を拡大して、高精度絶対距離測定の長距離化手法を実現した。本論文の主たる内容は以下の通り。

1. 本研究では、離れた 2 波長の連続波レーザーから発生される2つの EO コムを合成することで、コヒーレント合成 2 色 EO コムを生成した。変調器のドライブ信号を由来とする蓄積位相ノイズは、コヒーレント合成によって大きく抑制される。実際に、コヒーレント合成 2 色 EO コムと既存法である 1 色の EO コムとの位相ノイズ比較によって、本手法のノイズ抑制原理を実験的に実証した。これは、蓄積ノイズのコヒーレント合成による抑制を示した初めての結果である。

さらに、EOコムの中心波長間隔を拡大することにより、スペクトル幅60 nmへと広帯域化されたコヒーレント合成 2 色 EO コムの発生を示した。最後に、開発したコヒーレント合成 2 色 EO コムを筐体に収め、安定性と可搬性を高めた。

2. 作成したコヒーレント合成2色EOコムを距離測定に応用した。まず、光ファイバ型干渉計を用いた距離測定系を構築し、性能評価を行った。短時間安定性、長時間安定性、線形性、デッドパス誤差、周期誤差について評価した。1 秒以上の長時間においてはファイバ長の揺らぎが制限要因となったが、ナノメートル精度と 10 kHz の高速測定レートが実現され、高速変位測定に適した系であることを示した。

3. 作成したコヒーレント合成2色EOコムを用いた自由空間干渉計による距離測定を行った。参照光路長の揺らぎの影響をキャンセルするためにモニタ光路を導入した。単一波長レーザー干渉計、合成波長干渉計、およびマイクロ波の位相測定による 3 種の距離測定を行った。構築したEOコム光源の広帯域性と低ノイズ性を活用することで、3種の測定結果を組み合わせることに成功し、非曖昧範囲（non-ambiguity range）を mm レベルに拡大した、ナノメートル精度の絶対距離測定が実現された。既存の確立された HeNe レーザー干渉計による連続変位測定との比較を行った結果、±25 nm 以下の測定不確かさが確認された。

以上のように、本研究によって、コヒーレント合成による広帯域かつ低ノイズな電気光学変調コムの発生を初めて示すとともに、その光源の利点を生かすことで、広範な応用性のある高精度長距離絶対計測を実証した。

ABSTRACT

Optical frequency combs (OFCs) are laser sources which are capable of generating discrete, equal-spaced and highly coherent longitudinal modes. In time domain, an OFC emits ultrashort pulses with high peak power, which repeat at a period that equals to the reciprocal of comb mode spacing. Attributing to these elegant and attractive characteristics of OFCs, a lot of efforts have been made to generate OFCs and to apply them in various fields. Electro-optic frequency comb (EO comb) is one of the popular methods to obtain optical frequency comb, which has the unique advantages of large tuning and high tuning speed of the comb spacing. Meanwhile, the EO combs usually have simple configuration and good robustness, attributing to the cavity-less structure. Hence EO combs have attracted a lot of interests in high-precision distance measurement, optical communication, terahertz wave generation, etc. In this thesis, coherently synthesized two-color EO comb with broad spectrum and low phase noise is proposed and demonstrated. The suppression of accumulated phase noise of the comb modes through coherent synthesis is demonstrated for the first time. High precision absolute distance measurement is realized on the basic of the coherently synthesized two-color EO comb. The major contents in this thesis are summarized as follows:

1. Two EO combs with distinct center wavelengths are coherently synthesized, resulting in the generation of coherently synthesized two-color EO comb. The accumulated phase noise, which originates from the phase noise of driven signal, is greatly suppressed in the coherently synthesized two-color EO comb. This is experimentally verified by comparing the phase noise of comb modes in coherently synthesized two-color EO comb and conventional EO comb. To the best of my knowledge, this is the first demonstration of accumulated phase noise suppression through coherent synthesis. Broadband coherently synthesized two-color EO comb with spectrum range of 60 nm is demonstrated through increasing the center wavelength difference between the two EO combs. The coherently synthesized two-color EO comb is compactly integrated in a box.

2. The coherently synthesized two-color EO comb is applied to distance

measurement. This distance measurement system is based on a fiber type interferometer. The system performances are investigated, including the short-term stability, long-term stability, linearity, dead path error and cyclic error. Although the length fluctuation of fiber in the interferometer restricts the measurement with nanometer precision at > 1 s averaging time, this system is suitable to realize fast displacement measurement. Measurement with 10-kHz update rate has been achieved.

3. High precision absolute distance measurement is achieved based on the coherently synthesized two-color EO comb and a free space interferometer. Monitor arm is introduced to the system, so that the impact of path length fluctuations in the reference arm on the measurement can be ignored. Three methods are used to measure the distance under test, including single wavelength interferometry, synthetic wavelength technique and microwave phase detection. Benefiting from the low noise property of coherently synthesized two-color EO comb, combining of the three methods is realized and absolute distance measurement is demonstrated in consequence. This system is able to achieve nanometer precision with millimeter non-ambiguity range. Via comparing the measurement results with that from a HeNe interferometry, precision that less than ± 25 nm is realized.

KEY WORDS: Electro-optic comb; coherent synthesis; phase noise; distance measurement

Table of content

Chapter 1. Introduction

Optical frequency comb is one of the greatest advancements of laser after its invention, which was proposed at the end of the 20th century [1][2][3][4][5][6][7]. In 2005, John L. Hall from National Institute of Standards and Technology and Theodor W. Hänsch from Max Planck Institute for Quantum Optics were awarded the Nobel Prize in Physics for their contributions to optical frequency comb technology and precise spectroscopy [8][9]. The emergence of optical frequency comb has greatly promoted the development of many fields, such as spectroscopy, the transfer of optical time and frequency references to RF, the long-range transmission of time and frequency references, distance measurement, to name a few.

While the emergence of optical frequency comb technology has greatly contributed to the development of precision spectroscopy, optical frequency combs have also played a crucial role in the development of other applications such as the transfer of optical time and frequency references to RF, the long-range transmission of time and frequency references, distance measurement, and so on.

In the past few decades, various elegant and brilliant schemes have been proposed to generate an optical frequency comb, including mode-locked lasers, electro-optic frequency combs, microresonators, etc. A lot of efforts have been made to suppress the noise, broad the spectrum, compress the pulse and amplify the power of optical frequency combs. New technologies and applications of optical frequency combs are being proposed all the time. In this thesis, different configurations and applications of optical frequency combs are introduced, coherently synthesized two-color EO combs with low noise and broadband spectrum are demonstrated, high precision absolute distance measurement based on the coherently synthesized two-color EO comb is realized.

1.1 Optical frequency combs

The output of an optical frequency comb in time domain and frequency domain can be explained by Fig. 1-1. A pulse train is emitted from the optical frequency comb

in time domain. There are three parameters that characterize the pulse train: the repetition period of the pulses (T_r), the duration time of the pulse (τ), the pulse-to-pulse phase shift between carrier wave and envelope (Φ_{CE}). The pulses repeat every repetition period, which is basically determined by the cavity round-trip time. The pulse duration is usually at several tens to hundreds of femtoseconds. Particularly, pulses with few-femtoseconds duration time have been reported [10]. The pulse-to-pulse phase shift between carrier wave and envelope, which is so-called carrier-envelope phase (CEP), indicates the group velocity and phase velocity differentiation in the laser cavity. In fact, the carrier wave propagates at phase velocity, while the envelope propagates at group velocity.

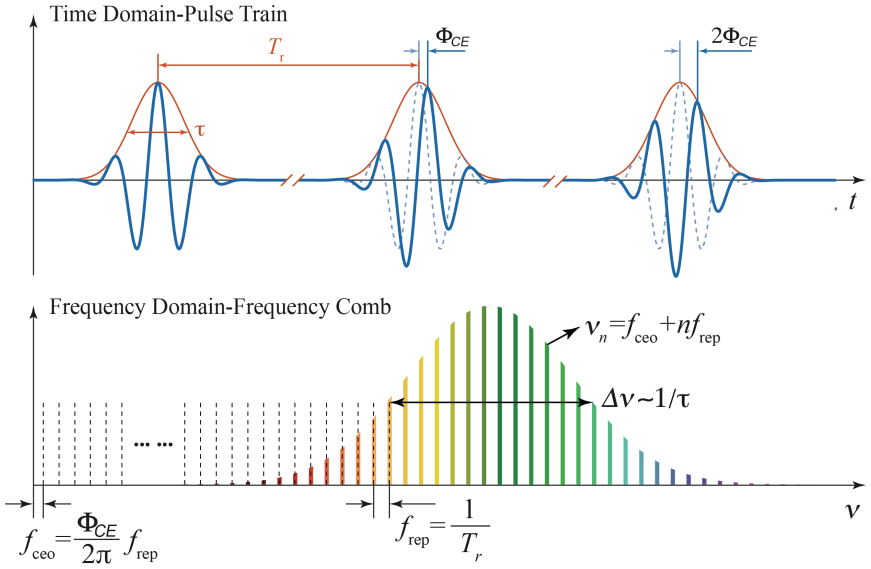

Fig. 1-1 Illustration of output from an optical frequency comb in time domain and frequency domain.

In frequency domain, the optical frequency comb presents a lot of equally spaced longitudinal modes, which is where the term 'optical frequency comb' comes from. These longitudinal modes are phase-locked. The three parameters of the pulse train in time domain, T_r, τ and Φ_{CE}, have their expression in frequency domain, which are mode spacing (f_{rep}), spectrum bandwidth ($\Delta\nu$) and carrier-envelope offset frequency (f_{ceo}), respectively. The mode spacing is the inverse of the repetition period of pulses, which is also named as repetition rate. The repetition rate usually varies from several tens MHz to GHz, according to different configurations. The $\Delta\nu$ of an optical frequency comb usually varies from few nm to hundreds of nm, which is contingent upon the cavity dispersion, nonlinearity, etc. The f_{ceo} is the frequency offset to zero

frequency of the optical frequency comb, which equals to $f_{\mathrm{rep}} \times \Phi_{CE}/2\pi$. As a result, the frequencies of all the modes can be expressed by $\nu_n = f_{\mathrm{ceo}} + nf_{\mathrm{rep}}$, where n is mode number.

Over the past decades, techniques related to optical frequency combs grow speedily. Various kinds of configurations have been demonstrated to realize optical frequency combs, including mode-locked lasers, electro-optic frequency combs and integrated optical frequency combs, etc. Optical frequency combs towards higher power, narrower pulse, new wavelength region and low noise also attract a lot of attention. The development of the optical comb is accompanied by the development of its application. For example, time and frequency metrology[11], spectroscopy [12], optical atomic clock [13], ranging and dimensional metrology [14], communication [15], to name only a few.

1.1.1 Optical frequency combs based on mode-locked lasers

Mode-locked lasers based optical frequency combs are the most maturely developed optical frequency combs, which indicate well environmental adaptability and high compactness. In the past decades, mode-locked lasers have gone through the development of dye lasers, solid-state lasers, and fiber lasers. Among solid-state lasers, Ti:sapphire mode-locked lasers have gain a lot of interests attributing to their excellent characteristics of narrow pulses, broadband spectrum and low noise. Particularly, octave spanning spectrum and pulses with less than 10 fs duration can be directly generated from Ti:sapphire mode-locked lasers [16][17]. In fact, the first optical frequency comb is generated based on a Ti:sapphire mode-locked laser [2]. So far, Ti:sapphire mode-locked lasers have been applied in high energy laser systems, attosecond science, etc. However, water cooling and expensive pump sources are required in Ti:sapphire lasers. In contrast, fiber mode-locked lasers have the advantages of more compact structure and good thermal dissipation. Various mechanisms are utilized in fiber lasers to realize mode-locking, like nonlinear polarization rotation, nonlinear amplifying loop mirror, saturable absorption and so on. The repetition rates of mode-locked fiber lasers usually vary from tens of MHz to hundreds of MHz. Erbium-doped fibers are the most commonly used gain medium in fiber lasers, leading to optical frequency combs that cover telecom window. Yb- and Tm-doped fibers are also widely used, resulting optical frequency combs with different center wavelengths. In addition, high nonlinear coefficient devices, such as

highly nonlinear fiber, photonic-crystal fiber and lithium niobate waveguides, have pave the way for spectrum broadening and nonlinear frequency conversion. Octave spanning spectrum that required in offset frequency stabilization have been realized in various systems. Moreover, terahertz wave generation [18], mid-infrared (MIR) frequency comb generation [19][20] and high power extreme ultraviolet (XUV) generation [21][22] have been reported by making use of the nonlinear optical processes. Recently, mode-locked lasers that directly emit two pulse trains with repetition rate offset from one cavity have gain a lot to attentions, especially for their applications in dual comb systems [23][24]. Up to now, it is reported that mode-locked fiber lasers have passed environmental stability tests and gravity tests, indicating its potential for future space applications [25][26].

1.1.2 Optical frequency combs based on microresonator

Microresonators have attracted increasing interests in recent years attributing to their potential to realize chip-scale optical frequency combs. Microresonators or ring-like resonators are the key components to produce the microcombs. Although there was no pulse output from the microcomb at the first demonstration [27][28], microcombs with single soliton operation become possible recently, where dispersion management of the resonator is crucial [29][30]. Attributing to the micrometer-level cavity length, repetition rates up to hundreds of GHz and even THz are achievable [31]. This property is attractive in applications like dual-comb measurements, communications, etc. [32][33][34] By combining on-chip optical devices and detectors, fully integrated chip-scale light detection and ranging (LIDAR) system will be possible in the future. Unfortunately, large tuning range of the repetition rate is not allowed. Besides, more efforts need to be paid in order to deeply understand the dynamics.

1.1.3 Optical frequency combs based on electro-optic frequency combs

Besides mode-locked lasers and microresonators, electro-optic frequency combs (EO combs) are also gaining a lot of attentions, benefiting to their simple configuration and excellent controllability. Electro-optic modulation is the key point of EO combs, which is based on the electro-optic effect. To obtain an EO comb, the phase and intensity of a CW laser are modulated through EO modulation, resulting in

the generation of cascaded sidebands in frequency domain and pulses in time domain [35][36][37]. The phase of these sidebands follows certain relationship. The spacing of these sidebands is the repetition rate of the EO comb, which is usually at tens of GHz level. Since the repetition rate is only determined by the modulation frequency of the EO modulators, it can be flexibly tuned in a large tuning range with high tuning speed. This characteristic is not allowed in neither mode-locked lasers nor microresonators. In addition, the shape mapping from pulse shape to spectrum shape is attractive in many applications [38]. As a result, the spectrum shape can be designed according to the pulse shape in time domain. Based on the time-to-frequency mapping, improving the spectrum flatness of an EO comb becomes a popular research topic, which is attractive in applications like telecommunications, arbitrary waveform generation. EO combs with Gaussian-shaped spectrum are also demonstrated. Besides utilizing cascaded EO modulators, one can place the modulator in an optical resonator and drive it with microwave signals that matches the free spectral range of the resonator [39][40][41][42].

However, limited spectrum bandwidth and accumulated phase noise at spectrum edges are the two weaknesses of EO combs. A lot of research has been made to broaden the spectrum bandwidth and reduce the phase noise of comb modes. So far, EO combs with octave spanning spectrum have been realized through hybrid highly nonlinear fibers or silicon nitride waveguides [43][44]. On the other hand, the phase noise of the driven signal of the modulators accumulates at the comb modes, especially at high offset frequency. This accumulation is detrimental for broadband EO combs to maintain comb structure. Various methods have been demonstrated to suppress such phase noise accumulation. For example, two comb modes in an EO comb can be linked to a reference frequency comb, resulting in the phase noise suppression of comb modes with comb mode number less than the locked comb modes [45][46]. A Fabry-perot cavity after the EO comb generation or a built-in Fabry-perot cavity is more effective in reducing the accumulated phase noise [43][44][47]. Actually, the Fabry-perot cavity is crucial to the detection and phase-locking of carrier-envelope offset frequency in EO combs.

More recently, EO combs integrated in lithium-niobate waveguides have gain a lot of interests [48][49][50]. Benefiting to the large EO response of the waveguides, both the spectrum bandwidth of the EO comb and electro-optical conversion efficiency are increased. System compactness is greatly improved in this case.

Dispersion management and spectrum broadening can be integrated in the waveguide as well, which further reducing the system complexity.

1.1.4 Applications of optical frequency combs

Optical frequency transfer. As is well known, the frequency of each comb mode in an optical frequency comb can be determined by repetition rate and offset frequency. Since the repetition rate and the offset frequency are both radio frequencies, the optical frequency comb can be considered as an excellent bridge to realize coherence transfer between radio frequencies and optical frequencies. As a result, researchers are able to get rid of sophisticated approaches to realize coherence transfer between optical frequencies and radio frequencies, such as harmonic frequency chain and optical interval division [52][53]. In recent decades, optically generated microwaves with ultralow phase noise have been demonstrated by many research groups [54][55][56]. In addition, optical frequency combs provide indispensable bridges that enable comparison between different optical clocks. The comparison of Hg^+ and Ca optical clocks through an optical frequency comb was the first attempt [57]. Subsequently, the comparison between other optical clocks were demonstrated [58][59][60]. Besides, an optical frequency comb that linked to an optical clock can be served as a frequency reference over wide frequency range [51].

Spectroscopy. Attributing to the broad spectrum and the equally spaced comb modes, optical frequency combs have been widely applied in spectroscopy. Dual-comb spectroscopy (DCS) is one of the most popular approaches [61]. In principle, by down sampling one frequency comb through another frequency comb with repetition rate offset, a new frequency comb located in radio frequency domain (RF comb) is generated. The absorption information (amplitude or phase) of the sample that placed in the optical path could be obtained by detecting the RF comb. The frequency resolution of DCS is settled by the repetition rate of the optical frequency comb, which is much higher than conventional spectrometers [62][63][64][65]. Besides, DCS exhibits high accuracy, high update rate and high signal-to-noise ratio, as well as the potential to achieve system compactness. Up to date, DCS has been applied in various wavelength regions from visible light to THz region [66][67][68][69][70].

Distance measurement. Optical frequency combs are elegant laser sources for

distance measurement. On the one hand, the femtosecond pulses that emitted from optical frequency combs make high-precision time-of-flight measurement in large range become possible [71]. Dual comb technique and optical cross correlation are widely-utilized methods to realize high precision time-of-flight measurement [14][72]. On the other hand, various kinds of interferometry are demonstrated in distance measurement on the basic of optical frequency combs, like synthetic wavelength technique [73], spectrally resolved interferometry [74], multi-heterodyne interferometry [75], to name a few. Besides, absolute distance measurement could be achieved by measuring the phase of the beat notes between the comb modes in an optical frequency comb [76]. Although nanometer precision distance measurement had been realized before the concept of fully-stabilized optical frequency comb [78], optical frequency combs indeed extend the sub-wavelength precision at long range up to kilometers [14].

Besides the above fields, optical frequency combs could be utilized in many other applications, like telecommunications, attosecond science, metrology, time to frequency transfer, and so on. The development of optical frequency combs facilitates their applications, and vice versa. In the future, new applications and optical frequency comb techniques might emerge. The optical frequency combs might become more tightly linked with applications, which also promotes technological advances.

1.2 Distance measurement

Lasers, especially optical frequency combs, have been widely applied in distance measurement attributing to their good directionality, long coherence length and high brightness. The introduction of lasers in distance measurement enables high accuracy and high-resolution measurement at large range. So far, laser-based ranging has greatly contributed to the development of various scientific and industrial fields, such as radar technology, precision manufacturing, remote sensing and mapping, nanotechnology, aerospace, and autonomous driving, etc. The research progress of distance measurement is described in this section. The benefits of utilizing optical frequency combs as the optical source for distance measurement are clarified. Some distance measurement techniques that on the basic of optical frequency combs are introduced.

1.2.1 Definition of meter and its measurement before the invention of optical frequency comb

Meter, symbol m, is one of the SI base units. It is defined as the distance that light travels in vacuum within 1/299792458 s [79]. This definition is based on the fixed numerical value of the speed of light in vacuum c, which is 299792458 when expressed in the unit m/s. According to the definition, there are mainly two methods to reproduce the length or distance.

(1) According to $L = c \times t$, the distance under test can be obtained by measuring the time-of-flight t that used for light propagation.

As illustrated in Fig. 1-2, a pulse or a pulse train is emitted and reflected by the target. A photodetector is used to detect the reflection light. The distance under test is obtained by measuring the time interval, t, between the emission time and receiving time. Considering the double pass propagation, the distance under test is $L = c \times t/2$. The time-of-flight ranging technique has very important applications in the fields of remote sensing detection such as LIDAR. For example, the distance between Earth and Moon was measured with accuracy better than 0.08-m by using a commercial Q-switched lasers as the optical source. Because of the limited response time (picosecond level) of photodetectors, the resolution of direct time-of-flight measurement is limited to millimeter level. Therefore, improving the accuracy of time-of-flight measurement requires new techniques that enable high precision measurement of pulse position.

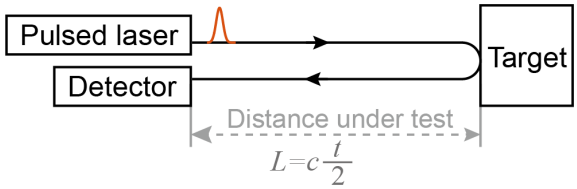

Fig. 1-2 The principle of time-of-flight measurement.

(2) According to $\lambda = c/f$, the vacuum wavelength of electromagnetic radiation λ and the frequency of the radiation λ is linked by the speed of light in vacuum. By analogical comparison of distance under test to vacuum wavelength and the phase to 2π, the distance under test can be obtained from interferometry. In case of single pass propagation of the electromagnetic wave, the distance under test is expressed by $L = \varphi\lambda/2\pi$, where φ is phase. Note that the distance under test is expressed by $L = \varphi\lambda/4\pi$ when double pass

propagation is applied.

The principle of optical interferometric phase detection based distance measurement is explained in Fig. 1-3. The laser beam emitted from the continuous-wave (CW) laser is reflected by the target and detected. The phase of the reflected beam is compared with that of the initial beam. The distance under test is then calculated by $L = \varphi\lambda/4\pi n$, where φ is phase increment, λ is optical wavelength of the CW laser and n is air refractive index. Here, the optical wavelength of the CW laser serves as the measurement reference. Hence sub-wavelength resolution is realizable. However, this is an incremental measurement rather than absolute distance measurement. Once the optical path is blocked and unblocked, the system is no longer able to determine the absolute position of the target. It is because the non-ambiguity range where the integer multiple of the phase can be uniquely determined is limited to a half wavelength due to the periodic nature of phase measurements, which is normally much smaller than the system fluctuation.

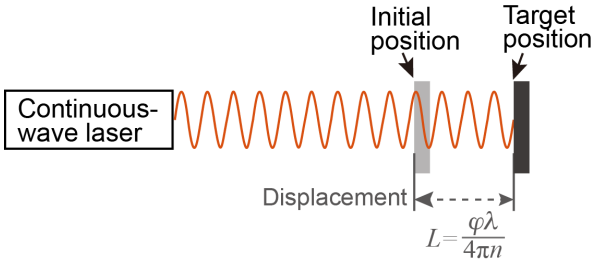

Fig. 1-3 The principle of distance measurement based on interferometric phase detection.

Several techniques have been reported to realize absolute distance measurement based on phase detection and to enlarge the non-ambiguity range. One popular method is to impose amplitude modulation or polarization modulation on the CW laser [80][81][82]. Consequently, the intensity or the polarization state of the CW laser varies depending on the external field. By comparing the phase of the external field before and after reflected by the target, the distance under test is obtained. The non-ambiguity range is decided by the frequency of the external field, which is usually on the order of meters. Synthetic wavelength technique is an alternative to extend the non-ambiguity range (NAR) [83]. The beat between two or more CW lasers with different optical frequencies generates the synthetic wavelength, which is inversely proportional to the frequency difference. Unfortunately, high-precision coherent synthesis between these CW lasers is essential to guarantee a resolution that better than the non-ambiguity range of interferometric phase measurement. System

becomes complex and compactness is degraded consequently. A modified synthetic wavelength technique is demonstrated by Lay O. P. et al., aiming to get rid of complex phase-locked loops [84]. In this method, several sidebands are generated around the CW laser through phase modulation. Synthetic wavelength is the result of beat between the CW laser and sidebands.

1.2.2 Advantages of using optical frequency comb for distance measurement

Optical frequency combs are excellent candidates for absolute distance measurement, attributing to the ultrashort pulse train in the time domain and numerous comb modes in frequency domain. From time domain, optical frequency combs are excellent candidates that provide ultrashort pulses. Pulses with sub-10 fs duration have been demonstrated in optical frequency combs [85]. However, taken the dispersion and the attenuation of air into consideration, it is recommended to use pulse trains with pulse width of several hundred femtosecond for large scale distance measurement in atmosphere [86]. High precision measurement of pulse position could be realized through optical cross correlation, which is an all-optical sampling method. In optical cross correlation, an ultrashort pulse train, which serves as the ultranarrow shutters, samples the pulse train that carries the information under test. As a result, the pulse position can be detected with high accuracy, breaking the response time limits of electronic devices. Hence high-accuracy absolute distance measurement could be achieved.

From frequency domain, one optical frequency comb can be served as multi-wavelength laser sources with their phase tightly locked. So an optical frequency comb could be used as the reference to realize coherent synthesis of several CW lasers, enabling synthetic wavelength technique [87][88][89][90]. A wavelength tunable CW laser with its frequency referenced to an optical frequency comb can also be utilized to synthetic wavelength technique [91]. In 2000, K. Minoshima et al. demonstrated a comb distance meter by measuring the phase of beat notes between the comb modes in a mode-locked laser that directly generating a series of synthetic wavelengths [76]. Multi-heterodyne interferometry is available in distance measurement by the interference between two optical frequency combs with slight comb spacing offset [14].

1.2.3 Absolute distance measurements based on optical frequency comb

Many techniques have been developed for absolute distance measurement based on optical frequency comb. Some of these techniques are introduced in the following, including comb distance meter, spectrally-resolved interferometry, dual-comb ranging and frequency-modulated continuous wave (FMCW) LiDAR. It's worth to note that one technique may not meet the requirements for all the applications because of its own limitations. Hence many researchers measure the under-test distance through several different techniques [71][92]. The limitations of each technique, such as poor precision and small NAR, are overcome. In addition, the calibration of air refractive index is quite important for high precision distance measurement. In fact, the uncertainty of air refractive index is the dominant factor in uncertainty of the distance measurement in most cases, especially in large scale distance measurement. So the calibration of air refractive index is also introduced in this section.

Comb distance meter. K. Minoshima et al. firstly demonstrated absolute distance measurement based on optical frequency comb in 2000 [76]. The beat between the comb modes in an optical frequency comb generates a series of synthetic waves of frequencies that varies from several tens of MHz to several THz. The phase of these frequency components, which is proportional to the distance under test, is detected, resulting in absolute distance measurement at 240 m with 2 μm resolution [77]. In this method, high precision measurement is realized via detecting higher order harmonics, while non-ambiguity range is determined through the first order harmonic. Further extension of non-ambiguity range could be realized by scanning the repetition rate and repeating the phase measurement.

Spectrally-resolved interferometry. K. Joo et al. firstly describe spectrally-resolved interferometry based on an optical frequency comb, resulting in high precision measurement of optical path delay between two pulses from an Michelson interferometer [93][94][95]. The interference between the two pulses generates abundant interference signals simultaneously in frequency domain, attributing to the numerous comb modes in an optical frequency comb. The phase relationship between these interference signals reveals the optical path delay. This measurement non-ambiguity range is usually at millimeter level due to the limited spectrum resolution of the spectrometer [96]. Through applying virtually image phase array based spectrometer, the non-ambiguity range is enlarged by an order of

magnitude [97][98]. On the basic of spectrally-resolved interferometry, chirped pulse spectral interferometry is demonstrated by K. Minoshima and T. Kato et al. [100]. The optical path delay can be directly read out from the interferometric spectrum, which reflects the instantaneous spectrum of the chirp [99], instead of running some demodulation algorithms. Thus non-scanning distance measurement is achieved.

Dual-comb ranging. Dual comb ranging technique is one of the most widely used ranging techniques in recent years, which was firstly demonstrated in 2009 [14]. This technique relies on two optical frequency combs with slight difference in repetition rates, which serves as signal comb and local oscillator comb, respectively. The pulses from signal comb are reflected by target mirror and then combined with the pulses from local comb, as shown in Fig. 1-4. Attributing to the repetition rate difference (Δf_{rep}), the pulses from local comb sample the specific part of the reflected pulses from target mirror in each pulse repetition period. As a result, the shape of the reflected pulse is completely recorded with a magnification factor of $f_{\mathrm{rep}}/\Delta f_{\mathrm{rep}}$, where the f_{rep} is the repetition rate of signal comb. So that the time-of-flight can be extracted by electronic methods with high precision. Besides time-of-flight measurement, dual-comb ranging also enables distance measurement with multi-wavelength interferometry [75][101][102][103][104][105]. The beating between the comb mode pairs with similar frequency in the two combs generate an RF frequency comb in frequency domain. The distance under test could be retrieved from the phase of each mode in the RF frequency comb.

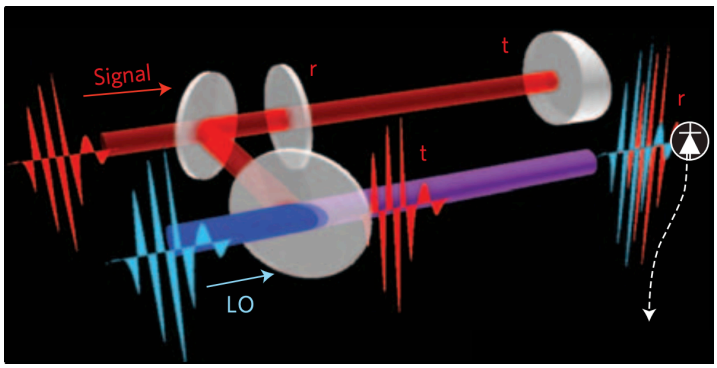

Fig. 1-4 The principle of dual-comb ranging [14].

So far, various optical frequency combs have been utilized in dual-comb ranging, like mode-locked lasers, microresonators and EO combs [75][106][107]. Nanometer-level resolution with kilometer-level non-ambiguity range have been realized through combining several methods.

In dual-comb ranging, the non-ambiguity range is determined by $v_g/2f_{rep}$, where v_g is the group velocity and f_{rep} is the repetition rate of signal comb. The non-ambiguity range could be further extended by scanning the repetition rate of signal comb and repeating the measurement [108][109]. X. Zhao et al. demonstrate further non-ambiguity range extension to 150 m through triple-comb ranging [110]. The update rate of dual-comb ranging is defined by the repetition rate difference between the two combs. So utilizing high repetition rate frequency combs in dual-comb systems is beneficial to increase the update rate. Ultrafast distance measurement with 96.4-MHz update rate has been realized in dual-comb ranging system based on microresonators [111]. It's worth to note that there are optimized values of repetition rate difference in a specific dual-comb ranging system [112][113].

In the beginning period of dual-comb ranging technique, the repetition rate and the carrier-envelope offset frequency of the two combs should be tightly phase-locked in order to maintaining the coherence between the two combs. The complex phase-locked loops make the system bulky and costly, which restrict the outdoor applications of dual-comb ranging technique. To reduce the system complexity, dual-comb ranging systems based on free-running lasers and asynchronous optical sampling (ASOPS) have been demonstrated [114][115]. The impact of pulse train timing jitter on time-of-flight measurements are studied [116][117]. Further system simplification has been demonstrated by using dual-comb lasers as optical sources, where two pulse trains with repetition rate difference are directly emitted from one cavity[118][119][120][121][122][123][124]. For example, Carlson D. R. et al. demonstrated dual-comb generation by rapidly switching the repetition rate of the EO comb [124]. Then two pulse trains with repetition rate offset are generated by splitting the output pulse train, delaying one of the beam paths and recombining the two paths.

FMCW LIDAR. FMCW LIDAR technology has attracted widespread attentions in recent years, which shows great potential for application in autonomous driving, cartography, etc. [125][126][127]. This technology is based on coherent measurement that uses a narrow line width CW laser as the optical source. Absolute distance and moving speed measurement of the target is realized by measuring the frequency of the interference signal between the emitted and reflected signal. Compared to non-coherent absolute measurement techniques such as time-of-flight measurement, the laser emission power requirement is greatly reduced. Meanwhile, this technique is completely independent of external disturbances such as solar irradiation and other

thermal sources.

The measurement resolution and the largest measurement range of FMCW LIDAR is related to the frequency scanning range and the coherence length of the CW laser, respectively. However, these two parameters are incompatible for a specific CW laser in general [128]. Recently, N. Kuse et al. demonstrate triplication of the frequency scanning range through an EO comb, since the frequency of all comb modes in an EO combs changes according to the modulated CW laser [129]. This multiplication of the frequency scanning range is also realized through a microresonator [130][131][132]. Moreover, the nonlinearity in the frequency scanning of the CW laser, which deteriorate the measurement accuracy, could be calibrated by an optical frequency comb [133][134].

Calibration of Air refractive index. Conventionally, the air refractive index is calculated according to empirical equation such as Ciddor's equation or Edlén's equation [135][136]. The empirical equation relies on high precision measurement of environmental conditions, like temperature, pressure, humidity and CO_2 concentration. Unfortunately, this is unsuitable in out-of-lab fields and rapidly changing environment. So far, two-color method [137] is demonstrated as a powerful tool for air refractive index self-correction in distance measurement based on mode-locked fiber OFCs [138][139][140][141]. In two-color method using fiber OFCs, fundamental frequency and its second harmonic of a mode-locked fiber laser (for example, fundamental frequency at 192 THz and second harmonic at 384 THz) are used to measure the same distance simultaneously. Benefiting from the dispersion relation of air, the geometrical length of the distance under test is obtained by the two measured values, without knowing the refractive index. More recently, K. Minoshima et al. demonstrated air refractive index correction by making use of phase refractive index and group refractive index of air based on an optical frequency comb [142]. The system setup is simplified via getting rid of complex second harmonic generation. Specifically, the pulse envelope propagates at the group velocity, while the carrier wave propagates at phase velocity. Precise measurement of the pulse envelope is the key point of high accuracy air refractive index correction [143].

1.3 Organization of this thesis

EO comb generation, phase noise suppression of comb modes in an EO comb

and absolute distance measurement based on EO combs are studied in this thesis. Low noise coherently synthesized two-color EO comb is proposed and demonstrated, which shows the advantages of low phase noise and broadband spectrum. On the basic of the coherently synthesized two-color EO comb, nanometer-precision absolute distance measurement is achieved. The non-ambiguity range of the distance measurement system is extended through combining several methods. The research in this thesis shows a simple and flexible method to reduce the phase noise of comb modes in an EO comb, which paves the way for the applications of EO combs that requires high precision and compact configuration. Here the absolute distance measurement is a successful demonstration of applications based on coherently synthesized two-color EO comb.

This thesis is organized as follows:

In Chapter 2, the principle of EO modulators, EO comb generation based on EO modulators, advantages of EO combs and the phase noise of comb modes in an EO comb are introduced. The principle of distance measurement based on single wavelength interferometry, synthetic wavelength technique and microwave phase detection is explained.

In Chapter 3, the EO comb generation is numerically simulated. Coherently synthesized two-color EO comb is proposed. The suppression of accumulated phase noise is experimentally verified. A broadband coherently synthesized two-color EO comb is demonstrated. System compactness is realized by integrating the optical devices into a small box.

In chapter 4, the coherently synthesized two-color EO comb is applied to distance measurement. A fiber interferometer is utilized in the distance measurement system for the sake of compactness. System performances are investigated, including stability, linearity, measurement error. Fast displacement measurement and absolute distance measurement are achieved.

In chapter 5, some enhancements are implemented to improve the stability and precision of the distance measurement system. A free space interferometer with three arms is utilized. The third arm, monitor arm, makes the length fluctuation in the reference arm has negligible impact on the measurement results. As a result, precision of $< \pm 25$ nm is realized.

In chapter 6, the content in this thesis is summarized. Outlooks of future improvements and potential applications are provided.

1.4 References

[1] T. Udem, J. Reichert, R. Holzwarth, and T. W. Hänsch, Absolute optical frequency measurement of the cesium D 1 line with a mode-locked laser[J]. Physical review letters, 1999, 82(18): 3568.

[2] D. J. Jones, S. A. Diddams, J. K. Ranka, A. Stentz, R. S. Windeler, J. L. Hall, and S. T. Cundiff, Carrier-envelope phase control of femtosecond mode-locked lasers and direct optical frequency synthesis[J]. Science, 2000, 288(5466): 635-639.

[3] S. A. Diddams, K. Vahala, and T. Udem, Optical frequency combs: Coherently uniting the electromagnetic spectrum[J]. Science, 2020, 369(6501): eaay3676.

[4] S. T. Cundiff, and J. Ye, Colloquium: Femtosecond optical frequency combs[J]. Reviews of Modern Physics, 2003, 75(1): 325.

[5] J. Ye, and S. T. Cundiff, Femtosecond optical frequency comb: principle, operation and applications[M]. Springer Science & Business Media, 2005.

[6] T. Fortier, and E. Baumann, 20 years of developments in optical frequency comb technology and applications[J]. Communications Physics, 2019, 2(1): 153.

[7] J. Kim, and Y. Song, Ultralow-noise mode-locked fiber lasers and frequency combs: principles, status, and applications[J]. Advances in Optics and Photonics, 2016, 8(3): 465-540.

[8] J. L. Hall, Nobel Lecture: Defining and measuring optical frequencies[J]. Reviews of Modern Physics, 2006, 78(4): 1279-1295.

[9] T. W. Hänsch. Nobel lecture: Passion for precision[J]. Reviews of Modern Physics, 2006, 78(4): 1297-1309.

[10] U. Morgner, F. X. Kärtner, S. H. Cho, Y. Chen, H. A. Haus, J. G. Fujimoto, E. P. Ippen, V. Scheuer, G. Angelow, and T. Tschudi, Sub-two-cycle pulses from a Kerr-lens mode-locked Ti: sapphire laser[J]. Optics letters, 1999, 24(6): 411-413.

[11] T. Udem, R. Holzwarth, and T. W. Hänsch, Optical frequency metrology[J]. Nature, 2002, 416(6877): 233-237.

[12] M. C. Stowe, M. J. Thorpe, A. Pe'er, J. Ye, J. E. Stalnaker, V. Gerginov and S. A. Diddams, Direct frequency comb spectroscopy[J]. Advances in Atomic, Molecular, and Optical Physics, 2008, 55: 1-60.

[13] T. L. Nicholson, S. L. Campbell, R. B. Hutson, G. E. Marti, B. J. Bloom, R. L. McNally, W. Zhang, M. D. Barrett, M. S. Safronova, G. F. Strouse, W. L. Tew, and J. Ye, Systematic evaluation of an atomic clock at 2×10^{-18} total uncertainty[J]. Nature communications, 2015, 6(1): 1-8.

[14] I. Coddington, W. C. Swann, L. Nenadovic, and N. R. Newbury, Rapid and precise absolute distance measurements at long range[J]. Nature photonics, 2009, 3(6): 351-356.

[15] S. Kawanishi, Ultrahigh-speed optical time-division-multiplexed transmission

technology based on optical signal processing[J]. IEEE Journal of Quantum Electronics, 1998, 34(11): 2064-2079.

[16] U. Morgner, R. Ell, G. Metzler, T. R. Schibli, F. X. Kärtner, J. G. Fujimoto, H. A. Haus, and E. P. Ippen, Nonlinear optics with phase-controlled pulses in the sub-two-cycle regime[J]. Physical Review Letters, 2001, 86(24): 5462.

[17] T. M. Fortier, A. Bartels, and S. A. Diddams, Octave-spanning Ti: sapphire laser with a repetition rate> 1 GHz for optical frequency measurements and comparisons[J]. Optics letters, 2006, 31(7): 1011-1013.

[18] I. A. Finneran, J. T. Good, D. B. Holland, P. B. Carroll, M. A. Allodi, and G. A. Blake, Decade-spanning high-precision terahertz frequency comb[J]. Physical review letters, 2015, 114(16): 163902.

[19] A. Schliesser, N. Picqué, and T. W. Hänsch, Mid-infrared frequency combs[J]. Nature photonics, 2012, 6(7): 440-449.

[20] D. M. B. Lesko, H. Timmers, S. Xing, A. Kowligy, A. J. Lind, and S. A. Diddams, A six-octave optical frequency comb from a scalable few-cycle erbium fibre laser[J]. Nature Photonics, 2021, 15(4): 281-286.

[21] R. J. Jones, K. D. Moll, M. J. Thorpe, and J. Ye, Phase-coherent frequency combs in the vacuum ultraviolet via high-harmonic generation inside a femtosecond enhancement cavity[J]. Physical Review Letters, 2005, 94(19): 193201.

[22] A. Cingöz, D. C. Yost, T. K. Allison, A. Ruehl, M. E. Fermann, I. Hartl, and J. Ye, Direct frequency comb spectroscopy in the extreme ultraviolet[J]. Nature, 2012, 482(7383): 68-71.

[23] R. Liao, H. Tian, W. Liu, R. Li, Y. Song, and M. Hu, Dual-comb generation from a single laser source: principles and spectroscopic applications towards mid-IR—A review[J]. Journal of Physics: Photonics, 2020, 2(4): 042006.

[24] R. Li, H. Shi, H. Tian, Y. Li, B. Liu, Y. Song, and M. Hu, All-polarization-maintaining dual-wavelength mode-locked fiber laser based on Sagnac loop filter[J]. Optics Express, 2018, 26(22): 28302-28311.

[25] L. Sinclair, I. Coddington, W. C. Swann, G. B. Rieker, A. Hati, K. Iwakuni, and N. R. Newbury, Operation of an optically coherent frequency comb outside the metrology lab[J]. Optics Express, 2014, 22(6): 6996-7006.

[26] M. Lezius, T. Wilken, C. Deutsch, M. Giunta, O. Mandel, A. Thaller, V. Schkolnik, M. Schiemange, A. Dinkelaker, A. Kohfeldt, A. Wicht, M. Krutzik, A. Peters, O. Hellmig, H. Duncker, K. Sengstock, P. Windpassinger, L. Lampmann, T. Hülsing, Theodor W. Hänsch, and Ronald Holzwarth, Space-borne frequency comb metrology[J]. Optica, 2016, 3(12): 1381-1387.

[27] T. J. Kippenberg, S. M. Spillane, and K. J. Vahala, Kerr-nonlinearity optical parametric oscillation in an ultrahigh-Q toroid microcavity[J]. Physical review letters, 2004, 93(8): 083904.

[28] P. Del'Haye, A. Schliesser, O. Arcizet, T. Wilken, R. Holzwarth, and T. J.

Kippenberg, Optical frequency comb generation from a monolithic microresonator[J]. Nature, 2007, 450(7173): 1214-1217.

[29] T. Herr, V. Brasch, J. D. Jost, C. Y. Wang, N. M. Kondratiev, M. L. Gorodetsky, and T. J. Kippenberg, Temporal solitons in optical microresonators[J]. Nature Photonics, 2014, 8(2): 145-152.

[30] X. Yi, Q. Yang, K. Y. Yang, M. G. Suh, and K. Vahala, Soliton frequency comb at microwave rates in a high-Q silica microresonator[J]. Optica, 2015, 2(12): 1078-1085.

[31] T. C. Briles, J. R. Stone, T. E. Drake, D. T. Spencer, C. Fredrick, Q. Li, D. Westly, B. R. Ilic, K. Srinivasan, S. A. Diddams, and S. B. Papp, Interlocking Kerr-microresonator frequency combs for microwave to optical synthesis[J]. Optics letters, 2018, 43(12): 2933-2936.

[32] P. M. Palomo, J. N. Kemal, M. Karpov, A. Kordts, J. Pfeifle, M. H. P. Pfeiffer, P. Trocha, S. Wolf, V. Brasch, M. H. Anderson, R. Rosenberger, K. Vijayan, W. Freude, T. J. Kippenberg, and C. Koos, Microresonator-based solitons for massively parallel coherent optical communications[J]. Nature, 2017, 546(7657): 274-279.

[33] P. Trocha, M. Karpov, D. Ganin, M. H. P. Pfeiffer, A. Kordts, S. Wolf, J. Krockenberger, P. M. Palomo, C. Weimann, S. Randel, W. Freude, T. J. Kippenberg, and C. Koos, Ultrafast optical ranging using microresonator soliton frequency combs[J]. Science, 2018, 359(6378): 887-891.

[34] M. G. Suh, and K. J. Vahala, Soliton microcomb range measurement[J]. Science, 2018, 359(6378): 884-887.

[35] I. Morohashi, T. Sakamoto, H. Sotobayashi, T. Kawanishi, I. Hosako, and M. Tsuchiya, Widely repetition-tunable 200 fs pulse source using a Mach–Zehnder-modulator-based flat comb generator and dispersion-flattened dispersion-decreasing fiber[J]. Optics letters, 2008, 33(11): 1192-1194.

[36] A. Ishizawa, T. Nishikawa, A. Mizutori, H. Takara, H. Nakano, T. Sogawa, A. Takada, and M. Koga, Generation of 120-fs laser pulses at 1-GHz repetition rate derived from continuous wave laser diode[J]. Optics express, 2011, 19(23): 22402-22409.

[37] A. J. Metcalf, V. T. Company, D. E. Leaird, and A. M. Weiner, High-power broadly tunable electrooptic frequency comb generator[J]. IEEE Journal of Selected Topics in Quantum Electronics, 2013, 19(6): 231-236.

[38] J. Azaña, Time-to-frequency conversion using a single time lens[J]. Optics communications, 2003, 217(1-6): 205-209.

[39] T. Kobayashi, T. Sueta, Y. Cho, and Y. Matsuo, High-repetition-rate optical pulse generator using a Fabry-Perot electro-optic modulator[J]. Applied Physics Letters, 1972, 21(8): 341-343.

[40] M. Kourogi, B. Widiyatomoko, Y. Takeuchi, and M. Ohtsu, Limit of

optical-frequency comb generation due to material dispersion[J]. IEEE journal of quantum electronics, 1995, 31(12): 2120-2126.

[41] P. Sekhar, C. Fredrick, S. Leifer, and, S. A. Diddams, Fiber-Integrated Supercontinuum with a 20 GHz Resonant Electro-Optic Frequency Comb[C]//CLEO: Science and Innovations. Optica Publishing Group, 2021: STu2D. 2.

[42] S. A. Diddams, L. Ma, J. Ye, and J. L. Hall, Broadband optical frequency comb generation with a phase-modulated parametric oscillator[J]. Optics letters, 1999, 24(23): 1747-1749.

[43] K. Beha, D. C. Cole, P. Del'Haye, A. Coillet, S. A. Diddams, and S. B. Papp, Electronic synthesis of light[J]. Optica, 2017, 4(4): 406-411.

[44] D. R. Carlson, D. D. Hickstein, W. Zhang, A. J. Metcalf, F. Quinlan, S. A. Diddams, and S. B. Papp, Ultrafast electro-optic light with subcycle control[J]. Science, 2018, 361(6409): 1358-1363.

[45] N. Kuse, T. R. Schibli, and M. E. Fermann, Low noise electro-optic comb generation by fully stabilizing to a mode-locked fiber comb[J]. Optics Express, 2016, 24(15): 16884-16893.

[46] A. Ishizawa, T. Nishikawa, T. Goto, K. Hitachi, T. Sogawa, and H. Gotoh, Ultralow-phase-noise millimetre-wave signal generator assisted with an electro-optics-modulator-based optical frequency comb[J]. Scientific Reports, 2016, 6(1): 24621.

[47] J. Kim, D. J. Richardson, and R. Slavík, Cavity-induced phase noise suppression in a Fabry–Perot modulator-based optical frequency comb[J]. Optics Letters, 2017, 42(8): 1536-1539.

[48] M. Zhang, B. Buscaino, C. Wang, A. S. Ansari, C. Reimer, R. Zhu, J. M. Kahn, and M. Lončar, Broadband electro-optic frequency comb generation in a lithium niobate microring resonator[J]. Nature, 2019, 568(7752): 373-377.

[49] Y. Hu, M. Yu, B. Buscaino, N. Sinclair, D. Zhu, R. Cheng, A. S. Ansari, L. Shao, M. Zhang, J. M. Kahn, and M. Lončar, High-efficiency and broadband on-chip electro-optic frequency comb generators[J]. Nature Photonics, 2022, 16(10): 679-685.

[50] A. S. Ansari, M. Yu, Z. Chen, C. Reimer, M. Zhang, N. Picqué, and M. Lončar, Thin-film lithium-niobate electro-optic platform for spectrally tailored dual-comb spectroscopy[J]. Communications Physics, 2022, 5(1): 88.

[51] H. Leopardi, J. D. Rodriguez, F. Quinlan, J. Olson, J. A. Sherman, S. A. Diddams, and T. M. Fortier, Single-branch Er: fiber frequency comb for precision optical metrology with 10− 18 fractional instability[J]. Optica, 2017, 4(8): 879-885.

[52] H. Schnatz, B. Lipphardt, J. Helmcke, F. Riehle, and G. Zinner, First phase-coherent frequency measurement of visible radiation[J]. Physical Review Letters, 1996, 76(1): 18.

[53] T. W. Hänsch, High resolution spectroscopy of hydrogen[C]//The Hydrogen Atom: Proceedings of the Symposium, Held in Pisa, Italy, June 30–July 2, 1988. Springer Berlin Heidelberg, 1989: 93-102.

[54] F. Quinlan, T. M. Fortier, M. S. Kirchner, J. A. Taylor, M. J. Thorpe, N. Lemke, A. D. Ludlow, Y. Jiang, and S. A. Diddams, Ultralow phase noise microwave generation with an Er: fiber-based optical frequency divider[J]. Optics letters, 2011, 36(16): 3260-3262.

[55] T. M. Fortier, F. Quinlan, A. Hati, C. Nelson, J. A. Taylor, Y. Fu, J. Campbell, and S. A. Diddams, Photonic microwave generation with high-power photodiodes[J]. Optics letters, 2013, 38(10): 1712-1714.

[56] Endo, T. D. Shoji, T. R. Schibli, High-sensitivity optical to microwave comparison with dual-output Mach-Zehnder modulators[J]. Scientific reports, 2018, 8(1): 4388.

[57] S. A. Diddams, T. Udem, J. C. Bergquist, E. A. Curtis, R. E. Drullinger, L. Hollberg, W. M. Itano, W. D. Lee, C. W. Oates, K. R. Vogel, and D. J. Wineland, An optical clock based on a single trapped 199Hg+ ion[J]. Science, 2001, 293(5531): 825-828.

[58] T. Rosenband, D. B. Hume, P. O. Schmidt, C. W. Chou, A. Brusch, L. Lorini, W. H. Oskay, R. E. Drullinger, T. M. Fortier, J. E. Stalnaker, S. A. Diddams, W. C. Swann, N. R. Newburry, W. M. Itano, D. J. Wineland, J. C. Bergquist, Frequency ratio of Al^{+} and Hg^{+} single-ion optical clocks; metrology at the 17th decimal place[J]. Science, 2008, 319(5871): 1808-1812.

[59] R. M. Godun, P. B. R. Nisbet-Jones, J. M. Jones, S. A. King, L. A. M. Johnson, H. S. Margolis, K. Szymaniec, S. N. Lea, K. Bongs, and P. Gill, Frequency ratio of two optical clock transitions in $^{171}Yb^{+}$ and constraints on the time variation of fundamental constants[J]. Physical review letters, 2014, 113(21): 210801.

[60] F. R. Giorgetta, W. C. Swann, L. C. Sinclair, E. Baumann, I. Coddington, and N. W. Newbury, Optical two-way time and frequency transfer over free space[J]. Nature Photonics, 2013, 7(6): 434-438.

[61] I. Coddington, N. Newbury, and W. Swann, Dual-comb spectroscopy[J]. Optica, 2016, 3(4): 414-426.

[62] I. Coddington, W. C. Swann, and N. R. Newbury, Coherent multiheterodyne spectroscopy using stabilized optical frequency combs[J]. Physical Review Letters, 2008, 100(1): 013902.

[63] N. Picqué, and T. W. Hänsch, Frequency comb spectroscopy[J]. Nature Photonics, 2019, 13(3): 146-157.

[64] B. Bernhardt, A. Ozawa, P. Jacquet, M. Jacquey, Y. Kobayashi, T. Udem, R. Holzwarth, G. Guelachvili, T. W. Hänsch, and N. Picqué, Cavity-enhanced dual-comb spectroscopy[J]. Nature photonics, 2010, 4(1): 55-57.

[65] R. Liao, Y. Song, W. Liu, H. Shi, L. Chai, and M. Hu, Dual-comb spectroscopy

with a single free-running thulium-doped fiber laser[J]. Optics express, 2018, 26(8): 11046-11054.

[66] T. Yasui, Y. Kabetani, E. Saneyoshi, S. Yokoyama, T. Araki, Terahertz frequency comb by multifrequency-heterodyning photoconductive detection for high-accuracy, high-resolution terahertz spectroscopy[J]. Applied Physics Letters, 2006, 88(24): 241104.

[67] S. Okubo, K. Iwakuni, H. Inaba, K. Hosaka, A. Onae, H. Sasada, and F. Hong, Ultra-broadband dual-comb spectroscopy across 1.0–1.9 μm[J]. Applied Physics Express, 2015, 8(8): 082402.

[68] F. Keilmann, C. Gohle, and R. Holzwarth, Time-domain mid-infrared frequency-comb spectrometer[J]. Optics letters, 2004, 29(13): 1542-1544.

[69] I. A. Finneran, J. T. Good, D. B. Holland, P. B. Carroll, M. A. Allodi, and G. A. Blake, Decade-spanning high-precision terahertz frequency comb[J]. Physical review letters, 2015, 114(16): 163902.

[70] T. Ideguchi, A. Poisson, G. Guelachvili, T. W. Hänsch, and N. Picqué, Adaptive dual-comb spectroscopy in the green region[J]. Optics letters, 2012, 37(23): 4847-4849.

[71] J. Ye, Absolute measurement of a long, arbitrary distance to less than an optical fringe[J]. Optics letters, 2004, 29(10): 1153-1155.

[72] J. Lee, Y. J. Kim, K. Lee, S. Lee, and S. W. Kim, Time-of-flight measurement with femtosecond light pulses[J]. Nature photonics, 2010, 4(10): 716-720.

[73] G. Wu, M. Takahashi, H. Inaba, and K. Minoshima, Pulse-to-pulse alignment technique based on synthetic-wavelength interferometry of optical frequency combs for distance measurement[J]. Optics letters, 2013, 38(12): 2140-2143.

[74] K. N. Joo, and S. W. Kim, Absolute distance measurement by dispersive interferometry using a femtosecond pulse laser[J]. Optics express, 2006, 14(13): 5954-5960.

[75] R. Yang, F. Pollinger, K. M. Hagen, J. Tan, and H. Bosse, Heterodyne multi-wavelength absolute interferometry based on a cavity-enhanced electro-optic frequency comb pair[J]. Optics Letters, 2014, 39(20): 5834-5837.

[76] K. Minoshima, and H. Matsumoto, High-accuracy measurement of 240-m distance in an optical tunnel by use of a compact femtosecond laser[J]. Applied Optics, 2000, 39(30): 5512-5517.

[77] K. Minoshima, T. Tomita, H. Nakayama, Y. Yamaoka, and H. Matsumoto, Ultrahigh-resolution distance meter using a frequency comb of a femtosecond mode-locked laser[C]//International Conference on Ultrafast Phenomena. Optica Publishing Group, 2002: TuB3.

[78] N. Bobroff, Recent advances in displacement measuring interferometry[J]. Measurement Science and Technology, 1993, 4(9): 907.

[79] https://www.bipm.org/en/si-base-units/metre

[80] G. Berkovic, and E. Shafir, Optical methods for distance and displacement measurements[J]. Advances in Optics and Photonics, 2012, 4(4): 441-471.
[81] D. Nitzan, A. E. Brain, and R. O. Duda, The measurement and use of registered reflectance and range data in scene analysis[J]. Proceedings of the IEEE, 1977, 65(2): 206-220.
[82] P. J. Besl, Active, optical range imaging sensors[J]. Machine vision and applications, 1988, 1: 127-152.
[83] R. Dändliker, R. Thalmann, and D. Prongué, Two-wavelength laser interferometry using superheterodyne detection[J]. Optics letters, 1988, 13(5): 339-341.
[84] O. P. Lay, S. Dubovitsky, R. D. Peters, J. P. Burger, S. W. Ahn, W. H. Steier, H. R. Fetterman, and Y. Chang, MSTAR: a submicrometer absolute metrology system[J]. Optics Letters, 2003, 28(11): 890-892.
[85] M. Nisoli, S. Stagira, S. D. Silvestri, O. Svelto, S. Sartania, Z. Cheng, G. Tempea, C. Spielmann, and F. Krausz, Toward a terawatt-scale sub-10-fs laser technology[J]. IEEE Journal of selected topics in quantum electronics, 1998, 4(2): 414-420.
[86] Y. Yamaoka, L. Zeng, K. Minoshima, and H. Matsumoto, Measurements and numerical analysis for femtosecond pulse deformations after propagation of hundreds of meters in air with water-vapor absorption lines[J]. Applied optics, 2004, 43(29): 5523-5530.
[87] Y. S. Jang, G. Wang, S. Hyun, H. J. Kang, B. J. Chun, Y. J. Kim, and S. W. Kim，Comb-referenced laser distance interferometer for industrial nanotechnology[J]. Scientific Reports, 2016, 6(1): 1-10.
[88] N. Schuhler, Y. Salvadé, S. Lévêque, R. Dändliker, and R, Holzwarth, Frequency-comb-referenced two-wavelength source for absolute distance measurement[J]. Optics letters, 2006, 31(21): 3101-3103.
[89] Y. S. Jang, and S. W. Kim, Distance measurements using mode-locked lasers: a review[J]. Nanomanufacturing and Metrology, 2018, 1: 131-147.
[90] G. Wang, Y. S. Jang, S. Hyun, B. J. Chun, H. J. Kang, S. Yan, S. W. Kim, and Y. J. Kim, Absolute positioning by multi-wavelength interferometry referenced to the frequency comb of a femtosecond laser[J]. Optics express, 2015, 23(7): 9121-9129.
[91] J. Jin, Y. J. Kim, Y. Kim, S. W. Kim, and C. S. Kang, Absolute length calibration of gauge blocks using optical comb of a femtosecond pulse laser[J]. Optics Express, 2006, 14(13): 5968-5974.
[92] Z. Zhu, G. Xu, K. Ni, Q. Zhou, and G. Wu, Synthetic-wavelength-based dual-comb interferometry for fast and precise absolute distance measurement[J]. Optics express, 2018, 26(5): 5747-5757.
[93] K. N. Joo, and S. W. Kim, Absolute distance measurement by dispersive

interferometry using a femtosecond pulse laser[J]. Optics express, 2006, 14(13): 5954-5960.

[94] K. N. Joo, Y. Kim, and S. W. Kim, Distance measurements by combined method based on a femtosecond pulse laser[J]. Optics express, 2008, 16(24): 19799-19806.

[95] X. Zhao, X. Qu, and F. Zhang, Absolute distance measurement by dispersive interferometry using an electro-optic comb[C]//2019 International Conference on Optical Instruments and Technology: Optoelectronic Measurement Technology and Systems. SPIE, 2020, 11439: 269-277.

[96] S. Xiong, J. Chen, S. Zhou, Y. Wang, R. Zhang, and G. Wu, Influence of spectral resolution on dispersive interferometry of optical frequency comb[J]. Optics Communications, 2022, 503: 127464.

[97] M. Cui, M. G. Zeitouny, N. Bhattacharya, S. A. Van den berg, and H. P. Urbach, Long distance measurement with femtosecond pulses using a dispersive interferometer[J]. Optics express, 2011, 19(7): 6549-6562.

[98] S. A. Van den berg, S. V. Eldik, and N. Bhattacharya, Mode-resolved frequency comb interferometry for high-accuracy long distance measurement[J]. Scientific reports, 2015, 5(1): 14661.

[99] T. Kato, M. Uchida, and K. Minoshima, No-scanning 3D measurement method using ultrafast dimensional conversion with a chirped optical frequency comb[J]. Scientific Reports, 2017, 7(1): 3670.

[100] K. Minoshima, H. Matsumoto, Z. Zhang, and T. Yagi, Simultaneous 3-D imaging using chirped ultrashort optical pulses[J]. Japanese journal of applied physics, 1994, 33(9B): L1348.

[101] C. Weimann, M. Lauermann, F. Hoeller, W. Freude, and C. Koos, Silicon photonic integrated circuit for fast and precise dual-comb distance metrology[J]. Optics express, 2017, 25(24): 30091-30104.

[102] J. Lee, S. Han, K. Lee, E. Bae, S. Kim, S. Lee, S. W. Kim, and Y. J. Kim, Absolute distance measurement by dual-comb interferometry with adjustable synthetic wavelength[J]. Measurement Science and Technology, 2013, 24(4): 045201.

[103] H. Wu, T. Zhao, Z. Wang, K. Zhang, B. Xue, J. Li, M. He, and X. Qu, Long distance measurement up to 1.2 km by electro-optic dual-comb interferometry[J]. Applied Physics Letters, 2017, 111(25): 251901.

[104] C. Weimann, A. Messner, T. Baumgartner, S. Wolf, F. Hoeller, W. Freude, and C. Koos, Fast high-precision distance metrology using a pair of modulator-generated dual-color frequency combs[J]. Optics express, 2018, 26(26): 34305-34335.

[105] B. Xue, Z. Wang, H. Zhang, K. Zhang, Y. Chen, M. He, B. Lin, and H. Wu, Absolute distance measurement by self-heterodyne EO comb interferometry[J].

IEEE Photonics Technology Letters, 2018, 30(9): 861-864.
[106] M. G. Suh, and K. J. Vahala, Soliton microcomb range measurement[J]. Science, 2018, 359(6378): 884-887.
[107] R. Li, X. Ren, B. Han, M. Yan, K. Huang, Y. Liang, J. Ge, and H. Zeng, Ultra-rapid dual-comb ranging with an extended non-ambiguity range[J]. Optics Letters, 2022, 47(20): 5309-5312.
[108] J. Lee, S. Han, K. Lee, E. Bae, S. Kim, S. Lee, S. W. Kim, and Y. J. Kim, Absolute distance measurement by dual-comb interferometry with adjustable synthetic wavelength[J]. Measurement Science and Technology, 2013, 24(4): 045201.
[109] H. Zhang, H. Wei, X. Wu, H. Yang, and Y. Li, Absolute distance measurement by dual-comb nonlinear asynchronous optical sampling[J]. Optics Express, 2014, 22(6): 6597-6604.
[110] X. Zhao, X. Qu, F. Zhang, Y. Zhao, and G. Tang, Absolute distance measurement by multi-heterodyne interferometry using an electro-optic triple comb[J]. Optics Letters, 2018, 43(4): 807-810.
[111] P. Trocha, M. Karpov, D. Ganin, M. H. Pfeiffer, A. Kordts, S. Wolf, J. Krockenberger, P. M. Palomo, C. Weimann, S. Randel, W. Freude, T. J. Kippenberg, and C. Koos, Ultrafast optical ranging using microresonator soliton frequency combs[J]. Science, 2018, 359(6378): 887-891.
[112] G. Wu, S. Xiong, K. Ni, Z. Zhu, and Q. Zhou, Parameter optimization of a dual-comb ranging system by using a numerical simulation method[J]. Optics Express, 2015, 23(25): 32044-32053.
[113] G. Wu, Q. Zhou, L. Shen, K. Ni, X. Zeng, and Y. Li, Experimental optimization of the repetition rate difference in dual-comb ranging system[J]. Applied Physics Express, 2014, 7(10): 106602.
[114] Y. Li, Y. Cai, R. Li, H. Shi, H. Tian, M. He, Y. Song, and M. Hu, Large-scale absolute distance measurement with dual free-running all-polarization-maintaining femtosecond fiber lasers[J]. Chinese Optics Letters, 2019, 17(9): 091202.
[115] T. A. Liu, N. R. Newbury, and I. Coddington, Sub-micron absolute distance measurements in sub-millisecond times with dual free-running femtosecond Er fiber-lasers[J]. Optics Express, 2011, 19(19): 18501-18509.
[116] H. Shi, Y. Song, F. Liang, L. Xu, M. Hu, and C. Wang, Effect of timing jitter on time-of-flight distance measurements using dual femtosecond lasers[J]. Optics express, 2015, 23(11): 14057-14069.
[117] H. Shi, Y. Song, R. Li, Y. Li, H. Cao, H. Tian, B. Liu, L. Chai, and M. Hu, Review of low timing jitter mode-locked fiber lasers and applications in dual-comb absolute distance measurement[J]. Nanotechnology and Precision Engineering, 2018, 1(4): 205-217.

[118] B. Lin, X. Zhao, M. He, Y. Pan, J. Chen, S. Cao, Y, Lin, Q. Wang, Z. Zheng, and Z. Fang, Dual-comb absolute distance measurement based on a dual-wavelength passively mode-locked laser[J]. IEEE Photonics Journal, 2017, 9(6): 1-8.

[119] R. Li, H. Shi, H. Tian, Y. Li, B. Liu, Y. Song, and M. Hu, All-polarization-maintaining dual-wavelength mode-locked fiber laser based on Sagnac loop filter[J]. Optics Express, 2018, 26(22): 28302-28311.

[120] S. M. Link, D. J. H. C. Maas, D. Waldburger, and U. Keller, Dual-comb spectroscopy of water vapor with a free-running semiconductor disk laser[J]. Science, 2017, 356(6343): 1164-1168.

[121] T. Ideguchi, T. Nakamura, Y. Kobayashi, and K. Goda, Kerr-lens mode-locked bidirectional dual-comb ring laser for broadband dual-comb spectroscopy[J]. Optica, 2016, 3(7): 748-753.

[122] M. G. Suh, and K. J. Vahala, Soliton microcomb range measurement[J]. Science, 2018, 359(6378): 884-887.

[123] H. Shi, Y. Song, T. Li, C. Wang, X. Zhao, Z. Zheng, and M. Hu, Timing jitter of the dual-comb mode-locked laser: A quantum origin and the ultimate effect on high-speed time-and frequency-domain metrology[J]. IEEE Journal of Selected Topics in Quantum Electronics, 2018, 24(5): 1-10.

[124] D. R. Carlson, D. D. Hickstein, D. C. Cole, S. A. Diddams, and S. B. Papp, Dual-comb interferometry via repetition-rate switching of a single frequency comb[J]. arXiv preprint arXiv:1806.05311, 2018.

[125] G. Beheim, and K. Fritsch, Remote displacement measurements using a laser diode[J]. Electronics Letters, 1985, 3(21): 93-94.

[126] K. Määttä, J. Kostamovaara, and R. Myllylä, Profiling of hot surfaces by pulsed time-of-flight laser range finder techniques[J]. Applied Optics, 1993, 32(27): 5334-5347.

[127] A. Martin, D. Dodane, L. Leviandier, D. Dolfi, A. Naughton, P. O'Brien, T. Spuessens, R. Baets, G. Lepage, P. Verheyen, P. D. Heyn, P. Absil, P. Feneyrou, and J. Bourderionnet, Photonic integrated circuit-based FMCW coherent LiDAR[J]. Journal of Lightwave Technology, 2018, 36(19): 4640-4645.

[128] S. M. Beck, J. R. Buck, W. F. Buell, R. P. Dickinson, D. A. Kozlowski, N. J. Marechal, and T. J. Wright, Synthetic-aperture imaging laser radar: laboratory demonstration and signal processing[J]. Applied optics, 2005, 44(35): 7621-7629.

[129] N. Kuse, and M. E. Fermann. Frequency-modulated comb LIDAR[J]. Apl Photonics, 2019, 4(10): 106105.

[130] J. Riemensberger, A. Lukashchuk, M. Karpov, W. Weng, E. Lucas, J. Liu, and T. J. Kippenberg, Massively parallel coherent laser ranging using a soliton microcomb[J]. Nature, 2020, 581(7807): 164-170.

[131] J. Liu, H. Tian, E. Lucas, A. S. Raja, G. Lihachev, R. N. Wang, J. He, T. Liu, M. H. Anderson, W. Weng, S. A. Bhave, and T. J. Kippenberg, Monolithic piezoelectric control of soliton microcombs[J]. Nature, 2020, 583(7816): 385-390.

[132] A. Lukashchuk, J. Riemensberger, A. Tusnin, J. Liu, and T. J. Kippenberg, Microresonator based Coherent Random Waveform Parallel Laser Ranging[C]//CLEO: Applications and Technology. Optica Publishing Group, 2022: ATu4M. 3.

[133] E. Baumann, F. R. Giorgetta, I. Coddington, L. C. Sinclair, K. Knabe, W. C. Swann, and N. R. Newbury, Comb-calibrated frequency-modulated continuous-wave ladar for absolute distance measurements[J]. Optics letters, 2013, 38(12): 2026-2028.

[134] E. Baumann, F. R. Giorgetta, J. -D. Deschênes, W. C. Swann, I. Coddington, and N. R. Newbury, Comb-calibrated laser ranging for three-dimensional surface profiling with micrometer-level precision at a distance[J]. Optics express, 2014, 22(21): 24914-24928.

[135] P. E. Ciddor, Refractive index of air: new equations for the visible and near infrared[J]. Applied optics, 1996, 35(9): 1566-1573.

[136] B. Edlén, The refractive index of air[J]. Metrologia, 1966, 2(2): 71.

[137] P. L. Bender, and J. C. Owens, Correction of optical distance measurements for the fluctuating atmospheric index of refraction[J]. J Geophys. Res., 1965, 70: 2461-2562.

[138] K. Minoshima, K. Arai, and H. Inaba, High-accuracy self-correction of refractive index of air using two-color interferometry of optical frequency combs[J]. Optics Express, 2011, 19(27): 26095-26105.

[139] G. Wu, M. Takahashi, K. Arai, H. Inaba, and K. Minoshima, Extremely high-accuracy correction of air refractive index using two-colour optical frequency combs[J]. Scientific Reports, 2013, 3(1): 1-6.

[140] Y. S. Jang, and S. W. Kim, Compensation of the refractive index of air in laser interferometer for distance measurement: A review[J]. International Journal of Precision Engineering and Manufacturing, 2017, 18: 1881-1890.

[141] H. J. Kang, B. J. Chun, Y. S. Jang, Y. J. Kim, and S. W. Kim, Real-time compensation of the refractive index of air in distance measurement[J]. Optics Express, 2015, 23(20): 26377-26385.

[142] T. Tanaka, K. Akuzawa, T. Kato, and K. Minoshima, Shape Measurement Technique with Self-correction of Air Refractive Using a Single-color Comb Interferometer[C]//Conference on Lasers and Electro-Optics/Pacific Rim. Optica Publishing Group, 2022: CThA6D_03.

[143] Y. Nakajima, T. R. Schibli, B. Xu, and K. Minoshima, Absolute distance measurement method with optical frequency comb interferometer based on

balanced optical cross correlator and optical heterodyne technique[C]//CLEO: Science and Innovations. Optica Publishing Group, 2016: SM2H. 1.

Chapter 2. Principle: Electro-optic frequency combs and absolute distance measurement

In this chapter, the principle of EO combs and absolute distance measurement will be introduced in detail. The key devices of EO combs, EO modulators, are explained at first. Then various configurations of EO combs are displayed. By making use of time-to-frequency mapping, EO combs with different spectrum shape could be generated. The phase noise of the comb modes in EO combs are illustrated, especially the accumulated phase noise from the oscillator that drives the EO modulators. Taking advantage of the simple configuration and widely tunable comb mode spacing, EO combs have been applied in many fields, like absolute distance measurement, optical communications, etc.

The principle of distance measurement based on single wavelength interferometry, synthetic wavelength technique and microwave phase detection is explained in this chapter. Through measuring under-test distance using the three methods simultaneously, absolute distance measurement with nanometer precision in wide measurement range is achievable.

2.1 Electro-optic frequency combs (EO combs)

2.1.1 Electro-optic modulators

An electro-optic modulator (EO modulator) is a kind of optical devices that can control the power, phase or polarization of an input optical field by making use of electro-optic effect. The electro-optic effect is the phenomenon that the refractive index of a material changes according to the electric field which is applied to a material. The refractive index of the material with respect to the applied electric field could be expressed by

$$n = n_0 + \gamma E + hE^2 + \cdots \tag{2-1}$$

where n_0 is the refractive index of the material when no electric field is applied, γ is linear electro-optic coefficient, h is second-order electro-optic coefficient and E is the electrical field. The second item of equation (2-1) indicates that the refractive

index of the material changes linearly with the applied electric field. This phenomenon is well-known as linear electro-optic effect or Pockels effect, which is investigated by Pockels [1][2]. Pockels effect only exist in noncentrosymmetric materials because it is a second-order nonlinear process. Typical noncentrosymmetric materials include lithium niobate (LiNbO3), lithium tantalate (LiTaO3), potassium di-deuterium phosphate (KDP), β-barium borate (BBO), potassium titanium oxide phosphate (KTP), gallium arsenide (GaAs), indium phosphide (InP), and so on. The third item of equation (2-1) indicates a third-order nonlinear process which the refractive index of the material changes quadratically with the applied electric field [3]. This effect can appear in any materials and is often named as Kerr effect. Kerr effect is much weaker Pockels effect in most cases, except in centrosymmetric materials. In this thesis, it is focused only on Pockels effect since it is mainly used in commercial electro-optic modulators.

Taking a noncentrosymmetric crystal KDP as an example, the index ellipsoid is rotational symmetric when no electrical field is applied, which is expressed by

$$\frac{x^2}{n_x^2}+\frac{y^2}{n_y^2}+\frac{z^2}{n_z^2}=1, n_x=n_y=n_o, n_z=n_e \tag{2-2}$$

where $(x,\ y,\ z)$, n_o and n_e are principal axes, ordinary refractive index and extraordinary refractive index, respectively. When applying an electrical field E_z on the crystal along z axis, these principal axes are modified. The index ellipsoid is then expressed by

$$\frac{x'^2}{n_{x'}^2}+\frac{y'^2}{n_{y'}^2}+\frac{z'^2}{n_{z'}^2}=1,$$
$$n_{x'}=n_o-\frac{1}{2}n_o^3\gamma_{63}E_z, \qquad n_{y'}=n_o+\frac{1}{2}n_o^3\gamma_{63}E_z, \qquad n_{z'}=n_e \tag{2-3}$$

where γ_{63} is electro-optic coefficient. Due to the external electrical field, both the x and y principal axes rotate 45 degrees, while the z principal axis doesn't. The axes x', y', z' are named as new principal axes. $n_{x'}$ and $n_{y'}$ are both modified and no longer equal. As a result, when a beam of light propagates along z principal axis of the material, a small optical path difference is induced between x' and y' polarization states of the input light. This means that a phase delay that is related to the applied electric field is printed onto the incident light. Therefore, by controlling the electric field that applied to the crystal, phase and polarization of the input light could be modulated. Intensity modulation of the input could be realized by combining

the material with other optical devices like waveplates and polarizers. In this section, the principle of phase modulator, intensity modulator and polarization modulator are described sequentially.

Polarization modulator. Any polarized light can be resolved into two orthogonally linear polarized components. The phase relation between the two linear polarized components corresponds to the polarization state of the original light one-by-one. So a linear polarized light, that is incident to the KDP along x or y axis, could be considered as the composition of two linear polarized components that along x' and y' axes. When an electrical field E_z is applied to the KDP, a phase delay between the two components is induced. The amount of the phase delay is $\Delta\varphi = \frac{2\pi}{\lambda}(n_{y'} - n_{x'})L = \frac{2\pi}{\lambda}n_o^3\gamma_{63}V = \pi\frac{V}{V_\pi}$, where $V_\pi = \frac{\lambda}{2n_o^3\gamma_{63}}$ is half wave voltage and $V = E_z L$ is the voltage along z axis. Through controlling the intensity of the external electric field, the polarization of the incident light could be modulated.

Phase modulator. In a phase modulator, the polarization state of the incident light is parallel to the x' axis or y' axis, which is guaranteed by a polarizer before the crystal, as explained in Fig. 2-1. As a result, the polarization state of the incident light doesn't change with the electrical field. When the incident light is from a continuous wave laser with center frequency ω_c and amplitude E_0, the optical field of the incident laser is expressed by $E_{in}(t) = E_0 \exp(j\omega_c t)$. Assume the phase modulator is driven by a sinusoidal signal with amplitude V_{PM} and angular frequency ω_{RF}, the RF signal is expressed by $V(t) = V_{PM} \times \sin(\omega_{RF} t)$ Then the output optical field from the phase modulator in the time domain is expressed as

$$\begin{aligned} E_{out}(t) &= E_0 \exp(j\omega_c t) * \exp(j\pi V(t)/V_\pi) \\ &= E_0 \sum_{n=-\infty}^{\infty} J_N(\pi V_{PM}/V_\pi) * \exp[j(n\omega_{RF} + \omega_c)t] \end{aligned} \tag{2-4}$$

where $V_\pi = \lambda/n_o^3\gamma_{63}$ is half wave voltage of the phase modulator, J_N is the Bessel function of first kind [4][5]. The maximum phase delay induced by the phase modulator is $\Delta\varphi = \pi V_{PM}/V_\pi$, which is defined as modulation depth of the phase modulator.

By applying Fourier transform to equation (2-4), the output optical field in frequency domain is

$$\tilde{E}_{out}(\omega) = E_0 \sum_{n=-\infty}^{\infty} J_N(\Delta\varphi) * \delta(\omega - n\omega_{RF} - \omega_c)] \tag{2-5}$$

According to equation (2-5), symmetrical sidebands are generated around the input CW laser. The frequencies of them are defined by $\omega_n = n\omega_{RF} + \omega_c$. These

sidebands are equally spaced with frequency interval of ω_{RF}. The number of the sidebands is determined by the modulation depth. More sidebands are generated by a phase modulator with higher modulation depth. Therefore, a phase modulator with ultra-low half-wave voltage and high tolerance to electrical power is preferred in frequency comb generations.

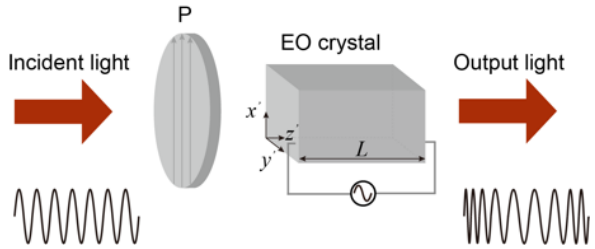

Fig. 2-1 Principle of phase modulators. P: polarizer; EO crystal: electro-optic crystal. The polarization orientation of the polarizer is parallel to the x' axis.

Intensity modulator. As is explained above, the polarization state of the incident light could be modulated by a polarization modulator. By placing a polarizer at the output of the polarization modulator, particular polarization component could be extracted. The intensity of this polarization component varies according to the driven signal of the polarization modulator. Therefore, an intensity modulator is obtained.

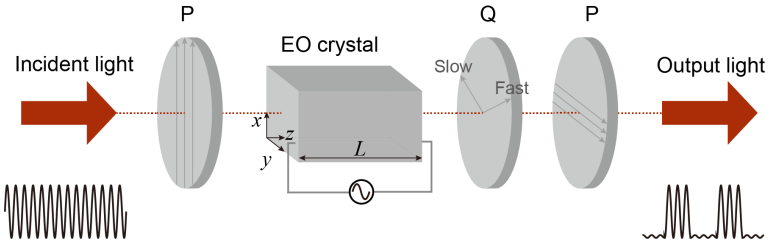

Fig. 2-2 Principle of intensity modulators. P: polarizer; EO crystal: electro-optic crystal; Q: quarter waveplate.

The scheme of a basic intensity modulator is illustrated in Fig. 2-2. An electro-optic crystal and a quarter waveplate are sandwiched between two polarizers with orthogonal polarization orientation. The x principal axis is at 45° from the fast axis and slow axis of the quarter waveplate. The polarization orientations of the two polarizers are parallel to the x and y principal axes of the crystal, respectively. The incident light is linearly polarized by the first polarizer and is resolved to two polarization components along the x' and y' axes. The phase retardation between them that induced by the external electrical field is $\Delta\varphi = \frac{2\pi}{\lambda}(n_{y'} - n_{x'})L = \frac{2\pi}{\lambda}n_o^3\gamma_{63}V = \pi\frac{V}{V_\pi}$. Another π/2 phase delay is induced by the quarter waveplate. So the total phase

delay is $\Delta\Phi = \pi\frac{V}{V_\pi} + \pi/2$. These two components are partly transmitted from the second polarizer. Therefore, the transmission function of the intensity modulator is [6]

$$\mathrm{T} = sin^2(\Delta\Phi/2). \tag{2-6}$$

The transmission characteristics of the intensity modulator is plotted in Fig. 2-3. Attributing to the fixed $\pi/2$ phase delay induced by quarter waveplate, the intensity modulator is operating at QUAD+ point. At this point, the response of the intensity modulator is almost linear for small driven signal. Besides, the intensity modulator can also be biased at MIN, MAX and QUAD- operating point by simply tuning the bias voltage. The ratio between the maximum transmission and minimum transmission is the extinction ratio of the intensity modulator. Typical extinction ration of a commercial intensity modulator is 20~25 dB. Cascading two or more intensity modulators can improve the overall extinction ratio.

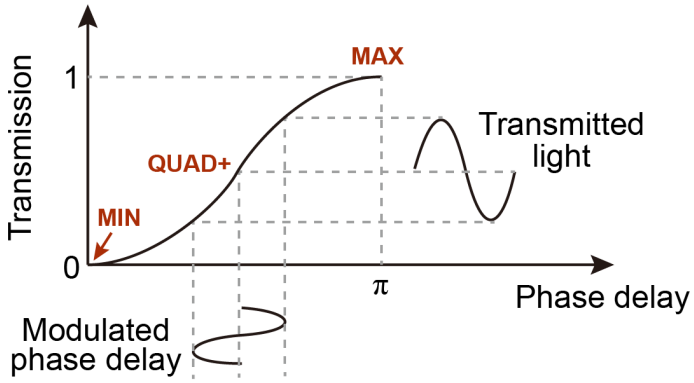

Fig. 2-3 Transfer function of an intensity modulator that biased at QUAD+ point.

In the above configurations, the electrical field is applied to the crystal along the propagation direction of the incident light. This is so-called longitudinal modulation. However, in these configurations, the half-wave voltage is usually at kilovolt level, which is too high for practical usage. Instead of the longitudinal modulation, a transverse modulation of the electro-optic crystal which provides a much smaller half-wave voltage is commonly used in fabrication. The half-wave voltage in transverse modulation is d/L times smaller than in longitudinal modulation, where d and L are the height and length of the crystal. By making use of transverse modulation, the half-wave voltage of commercial EO phase modulator or intensity modulators usually varies from 3 to 10 V.

In addition, to achieve high modulation bandwidth of an EO modulator, the incident light is usually bounded in a waveguide that printed on the electro-optic crystal. Mach-Zehnder interferometers are widely utilized in these waveguides. The

modulators with Mach-Zehnder interferometer are called as Mach-Zehnder modulator. According to the crystal orientation, a single arm or both two arms of the Mach-Zehnder interferometer could be driven by external electrical fields. The interference between the two arms leads to the phase modulation or intensity modulation to the incident light. Typical designs of Mach-Zehnder modulators are shown in Fig. 2-4.

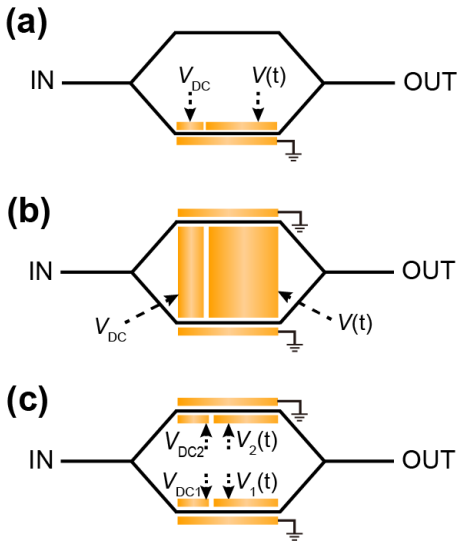

Fig. 2-4 Typical designs of commercial EO Mach-Zehnder modulators. (a): A single arm of the Mach-Zehnder interferometer is driven by external electrical signal. (b): Single-drive Mach-Zehnder modulator. (c): Dual-drive Mach-Zehnder modulator.

In Fig. 2-4 (a), one arm of the Mach-Zehnder modulator is modulated by a time variable electrical field $V(t)$ with bias voltage of V_{DC}. Assume the input optical field is E_{in}, the output optical field is expressed as

$$E_{out} = 1/2E_{in} * [1 + \exp(j\pi V(t)/V_\pi) \times \exp(j\pi V_{DC}/V_\pi)]. \quad (2\text{-}7)$$

The Mach-Zehnder modulator is regarded as an intensity modulator in this case. In Fig. 2-4 (b), the two arms of the Mach-Zehnder are covered by same electrodes. The driven electrical fields to the two arms are either same or opposite, depending on the design. Mach-Zehnder modulator with this configuration is named as single-drive Mach-Zehnder modulator. The output optical field is expressed as $E_{out} = 1/2E_{in} * [\exp(j\pi(V_1(t) + V_{DC1})/V_\pi) + \exp(j\pi(V_2(t) + V_{DC2})/V_\pi)]$, where $V_1(t) = V_2(t)$ or $V_1(t) = -V_2(t)$. When $V_1(t) = V_2(t)$, the Mach-Zehnder works at push-push mode and is equal to a pure phase modulator. The Mach-Zehnder works at push-pull mode and is equal to a pure intensity modulator when $V_1(t) = -V_2(t)$. Besides, the two arms of the interferometer can also be separately modulated, which is well known as

dual-drive Mach-Zehnder modulator, as shown in Fig. 2-4 (c).

The detail design and manufacture process of EO modulators are much more complex than explained here. A lot of factors should be taken care in the fabrication, such as thermal effect, orientation, deformation and resonance of the crystal, etc. So far, there are many companies produce commercial EO modulators, like EOSPACE, iXblue, Thorlabs, JENOPTIC, and so on. These modulators are suitable to various applications. For example, phase modulators with ultra-low half wave voltage could be applied in broadband EO comb generation. Intensity modulators with high modulation bandwidth could be used as optical switch with fast response time. High speed optical communications, power stabilization and frequency stabilization of a laser are also achievable through making use of EO modulators.

2.1.2 EO combs generation with electro-optic modulators

Time-to-frequency mapping.

At first, let's consider a chirp-free pulse from an optical frequency comb with its pulse shape and spectrum plotted in Fig. 2-5. The envelope of the pulse is determined by the interference among all the frequency components. When the pulse undergoes large amount dispersion, it stretches a lot due to the time delay between these frequency components. As long as the dispersion is large enough, the time delay between these frequency components is large enough. As a result, all the frequency components will be totally separated in the time domain. Thus, the spectrum shape of the frequency comb is mapped to the pulse shape in time domain, as illustrated in Fig. 2-5. This process is called as frequency-to-time mapping. The dispersion module can be long fiber, grating pair or other devices. Through mapping the spectrum shape of an OFC to pulse shape in time domain, spectrum analysis of the OFC is enabled via detecting the pulse train with a high-speed oscilloscope. This approach is applied widely in dispersive Fourier transform spectroscopy [7][8][9][10].

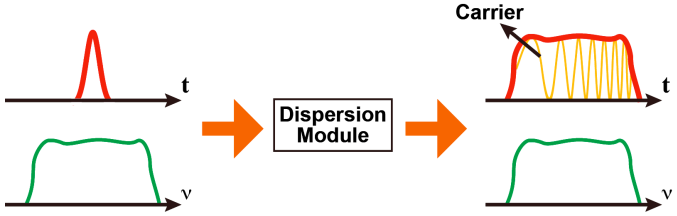

Fig. 2-5 Frequency-to-time mapping. Red curves show the pulse shape in time domain. Green curves indicate the spectrum shape in frequency domain.

On the contrary, the pulse shape in time domain can be printed to the spectrum shape when a strong parabolic phase is imposed on the pulse, as explained in Fig. 2-6. Assume the input pulse is a long pulse with spectrum bandwidth of $\Delta\nu$. Due to the strong parabolic phase modulation to the input pulse, the output pulse has linearly distributed instantaneous frequency. This means that new frequency components are generated around the input carrier frequency. The intensity of these frequency components is determined by the pulse shape. As a result, the spectrum shape of the output light has the same structure with the pulse shape in time domain. This process is time-to frequency mapping [11][12]. The rate at which the instantaneous frequency changes is chirp rate. The chirp rate induced by the parabolic phase modulation should be far more than $\Delta\nu^2/4\pi$ in order to achieve time-to-frequency mapping [13]. The 3-dB bandwidth of the output spectrum is proportional to the chirp rate. Attributing to the linear chirp, the pulse can be compressed easily through dispersion management. Therefore, a broad spectrum and corresponding narrow pulse are obtained. The device that can provide strong parabolic phase modulation is called as time lens. There are many ways to implement time lens, such as phase modulating the input pulse through an EO phase modulator [14][15], cross correlating the input pulse with another highly linear chirped pulse [16][17].

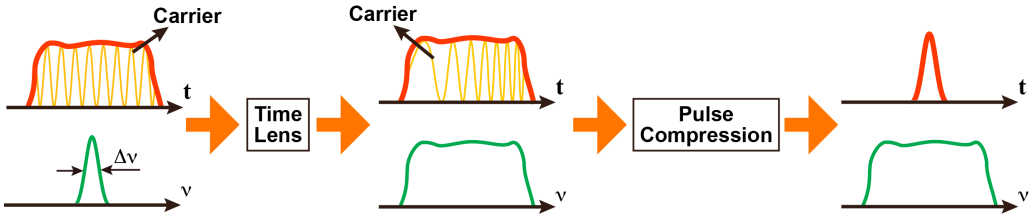

Fig. 2-6 Time-to-frequency mapping. Red curves show the pulse shape in time domain. Green curves indicate the spectrum shape in frequency domain.

EO comb generation with EO modulators.

According to time-to-frequency mapping, two elements are required to generate an optical frequency comb: a pulse train and parabolic phase modulation with same period as the pulse train. A pulse train with narrow bandwidth could be obtained by modulating a continuous wave laser with EO intensity modulator(s). The pulse shape is determined by the bias voltage and driven signal(s) of the intensity modulator(s). Periodic parabolic phase modulation is achieved by modulating the input pulse train through EO phase modulators. In practical, sinusoidal signals are often applied to these phase modulators since the temporal phase is approximate to parabolic around

the peaks or valleys. Another reason of utilizing sinusoidal signals is their easy realizability compared to the ideal periodically parabolic signals. Therefore, EO combs can be realized by modulating a continuous wave laser through cascaded EO modulators. Typical configurations of EO combs are displayed in Fig. 2-7.

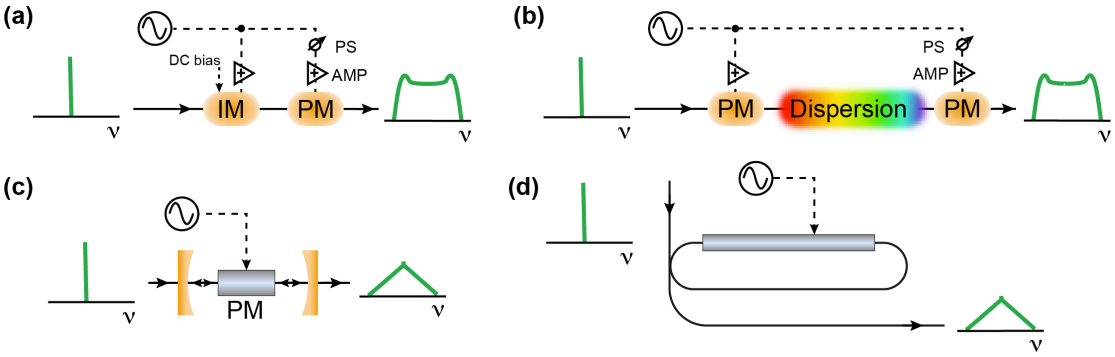

Fig. 2-7 Representative configurations of EO comb generation. IM: intensity modulator; PM: phase modulator; AMP: microwave amplifier; PS: phase shifter.

Fig. 2-7 (a) shows the versatile setups of an EO comb. A pulse train with pseudo-square shape is obtained by modulating a CW laser with an intensity modulator, whose bias voltage and amplitude of its driven signal are both set to half of V_π. After inputting the pulse train to a phase modulator that driven by a sinusoidal signal, an EO comb with flat-top shaped spectrum is generated [18][19]. Although only one phase modulator is applied in Fig. 2-7 (a), several cascaded phase modulators can be sequentially connected to obtain an EO comb with broader spectrum [14][20][21][22][23][24][25][26][27]. For example, an EO comb with 39-nm spectrum bandwidth and 25-GHz comb spacing is achieved by applying eight phase modulators [28]. However, the temporal phase of a sinusoidal signal gradually deviates from quadratic phase as one moves away from its peaks or valleys. These aberrations cause the power fluctuation of high order comb modes at the spectrum edges, which indicating the degradation of the spectrum flatness. Many efforts have been made to improve the spectrum flatness [29][30][31][32][33]. The most straightforward way is to sharpen the pulse and minimize the temporal phase deviation from quadratic simultaneously. Special designed RF waveforms with temporal phase better approximates quadratic could be used to solve the problem, while sharper pulse could be realized by cascade two intensity modulators. A very flat EO comb that contains 38 comb lines within 1 dB variation is demonstrated by imposing fundamental and scaled second harmonics on a phase modulator [29]. In

addition, Dou et al. found that the spectrum flatness is related to the bias voltage of the intensity modulator. Through biasing the intensity modulator at 0.35 times Vπ, 15 comb lines within 1 dB flatness is achieved [32].

According to time-to-frequency mapping, the spectrum shape of an EO comb based on cascaded modulators is determined by the pulse shape. Thus, by manipulating the pulse in time domain, EO combs with various and variable shape are achievable. Besides flat-topped EO combs, EO combs with Gaussian shape have also drawn a lot of interests because of their applications in optical communication and optical arbitrary waveform generation. Since a pulse train with Gaussian profile is realizable by carving the output of an CW laser with cascaded intensity modulators, an EO comb with Gaussian shape could be obtained. The bias voltage and the amplitude of the driven signal of these intensity modulators should be carefully chosen. For instance, two intensity modulators biased at QUAD accompanied with another intensity modulator that biased at MAX are successfully utilized to generate Gaussian-shaped pulse. The amplitude of the driven signal to these modulators should match their bias voltage, which means $V_\pi/2$ amplitude to the first two IMs and V_π amplitude to the third IM [34][35].

Fig. 2-7 (b) illustrates another common configuration of EO comb generation, which intrinsically equals to the setup in Fig. 2-7 (a). The combination of a phase modulator and a dispersion medium plays the role of a pulse train generator [13][36]. Phase modulation to the pulse train leads to the generation of an EO comb [37].

Due to the cavity-less configuration in Fig. 2-7 (a) and (b), the comb mode spacing of these EO combs can be tuned in large tuning range with high tuning speed. The comb mode spacing could range from several hundreds of MHz to several tens of GHz. Compared to the optical frequency combs based on mode-locked lasers and microresonators, these advantages only exist in EO combs.

Besides the above configuration, placing a phase modulator inside a Fabry-Perot cavity is another popular scheme of EO comb generation, as shown in Fig. 2-7 (c) [38][39][40][41][42][43]. The modulation frequency of the phase modulator should match with the free-spectral-range (FSR) of the cavity. Sometimes active feedback is necessary to ensure this relationship [44]. Meanwhile, the cavity plays an important role of narrow spectrum filter to all the comb modes, attributing to the cavity's Lorentzian transfer function [45]. As a consequence, the phase noise of the comb modes at high Fourier frequency is reduced. Notice that the spectrum shape of this

kind of EO comb is dominated by the transfer function of the cavity, rather than time-to-frequency mapping.

More recently, embedding a phase modulator in a microresonator has attracted wide interests due to its compactness and integration, as shown in Fig. 2-7 (d) [46][47][48][49][50]. An EO comb with 20-dB spectrum bandwidth of 35 nm is reported in Ref. [47]. Through careful dispersion management of the waveguide, octave spanning EO comb is feasible. However, the tuning flexibility of the comb mode spacing is no longer allowed in EO combs with cavity scheme.

In this sub-section, the basic principle of EO comb generation and representative schemes of EO combs are introduced. Based on the aforementioned configurations, EO combs emit ultra-short pulses with octave spanning spectrum have been demonstrated [24][51]. Fully stabilization of an EO comb is achieved by phase locking the EO comb to another fully stabilized OFC or directly phase locking both repetition rate and carrier-envelope offset frequency [14][52][53].

2.1.3 Phase noise of comb modes in EO combs

There are many possible noise sources in EO combs, such as phase noise of the CW laser, phase noise of the RF oscillator, amplitude noise of the CW laser, timing jitter, slow drifting of the modulators, residual phase or amplitude modulation and so on [6]. Among these noise sources, the phase noise of the CW laser and the RF oscillator contribute the most. Assume the phase noise of the CW laser and the RF oscillator are static, which are expressed by $\Delta\varphi_c$ and $\Delta\varphi_{RF}$, respectively. Then, the optical field of the CW laser is expressed through $E_{in} = E_0 \exp(j\omega_c t) \exp(j\Delta\varphi_c)$. The sinusoidal signal that drives the phase modulators is expressed by $V_{PM}(t) = V_{PM} * \sin(\omega_{RF}\mathrm{t} + \Delta\varphi_{RF})$. For the sake of simplicity, let's take EO combs with cavity-less configuration as an example to explain the phase noise of comb modes. After the CW laser is modulated by the phase modulators, the output field in time domain is expressed as

$$\begin{aligned} E_{out} &= E_0 \exp[j(\omega_c t + \Delta\varphi_c)] * \exp\left(\frac{j\pi V_{PM} * \sin(\omega_{RF}\mathrm{t} + \Delta\varphi_{RF})}{V_\pi}\right) \\ &= E_0 \sum\nolimits_{n=-\infty}^{\infty} \left\{ J_N\left(\frac{\pi V_{PM}}{V_\pi}\right) \times \exp[j(\Delta\varphi_c \right. \\ &\qquad \left. + n \times \Delta\varphi_{RF})] \times \exp[j(n\omega + \omega_c)t] \right\} \end{aligned} \tag{2-8}$$

The Fourier transform of equation (2-8) shows the optical field in frequency domain:

$$E_{out} = E_0 \sum_{n=-\infty}^{\infty}\{J_N(\pi V_{PM}/V_\pi) \times \exp\left[j(\Delta\varphi_c + n \times \Delta\varphi_{RF})\right] \times \delta(\omega - n\omega_{RF} - \omega_c)]\}. \quad (2\text{-}9)$$

As a result, the comb modes located at $\omega_n = n\omega_{RF} + \omega_c$ has the phase fluctuation of $\Delta\varphi_c + n \times \Delta\varphi_{RF}$. This indicates the phase noise of the RF oscillator diffuses to the comb modes in proportion to their comb mode number, while the phase noise of the CW laser diffuses without magnification [54][55]. The process of phase noise accumulation from RF oscillator to all the comb modes is called as accumulated phase noise. As a result, the high order comb modes have higher phase noise and larger linewidth, as illustrated in Fig. 2-8 (a) [24]. The noisier RF oscillator, the higher comb modes' phase noise. Considering the ultra-stable long-term performance of CW laser and ultra-low short-term drifting of the RF oscillator, the phase noise of the comb modes is dominated by the phase noise of CW laser at low Fourier frequency (< 1 kHz), while it is dominated by the accumulated phase noise at high Fourier frequency (> 1 kHz). This relationship is illustrated in Fig. 2-8 (b) [23]. Note that the frequency noise and phase noise are just different ways to describe the same phenomenon. Therefore, the accumulated phase noise is problematic, especially for broadband EO combs.

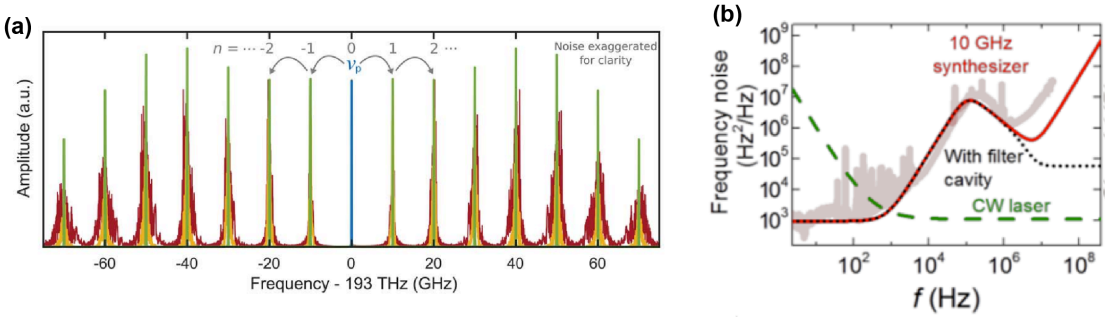

Fig. 2-8 (a) Red curve: accumulated phase noise on high order comb modes of an EO comb. Yellow curve: spectrum of an EO comb after filtered by a Fabry–Pérot cavity. Green curve: spectrum of an ideal EO comb. From Ref. [24]. (b) The contribution of frequency noise of the CW laser and RF synthesizer to the frequency noise of 19340th comb mode in EO comb. From Ref. [23].

Fortunately, several methods have been reported to suppress the accumulated phase noise. For instance, the phase noise of comb modes could be reduced through phase locking two comb modes in an EO comb to a fully stabilized mode-locked fiber

laser [52][53]. More phase noise could be suppressed with higher locking bandwidth of the phase-locked loops. Locking bandwidth of 300 kHz is achievable with carefully design of the system [53]. However, the phase noise that beyond the locking bandwidth is hard to be reduced in this case. Meanwhile, the reference fully stabilized optical frequency comb increase the system complexity.

In addition, a resonator, such as a Fabry–Pérot cavity or a microresonator, has been demonstrated as a powerful tool to reduce the accumulated phase noise. Attributing to its Lorentzian transfer function [45], the accumulated phase noise that far beyond the locking bandwidth of any phase-locked loops can be reduced. As the dashed black curve shown in Fig. 2-8 (b), the accumulated phase noise is greatly suppressed. It was found that either a Fabry–Pérot cavity after EO comb generation or a built-in Fabry–Pérot cavity is beneficial to the reduction of accumulated phase noise. In fact, a Fabry–Pérot cavity is essential to detect the carrier-envelope offset frequency through *f*-2*f* method [24], although the wide tuning range of repetition rate is not allowed anymore.

2.1.4 Advantages of EO combs

EO combs have many advantages, like flexible tunability and high comb mode power, etc.

Flexible tunability. According to time-to-frequency mapping, the pulse shape and the spectrum shape of EO combs are both tunable. This could be achieved by manipulating the bias voltage and the RF signals to the EO modulators [5][25][56][57][58]. Flat-top shaped EO combs and Gaussian shaped EO combs have been introduced in Section 2.1.2. In addition, the center wavelength and the repetition rate of the EO combs are determined only by the CW laser and the frequency of the RF signal, respectively. Hence both the center wavelength and the repetition rate are tunable. Since the operating bandwidth of EO modulators are often at tens of nm level, the center wavelength of the generated EO comb is tunable among this range. The repetition rate of EO combs can range from several MHz to tens of GHz, where the electro-optic bandwidth of the EO modulators sets the upper limit. Meanwhile, the tuning speed of repetition could be extremely high, which cannot be realized in neither mode-locked fiber lasers nor microresonators. For example, the maximum sweep rate of a RF synthesizer (Keysight, E8257D) is 400 MHz/ms when the output

frequency is > 3.2 GHz. It's worth to note that the wide tunability of the repetition rate is not allowed in EO combs with cavity configuration.

High comb mode power. Larger comb mode spacing, fewer comb modes located in certain bandwidth, higher power for each comb mode. For instance, in a 10-GHz flat-topped EO comb with 40 comb modes and 100 mW output power, the power of each comb mode is 2.5 mW. This is 100 times higher than that in a 100-MHz mode-locked laser with same spectrum bandwidth. This property is very attractive in many applications, such as high sensitivity spectroscopy, distance measurement, optical communications, etc.

2.2 Absolute distance measurement

2.2.1 Distance measurement based on single wavelength interferometry

The principle of single-wavelength-interferometry based distance measurement can be explained in Fig. 2-9. A continuous wave laser, or a longitudinal mode from an optical frequency comb, is split into reference path and target path by a beam splitter. These two paths are reflected by a reference mirror and a target mirror, respectively. Next they are combined by the beam splitter and interfere at the photodetector. Through detecting the phase of the interference signal, the under-test distance could be calculated. By using the laser wavelength as 'ruler', distance measurement with nanometer resolution is achievable. Assume the optical wavelength of the continuous wave laser is λ, the under-test distance is

$$D = \frac{1}{n}\left(N\frac{\lambda}{2} + \frac{\varphi\lambda}{4\pi}\right), \tag{2-10}$$

where φ is the measured phase shift, n is the air refractive index and N is an integer. Here, the non-ambiguity range of the measurement is $\lambda/2$. To achieve absolute distance measurement, the value of N should be measured through other coarse measurements.

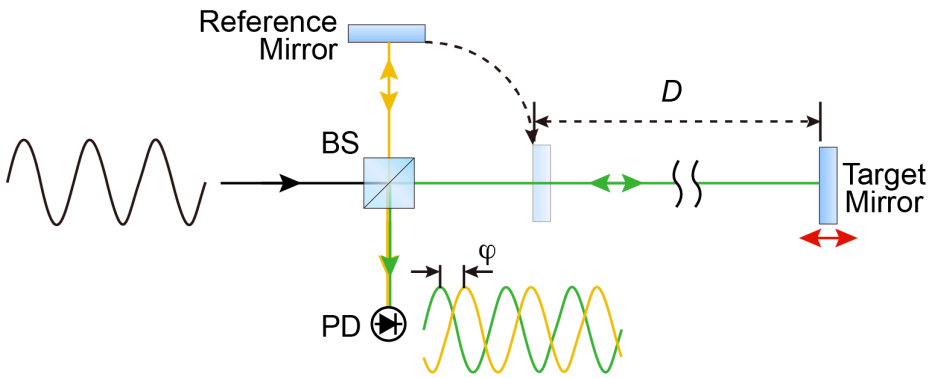

Fig. 2-9 Principle of single-wavelength-interferometry based distance measurement. BS: beam splitter; PD: photodetector.

It's not necessary to strictly filter one longitudinal mode from an optical frequency comb to realize single wavelength interferometry. Actually, it's not easy to select single longitudinal mode from an optical frequency comb, especially when the comb spacing is on the order of tens of MHz. Researchers have demonstrated single wavelength interferometry using a group of longitudinal modes from an optical frequency comb. This group of longitudinal modes could be selected by band pass filtering the optical frequency comb. In this case, λ is the effective center wavelengths of these longitudinal modes [59]. Correspondingly, the phase shift of the interference signal is the integration of phase shift from all the longitudinal modes in the pass bands.

According to the frequency of the interference signal, single-wavelength interferometry can be implemented via homodyne detection or heterodyne detection. In homodyne detection, the interference signal is a DC signal. In contrast, the frequency of the interference signal deviates from zero in heterodyne detection, which could be realized by inserting a frequency shifter in the reference path. Compared to homodyne detection, heterodyne detection is preferred, since the influence of DC or low frequency signal components such as ambient light interference or laser power drift on the measurement results is effectively avoided.

2.2.2 Absolute distance measurement based on synthetic wavelength technique

Through measuring the distance with synthetic wavelength technique and single wavelength interferometry, non-ambiguity range is extended, as illustrated in Fig. 2-10. In this case, two CW lasers, or two longitudinal modes from an optical

frequency comb, are utilized to measure the same under-test distance simultaneously. So the under-test distance is explained by

$$D = \frac{1}{n_1}\left(N_1\frac{\lambda_1}{2} + \frac{\varphi_1\lambda_1}{4\pi}\right) = \frac{1}{n_2}\left(N_2\frac{\lambda_2}{2} + \frac{\varphi_2\lambda_2}{4\pi}\right), \tag{2-11}$$

where λ_1 and λ_2 are the wavelength of the two CW lasers or the two longitudinal modes, φ_1 and φ_2 are the phase shift of the interferometer signal contributed by the two lasers, n_1 and n_2 are air refractive index at the two wavelengths, N_1 and N_2 are the integers, respectively. If the wavelengths of the two CW lasers are close to each other, n_1 and n_2 are approximately equal.

From equation (2-11), one can derive that

$$D = \frac{1}{n_g}\left(M\frac{\Lambda}{2} + \frac{\Phi\Lambda}{4\pi}\right), \tag{2-12}$$

where $\Lambda = \lambda_1\lambda_2/(\lambda_2 - \lambda_1)$ is the synthetic wavelength, $\Phi = \varphi_1 - \varphi_2$ is the corresponding phase, n_g is the group refractive index of air corresponding to the synthetic wavelength and M is an integer. In this case, the non-ambiguity range is extended to $\Lambda/2$, which is tens or hundreds times of the optical wavelength. By tuning the frequency of one of the CW lasers or choosing different longitudinal modes in the optical frequency comb, one can obtain different synthetic wavelengths. Through applying these synthetic wavelengths in distance measurement, further non-ambiguity range extension is realizable [60].

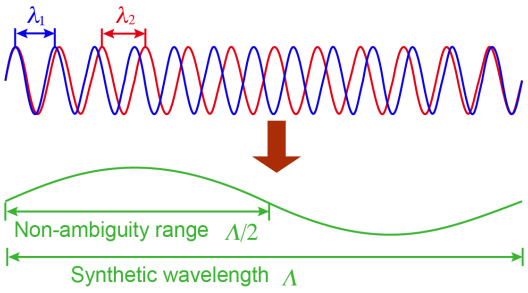

Fig. 2-10 Illustration of synthetic wavelength.

2.2.3 Absolute distance measurement based on microwave phase detection

Through photo-detecting the pulse train from an optical frequency comb, one can observe the repetition rate and its high order harmonics in radio frequency domain. The phase of these harmonics changes according to the time delay that the pulse train undergoes. Therefore, the under-test time delay, hence the under-test distance, can be obtained by detecting the phase of these harmonics. This method is called as microwave phase detection. Distance measurement with micrometer measurement

precision in hundreds of meters measurement range have been reported through microwave phase detection [61]. The under-test distance is explained by

$$D = \frac{1}{n_g}\left(K\frac{\Lambda_m}{2} + \frac{\Phi_m \Lambda_m}{4\pi}\right), \tag{2-12}$$

where n_g is the group refractive index, Λ_m is the wavelength of the microwave, K is an integer. Λ_m is inversely proportional to the frequency of the harmonics. The advantageous of the microwave phase detection is that there is no dead zone in the whole measurement range.

Through combining the microwave phase detection, synthetic wavelength technique and single wavelength interferometry, absolute distance measurement with nanometer precision is realizable in the extended non-ambiguity range, as explained in Fig. 2-11. The measurement results through single wavelength interferometry, synthetic wavelength and microwave phase detection are labeled as D_p, D_g and D_m, respectively. Here distance measurement through microwave phase detection serves as coarse measurement, while distance measurement through single wavelength interferometry serves as precise measurement. To combine these methods, the measurement uncertainty of the coarse measurement must be less than the non-ambiguity range of the precise measurement. The integer of the precise measurement is determined by coarse measurement. For example, $M = \lfloor 2D_m/\Lambda \rceil$ and $N = \lfloor 2D_g/\lambda \rceil$, where $\lfloor\cdot\rceil$ means round down.

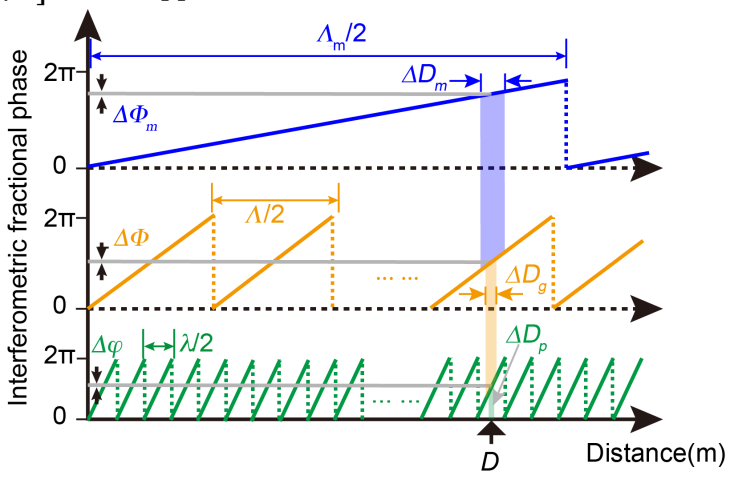

Fig. 2-11 Absolute distance measurement through combining three methods. Blue curve: distance measurement through microwave phase detection. $\Delta\Phi_m$ and ΔD_m are the measurement error of phase and distance, respectively. Orange curve: distance measurement through synthetic wavelength technique. $\Delta\Phi$ and ΔD_g are the measurement error of phase and distance, respectively. Green curve: distance measurement through single wavelength interferometry. $\Delta\varphi$ and ΔD_p are the measurement error of phase and distance, respectively.

2.3 Summary of this chapter

In this chapter, the principle of EO modulators, various configurations of EO combs and the phase noise of comb modes in EO combs are introduced. The advantages of EO combs include simple setup, wide tunability, high repetition rate and high comb mode power. Benefiting from these, EO combs have been widely utilized in telecommunications, arbitrary waveform generation, distance measurement and so on.

The principle of absolute distance measurement is also illustrated in this chapter. By combining several methods, high precision measurement can be realized in extended non-ambiguity range. Therefore, absolute distance measurement is realized.

2.4 References

[1] F. Pockels, Ueber den Einfluss elastischer Deformationen, speciell einseitigen Druckes, auf das optische Verhalten krystallinischer Körper[J]. Annalen der Physik, 1889, 273(5): 144-172.

[2] A. Kundt, Ueber das optische Verhalten des Quarzes im electrischen Felde[J]. Annalen der Physik, 1883, 254(2): 228-233.

[3] J. Kerr, XL. A new relation between electricity and light: Dielectrified media birefringent[J]. The London, Edinburgh, and Dublin Philosophical Magazine and Journal of Science, 1875, 50(332): 337-348.

[4] S. Ozharar, F. Quinlan, I. Ozdur, S. Gee, and P. J. Delfyett, Ultraflat optical comb generation by phase-only modulation of continuous-wave light[J]. IEEE photonics technology letters, 2007, 20(1): 36-38.

[5] A. Yariv, Optical electronics in modern communications[M]. Oxford University Press, USA, 1997.

[6] A. Parriaux, K. Hammani, and G. Millot, Electro-optic frequency combs[J]. Advances in Optics and Photonics, 2020, 12(1): 223-287.

[7] K. Goda, and B. Jalali, Dispersive Fourier transformation for fast continuous single-shot measurements[J]. Nature Photonics, 2013, 7(2): 102-112.

[8] J. Chou, D. R. Solli, and B. Jalali, Real-time spectroscopy with subgigahertz resolution using amplified dispersive Fourier transformation[J]. Applied Physics Letters, 2008, 92(11): 111102.

[9] T. Godin, L. Sader, A. K. Kashi, P. H. Hanzard, A. Hideur, D. J. Moss, R. Morandotti, G. Genty, J. M. Dudley, A. Pasquazi, M. Kues, and B. Wetzel, Recent advances on time-stretch dispersive Fourier transform and its applications[J]. Advances in Physics: X, 2022, 7(1): 2067487.

[10] A. Mahjoubfar, D. V. Churkin, S. Barland, N. Broderick, S. K. Turitsyn, and B. Jalali, Time stretch and its applications[J]. Nature Photonics, 2017, 11(6): 341-351.

[11] J. Azaña, Time-to-frequency conversion using a single time lens[J]. Optics communications, 2003, 217(1-6): 205-209.

[12] W. C. Banyai, A. A. Godil, M. T. Kauffman, and D. M. Bloom, Time-to-frequency converter for measuring picosecond optical pulses[J]. Appl. Phys. Lett, 1994, 64(3): 270-272.

[13] J. Lancis, and P. Andrés, Lossless equalization of frequency combs[J]. Optics letters, 2008, 33(16): 1822-1824.

[14] D. R. Carlson, D. D. Hickstein, W. Zhang, A. J. Metcalf, F. Quinlan, S. A. Diddams, and S. B. Papp, Ultrafast electro-optic light with subcycle control[J]. Science, 2018, 361(6409): 1358-1363.

[15] B. H. Kolner, Space-time duality and the theory of temporal imaging[J]. IEEE Journal of Quantum Electronics, 1994, 30(8): 1951-1963.

[16] C. V. Bennett, and B. H. Kolner, Upconversion time microscope demonstrating 103× magnification of femtosecond waveforms[J]. Optics letters, 1999, 24(11): 783-785.

[17] E. Arons, E. N. Leith, A. C. Tien, and R. Wagner, High-resolution optical chirped pulse gating[J]. Applied optics, 1997, 36(12): 2603-2608.

[18] V. T. Company, and A. M. Weiner, Optical frequency comb technology for ultra‐broadband radio‐frequency photonics[J]. Laser & Photonics Reviews, 2014, 8(3): 368-393.

[19] M. Fujiwara, M. Teshima, J. Kani, H. Suzuki, N. Takachio, and K. Iwatsuki, Optical carrier supply module using flattened optical multicarrier generation based on sinusoidal amplitude and phase hybrid modulation[J]. Journal of lightwave technology, 2003, 21(11): 2705.

[20] A. Ishizawa, T. Nishikawa, A. Mizutori, H. Takara, H. Nakano, T. Sogawa, A. Takada, and M. Koga, Generation of 120-fs laser pulses at 1-GHz repetition rate derived from continuous wave laser diode[J]. Optics express, 2011, 19(23): 22402-22409.

[21] V. R. Supradeepa, C. M. Long, R. Wu, F. Ferdous, E. Hamidi, D. E. Leaird, and A. M. Weiner, Comb-based radiofrequency photonic filters with rapid tunability and high selectivity[J]. Nature Photonics, 2012, 6(3): 186-194.

[22] A. J. Metcalf, V. T. Company, D. E. Leaird, and A. M. Weiner, High-power broadly tunable electrooptic frequency comb generator[J]. IEEE Journal of Selected Topics in Quantum Electronics, 2013, 19(6): 231-236.

[23] D. C. Cole, K. M. Beha, S. A. Diddams, and S. B. Papp, Octave-spanning supercontinuum generation via microwave frequency multiplication[C]//Journal of Physics: Conference Series. IOP Publishing, 2016, 723(1): 012035.

[24] K. Beha, D. C. Cole, P. Del'Haye, A. Coillet, S. A. Diddams, and S. B. Papp, Electronic synthesis of light[J]. Optica, 2017, 4(4): 406-411.
[25] M. E. Plascak, R. B. Ramirez, K. Bagnell, and P. J. Delfyett, Tunable broadband electro-optic comb generation using an optically filtered optoelectronic oscillator[J]. IEEE Photonics Technology Letters, 2017, 30(4): 335-338.
[26] A. Aubourg, J. Lhermite, S. Hocquet, E. Cormier, and G. Santarelli, Generation of picosecond laser pulses at 1030 nm with gigahertz range continuously tunable repetition rate[J]. Optics Letters, 2015, 40(23): 5610-5613.
[27] A. J. Metcalf, C. D. Fredrick, R. C. Terrien, S. B. Papp, and S. A. Diddams, 30 GHz electro-optic frequency comb spanning 300 THz in the near infrared and visible[J]. Optics Letters, 2019, 44(11): 2673-2676.
[28] A. Ishizawa, T. Nishikawa, K. Hara, K. Hitachi, T. Sogawa, and H. Gotoh, Carrier-envelope-offset locking of 25-GHz EOM comb based on a free-running CW Laser Diode, in Conference on Lasers and Electro-Optics, 2018, paper SM4L.5.
[29] R. Wu, V. R. Supradeepa, C. M. Long, D. E. Leaird, and A. M. Weiner, Generation of very flat optical frequency combs from continuous-wave lasers using cascaded intensity and phase modulators driven by tailored radio frequency waveforms[J]. Optics letters, 2010, 35(19): 3234-3236.
[30] Y. Xing, Q. Wang, L. Huo, and C. Lou, Frequency chirp linearization for ultraflat optical frequency comb generation based on group velocity dispersion[J]. Optics Letters, 2013, 38(13): 2188-2190.
[31] J. V. Howe, J. Hansryd, and C. Xu, Multiwavelength pulse generator using time-lens compression[J]. Optics letters, 2004, 29(13): 1470-1472.
[32] Y. Dou, H. Zhang, and M. Yao, Improvement of flatness of optical frequency comb based on nonlinear effect of intensity modulator[J]. Optics letters, 2011, 36(14): 2749-2751.
[33] V. R. Supradeepa, and A. M. Weiner, Bandwidth scaling and spectral flatness enhancement of optical frequency combs from phase-modulated continuous-wave lasers using cascaded four-wave mixing[J]. Optics letters, 2012, 37(15): 3066-3068.
[34] R. Wu, C. M. Long, D. E. Leaird, and A. M. Weiner, Directly generated Gaussian-shaped optical frequency comb for microwave photonic filtering and picosecond pulse generation[J]. IEEE Photonics Technology Letters, 2012, 24(17): 1484-1486.
[35] R. Wu, D. E. Leaird, and A. M. Weiner, Supercontinuum-based 10-GHz flat-topped optical frequency comb generation[J]. Optics express, 2013, 21(5): 6045-6052.
[36] T. Komukai, T. Yamamoto, and S. Kawanishi, Optical pulse generator using phase modulator and linearly chirped fiber Bragg gratings[J]. IEEE photonics

technology letters, 2005, 17(8): 1746-1748.
[37] T. Yamamoto, T. Komukai, K. Suzuki, and A. Takada, Multicarrier light source with flattened spectrum using phase modulators and dispersion medium[J]. Journal of Lightwave Technology, 2009, 27(19): 4297-4305.
[38] T. Kobayashi, T. Sueta, Y. Cho, and Y. Matsuo, High-repetition-rate optical pulse generator using a Fabry-Perot electro-optic modulator[J]. Applied Physics Letters, 1972, 21(8): 341-343.
[39] M. Kourogi, K. Nakagawa, and M. Ohtsu, Wide-span optical frequency comb generator for accurate optical frequency difference measurement[J]. IEEE Journal of Quantum Electronics, 1993, 29(10): 2693-2701.
[40] R. P. Kovacich, U. Sterr, and H. R. Telle, Short-pulse properties of optical frequency comb generators[J]. Applied optics, 2000, 39(24): 4372-4376.
[41] T. Saitoh, M. Kourogi, and M. Ohtsu, A waveguide-type optical-frequency comb generator[J]. IEEE photonics technology letters, 1995, 7(2): 197-199.
[42] S. Xiao, L. Hollberg, N. R. Newbury, and S. A. Diddams, Toward a low-jitter 10 GHz pulsed source with an optical frequency comb generator[J]. Optics Express, 2008, 16(12): 8498-8508.
[43] I. Demirtzioglou, C. Lacava, K. R. H. Bottrill, D. J. Thomson, G. T. Reed, D. J. Richardson, and P. Petropoulos, Frequency comb generation in a silicon ring resonator modulator[J]. Optics express, 2018, 26(2): 790-796.
[44] S. Xiao, L. Hollberg, and S. A. Diddams, Generation of a 20 GHz train of subpicosecond pulses with a stabilized optical-frequency-comb generator[J]. Optics letters, 2009, 34(1): 85-87.
[45] J. Kim, D. J. Richardson, and R. Slavík, Cavity-induced phase noise suppression in a Fabry–Perot modulator-based optical frequency comb[J]. Optics Letters, 2017, 42(8): 1536-1539.
[46] Y. Hu, M. Yu, B. Buscaino, N. Sinclair, D. Zhu, R. Cheng, A. S. Ansari, L, Shao, M. Zhang, J. M. Kahn, and M. Lončar, High-efficiency and broadband on-chip electro-optic frequency comb generators[J]. Nature Photonics, 2022, 16(10): 679-685.
[47] M. Zhang, B. Buscaino, C. Wang, A. S. Ansari, C. Reimer, R. Zhu, J. M. Kahn, and M. Lončar, Broadband electro-optic frequency comb generation in a lithium niobate microring resonator[J]. Nature, 2019, 568(7752): 373-377.
[48] A. Rueda, F. Sedlmeir, M. Kumari, G. Leuchs, and H. G. L. Schwefel, Resonant electro-optic frequency comb[J]. Nature, 2019, 568(7752): 378-381.
[49] M. Yu, D. III Barton, R. Cheng, C. Reimer, P. Kharel, L. He, L. Shao, D. Zhu, Y. Hu, H. R. Grant, L. Johansson, Y, Okawachi, A. L. Gaeta, M. Zhang, and M. Lončar, Integrated femtosecond pulse generator on thin-film lithium niobate[J]. Nature, 2022: 1-7.
[50] V. S. Ilchenko, A. B. Matsko, A. A. Savchenkov, and L. Maleki, Low-threshold

parametric nonlinear optics with quasi-phase-matched whispering-gallery modes[J]. JOSA B, 2003, 20(6): 1304-1308.

[51] X. Zhang, J. Zhang, K. Yin, Y. Li, X. Zheng, and T. Jiang, Sub-100 fs all-fiber broadband electro-optic optical frequency comb at 1.5 μm[J]. Optics Express, 2020, 28(23): 34761-34771.

[52] A. Ishizawa, T. Nishikawa, T. Goto, K. Hitachi, T. Sogawa, and H. Gotoh, Ultralow-phase-noise millimetre-wave signal generator assisted with an electro-optics-modulator-based optical frequency comb[J]. Scientific Reports, 2016, 6(1): 24621.

[53] N. Kuse, T. R. Schibli, M. E. Fermann, Low noise electro-optic comb generation by fully stabilizing to a mode-locked fiber comb[J]. Optics Express, 2016, 24(15): 16884-16893.

[54] A. Ishizawa, T. Nishikawa, A. Mizutori, H. Takara, A. Takada, T. Sogawa, and M. Koga, Phase-noise characteristics of a 25-GHz-spaced optical frequency comb based on a phase-and intensity-modulated laser[J]. Optics express, 2013, 21(24): 29186-29194.

[55] L. Lundberg, M. Mazur, A. Fülöp, V. T. Company, M. Karlsson, and P. A. Andrekson, Phase correlation between lines of electro-optical frequency combs[C]//CLEO: Applications and Technology. Optica Publishing Group, 2018: JW2A. 149.

[56] I. Morohashi, T. Sakamoto, H. Sotobayashi, T. Kawanishi, and I. Hosako, Broadband wavelength-tunable ultrashort pulse source using a Mach–Zehnder modulator and dispersion-flattened dispersion-decreasing fiber[J]. Optics letters, 2009, 34(15): 2297-2299.

[57] M. A. Prantil, E. Cormier, J. W. Dawson, D. J. Gibson, M. J. Messerly, and C. P. J. Barty, Widely tunable 11 GHz femtosecond fiber laser based on a nonmode-locked source[J]. Optics Letters, 2013, 38(17): 3216-3218.

[58] X. Yan, X. Zou, W. Pan, L. Yan, and J. Azaña, Fully digital programmable optical frequency comb generation and application[J]. Optics letters, 2018, 43(2): 283-286.

[59] G. Wu, L. Liao, S. Xiong, G. Li, Z. Cai, and Z. Zhu, Synthetic wavelength interferometry of an optical frequency comb for absolute distance measurement[J]. Scientific reports, 2018, 8(1): 1-7.

[60] R. Yang, F. Pollinger, K. M. Hagen, J. Tan, and H. Bosse, Heterodyne multi-wavelength absolute interferometry based on a cavity-enhanced electro-optic frequency comb pair[J]. Optics Letters, 2014, 39(20): 5834-5837.

[61] K. Minoshima, and H. Matsumoto, High-accuracy measurement of 240-m distance in an optical tunnel by use of a compact femtosecond laser[J]. Applied Optics, 2000, 39(30): 5512-5517.

Chapter 3. Coherently synthesized two-color EO combs

In this chapter, the simulation of EO comb generation is performed firstly, which is significantly instructive for experiments. Then the principle of coherently synthesized two-color EO combs is introduced. A coherently synthesized 1550/1560 nm two-color EO comb is constructed. The experimentally verification of accumulated phase noise suppression is performed. To further broaden the spectrum, a coherently synthesized 1535/1560 nm two-color EO comb with spectrum span of 60 nm is built. Finally, the coherently synthesized two-color EO comb is integrated in a small mechanical box.

3.1 Single-color EO comb: simulation and construction

3.1.1 Simulation of EO combs

Before constructing EO combs, some simulations about EO comb generation are implemented in order to fully understand the dynamics.

Simulation of EO comb generation:

In chapter 2, equation (2-4) and (2-7) explain the mathematical expression of the optical field after phase modulator and intensity modulator, respectively. The optical field of a seeded CW laser is expressed as $E_{in}(t) = E_0 \times exp(j\omega_c t)$, where E_0 and ω_c are the amplitude and the optical angular frequency of the seed laser, respectively. When this CW laser is modulated by several IMs and PMs in sequence, the output optical field, $E_{out}(t)$, is expressed as：

$$\begin{aligned} &E_{out}(t) = E_{in}(t) \times \prod_{i=1}^{n}[IM_i(t)] \prod_{j=1}^{m}\left[PM_j(t)\right], \\ &IM_i(t) = 1 + exp(j\pi\, V_{IMi}(t)/V_{\pi IMi}) \times exp(j\pi\, V_{DCi}/V_{\pi IMi}), \\ &PM_j(t) = exp\left(j\pi\, V_{PMj}(t)/V_{\pi PMj}\right), \end{aligned} \tag{3-1}$$

where n is the number of IMs, m is the number of PMs. $V_{\pi IM}$, $V_{IM}(t)$ and V_{DC} are the half wave voltage, driven signal and bias voltage of IM, respectively. $V_{\pi PM}$ and $V_{PM}(t)$ are the half wave voltage and driven signal of PM, respectively. According to commutative law of multiplication, the output field remains unchanged when the order of these modulators changes. This means that the orders of these

modulators have no effect to the output field.

The impacts of PMs and IMs on the output field are investigated, respectively. For the sake of simplicity, the DC bias voltage of the IMs and the amplitude of the sinusoidal signal that drives the IM are both set to $V_{\pi IM}/2$. The PMs are also driven by sinusoidal signals. As a result, the generated EO comb should have flat-topped spectrum shape in frequency domain and flat-topped pulses in time domain.

First, let's consider the situation that the CW laser is modualted by one IM and one PM. Two things have to be taken into consideration: the modulation index of PM and the phase match of the RF signals that applied to the modulators. As defined previously, the modulation index of phase modulator is $\pi V_{PM}/V_{\pi PM}$, where V_{PM} is the amplitude of the external RF signal. The modulation index determines the capability to produce as many comb modes as possible. Higher modulation index, more comb modes. The output spectra of the EO combs with 2π, 4π and 7π modulation index are shown in Fig. 3-1 (a). All the spectra are normalized for better comparation. Clearly, the comb mode number increases linearly with the modulation index. Besides, the phases of the sinusoidal signals that drive the modulators should be matched precisely. Otherwise the flatness and the symmetry of the generated spectrum will degrad rapidly. Fig. 3-1 (b) illustrates the output spectra when the phase differences between the driven sinusoidal signals of IM and PM are 0, 0.25π and 0.5π, respectively. In experiment, such phase mismatch could be avoided through appropriately setting the phase of the RF signals that are applied to modulators.

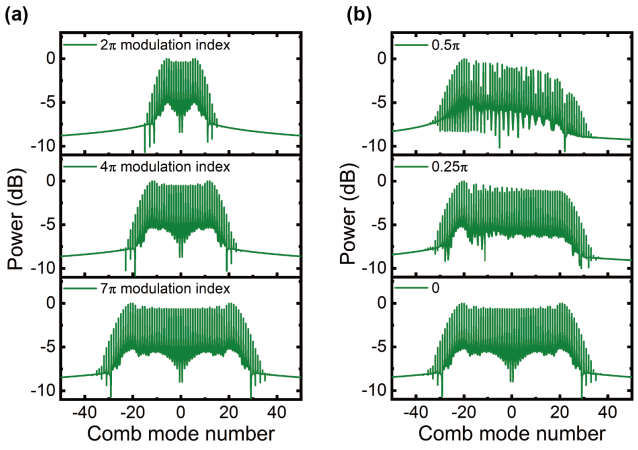

Fig. 3-1 (a): Simulated spectra of EO combs with PM's modulation index of 2π, 4π and 7π. (b): Simulated spectra of EO comb when phase differences between driven signals of IM and PM are set to 0, 0.25π and 0.5π.

Next, EO comb generation with several cascaded PMs is investigated. The

spectra of the EO combs with 1 PM, 2 PMs and 3 PMs are shown in Fig. 3-2 (a). Here, the sinusoidal signals that drive these PMs are in phase. The modulation index of each PM is set to 2π. Therefore, the total modulation index of three PMs is 6π. According to the bottom curve in Fig, 3-2 (a), there are 40 comb modes within 3 dB bandwidth in the EO comb with three PMs, which is nearly three times than the EO comb with only one PM. This indicates that increasing the number of PMs serves the same purpose as increasing the modulation index of a single PM. Note that the prerequisites of in-phase driven signals is very important. The spectra of EO combs with two phase mismatched PMs are shown in Fig, 3-2 (b). The phase differences between the driven signals are set to π, 0.5π and 0, from top to bottom. For the top curve in Fig. 3-2 (b), almost all of the comb modes disappear due to the reversed phase of the driven signals. So, placing a phase shifter in front of each phase modulator is required for precise phase adjusting during experiment.

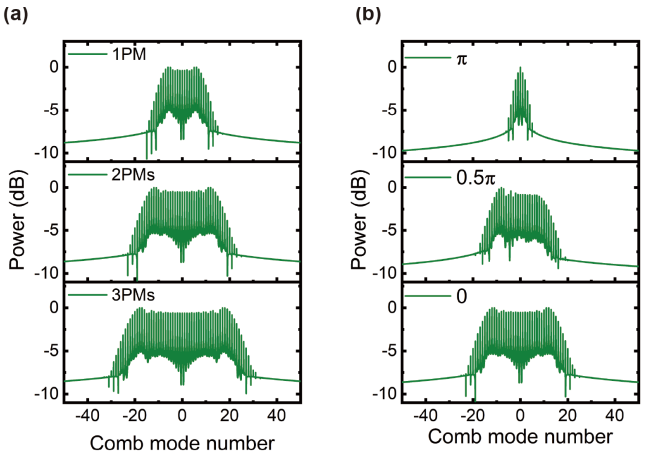

Fig. 3-2 (a) Simulated spectra of EO comb with 1 PM, 2 PMs and 3 PMs. (b): Simulated spectra of EO comb with 2 PMs. The phase difference of the driven signals to the two PMs are set to π, 0.5π and 0.

According to the simulation, the relationship between the comb mode number and the modulation index of PM is plotted in Fig. 3-3. Here, the number of comb modes within 3 dB bandwidth is denoted as the comb mode number. The correlation factor R^2 is 0.99997. The right axis shows the corresponding spectrum bandwidth when assuming 10-GHz comb spacing and 1550-nm center wavelength. Some experimental results according to the references [1]-[7] are plotted in Fig. 3-3 as the orange dots, which shows well agreement with the simulation.

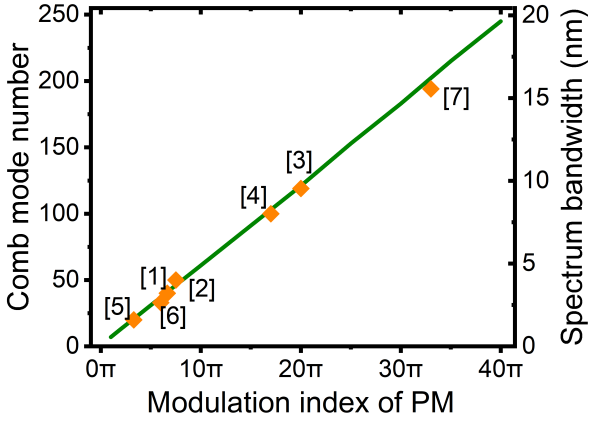

Fig. 3-3 Left axis: simulated comb mode number versus the modulation index of PM. Right axis: corresponding spectrum bandwidth when assuming 10-GHz comb spacing and 1550-nm center wavelength. Orange dots: experimental results in references [1]-[7].

The impact of the number of IMs on the EO comb is also investigated in the simulation. Fig. 3-4 shows the spectrum and pulse shape of the EO combs with one and two IMs. The modulation index of PM is 7π. The comb mode spacing is set to 10 GHz, corresponding to 100-ps repetition period of pulses. All these curves are normalized. Both of the two pulses have flat-topped shape. According to time-to-frequency mapping, the spectrum shaped of the EO comb should be the duplication of the pulse shape if quadratic phase is imposed on the flat-topped pulse. In the case of sinusoidal phase modulation, the temporal phase gradually deviates from quadratic phase at pulse's edges, which introduces high order chirp to the pulse. Therefore, the spectrum shape deviates from ideal case, leading to the "bat ears" at spectrum edges. From Fig. 3-4 (b), the pulses have duty cycles of 60% and 50% from EO combs with one IM and two IMs, respectively. When two IMs are applied, the pulse is narrower. Therefore, the high order chirp at pulse's edges that induced by imperfect quadratic phase modulation is weaker. Hence the spectrum flatness is improved and the bat ears are reduced.

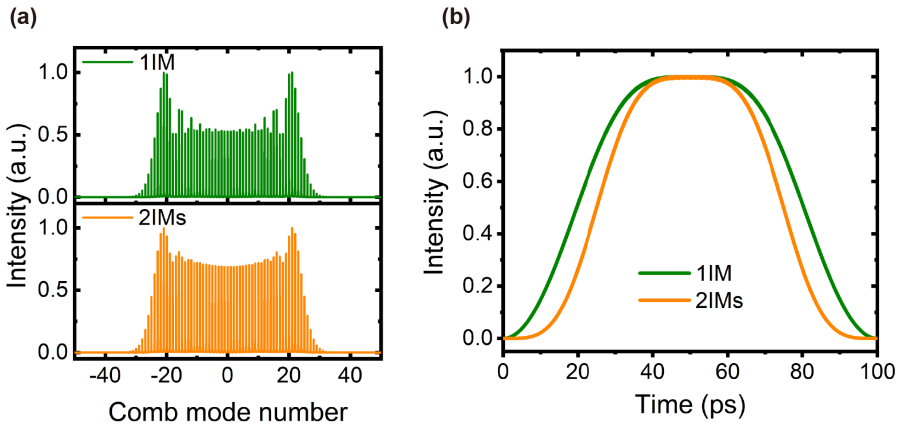

Fig. 3-4 Simulated spectra (a) and simulated pulse in time domain (b) of EO combs generated with one (green curve) and two (orange curve) IMs.

Simulation of pulse compression of EO comb:

The pulse emitted from an EO comb is nearly linear chirped. So it can be compressed easily through a piece of single-mode fiber, a chirped fiber Bragg grating, or a pulse shaper. Among these devices, using single-mode fiber for pulse compressing is the simplest with the lowest cost. Suppose two IMs and three PMs are used to generate a flat-topped EO comb. The total modulation index of three PMs is 7π. The comb spacing is set to 10 GHz. The optical spectrum the EO comb is same as orange curve in Fig. 3-4 (a). In time domain, the pulse envelope, instantaneous frequency and its phase are shown in Fig. 3-5. According to the decreasing instantaneous frequency, the pulse has positive chirp, which can be compensated by negative dispersion fiber like SMF28.

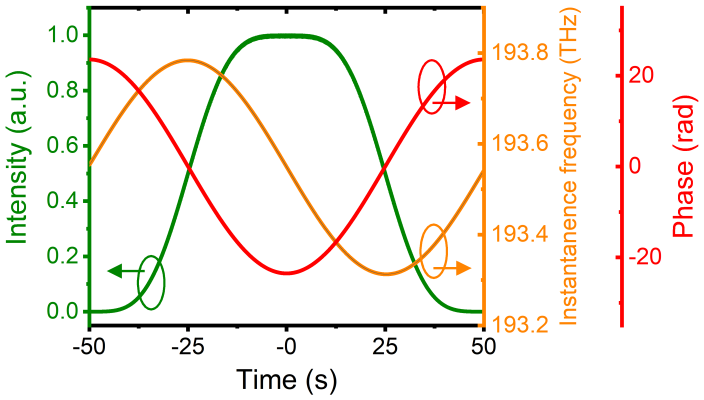

Fig. 3-5 Green curve: envelope of the EO pulse. Orange curve: instantaneous frequency of the EO pulse. Red curve: phase of the EO pulse.

The simulated pulse evolution in a piece of 574-m SMF28 is displayed in Fig.

3-6 (a). The simulation is based on nonlinear Schrödinger equation and split-step Fourier method [8]. The length of the SMF28 is chosen to obtain narrowest pulse. The pulse traces at the input and output of the SMF28 are plotted in Fig. 3-6 (b), as the green curve and orange curve. The pulse is compressed to 1.8 ps through the SMF, which is nearly Fourier transform limited duration. Around the main pulse, there are symmetrical pedestals, attributing to high order chirp. These pedestals are unavoidable if sinusoidal signals are used to drive PMs. In fact, the pedestals around the main pulse and the bat ears in the spectrum are manifestations of the same phenomenon in the time and frequency domains. The optical spectra at the input and output of the SMF is also shown in Fig. 3-6 (b).

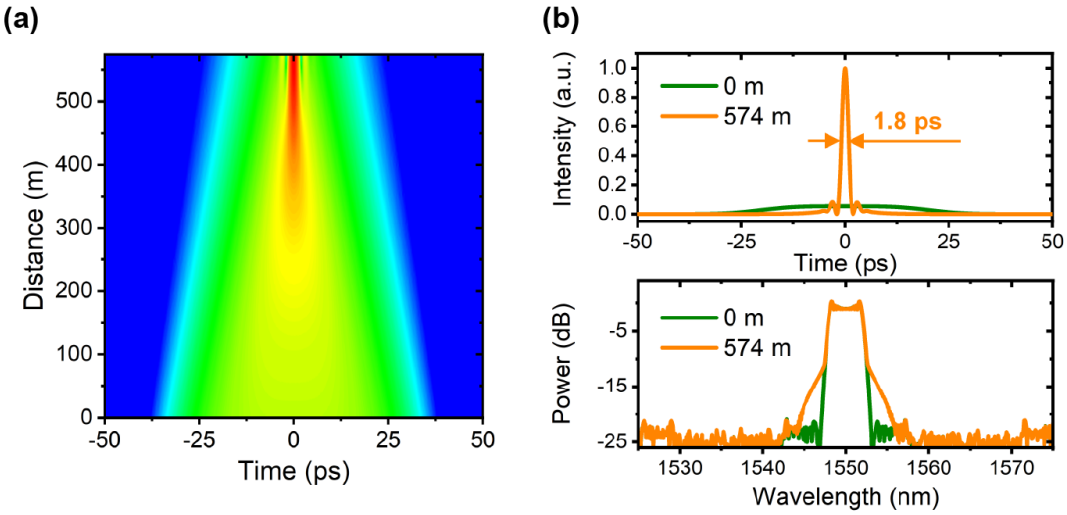

Fig. 3-6 (a): Evolution of pulse from EO comb in 574-m SMF. (b): Top: the pulse trace at the input (green) and output (orange) of the 574-m SMF. Bottom: optical spectra at the input (green) and output (orange) of the 574-m SMF.

During the simulation, it is found that the length of the SMF required for pulse compression varies with the modulation index. With the increases of modulation index, the chirp rate of the pulse decreases since frequency components are more aggregated in the pulse. Therefore, shorter SMF is required to compress the pulse. The relationship between the required length of SMF and the modulation index of PM is displayed in Fig. 3-7. From the simulation, the required length decreases with increasing modulation depth. The amount of dispersion that needed for pulse compression can be obtained by multiplying the required fiber length with its dispersion. Meanwhile, the compressed pulse becomes narrower when the modulation depth increases, which is benefiting from broader spectrum. The pulse width after compression has the same tendency as the required length of SMF, as the orange

curve shows in Fig. 3-7.

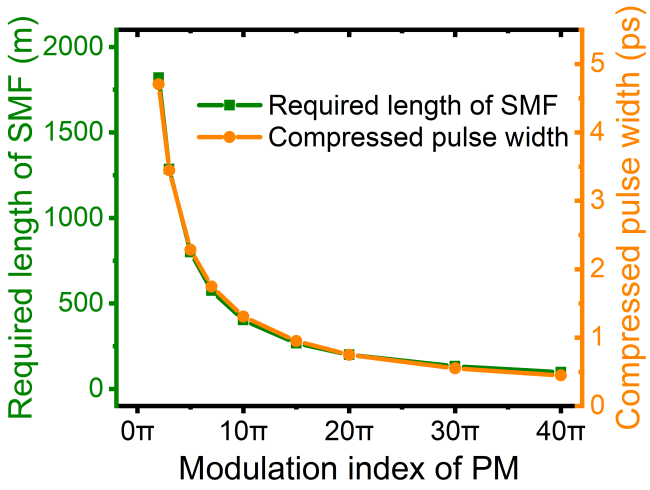

Fig. 3-7 Green curve: Required length of SMF for pulse compression with respect to modulation index of PM. Orange curve: Compressed pulse width with respect to modulation index of PM.

In the above simulation, the average optical power of EO comb is low (less than several tens of mW). However, when the average power is at hundreds of mW or W level, the spectrum of the EO comb would broaden in the long SMF because of nonlinearity. The nonlinearity accelerates the pulse compression in SMF. Therefore, the length of SMF that required for pulse compression become shorter. For example, only 508 m SMF is needed to compress the pulse when the average power is 1 W, where the input pulse is same as that in Fig. 3-6. The pulse evolution in the 508 m fiber is displayed in Fig. 3-8 (a). The pulse and optical spectrum at the input and output of the 508 m fiber is plotted in Fig. 3-8 (b). The spectrum broaden is apparently. The pulse width is 0.76 ps after compression, which is narrower due to broader spectrum.

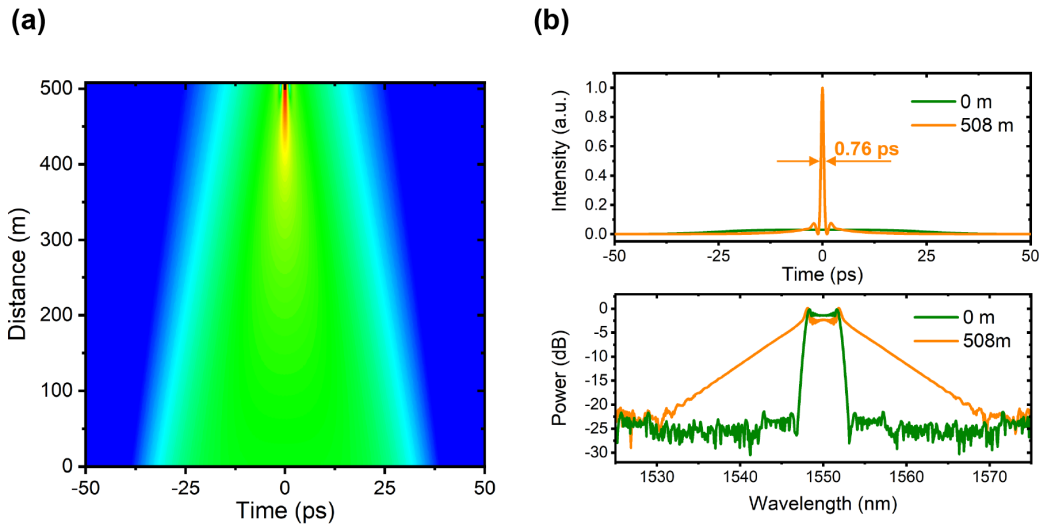

Fig. 3-8 (a): Evolution of EO pulse in 508-m SMF when the average power is 1 W. (b): Top: The pulse trace at the input (green) and output (orange) of the 508-m SMF. Bottom: optical spectra at the input (green) and output (orange) of the 508-m SMF.

On the basic of above simulation, the obtaining of an EO comb with Fourier limited pulse becomes very clear and simple. The modulation index could be calculated through the total amplitude of applied RF signal and the half wave voltage of PMs. The half wave voltage is given by the manufacturer. The spectrum bandwidth, Fourier transform limited pulse duration and required amount of dispersion for pulse compression in ideal case can be estimated according to Fig. 3-3 and Fig. 3-7, respectively. The phase match among the RF signals is simple to achieve by monitoring the optical spectrum when tuning the phase shifter. During the experiment, the phase shifters in front of the PMs should be adjusted until the optical spectrum is broadest. Then the phase shifters in front of the IMs should be tuned until the optical spectrum is symmetric. Next a piece of long fiber could be used to compress the pulse. The pulse width is monitored by measuring the autocorrelation trace of the pulse. The phase match among the RF signals is guaranteed if the pulse is successfully compressed. If pulse is not compressed, the phase shifters in front of the IMs should tuned another π to realize phase match.

3.1.2 Construction of single-color EO comb

An EO comb with 1540-nm center wavelength is constructed as an example. EO combs with other center wavelengths in C-band can be easily obtained by replacing the CW laser.

The configuration of the EO comb is given in Fig. 3-9 (a). The center wavelength of the CW laser (RIO, PLANEX) is 1540 nm. The output power of the CW laser is 19 mW. Two EO IMs (iXblue, MXAN-LN-10-PD-P-P-FA-FA-LIL) and three EO PMs (iXblue, MPZ-LN-10-00-P-P-FA-FA-HEP) are utilized to modulate the CW laser. These IMs and PMs are both driven by sinusoidal signals with 10-GHz frequency. These sinusoidal signals are from an RF synthesizer (KEYSIGHT E8257D), which is referenced to a 10 MHz GPS-disciplined clock. The amplitudes of these sinusoidal signals are different. The amplitudes of the driven signals that applied to the two IMs are equal to their $V_{\pi IM}/2$, while the DC bias voltages are also $V_{\pi IM}/2$. The RF power to each PM is 33 dBm. Considering the 6-V half-wave voltage of each PM, the total modulation index to the PMs is 7π. Five phase shifters that placed before the five modulators ensure the phase match between the driven signals. Therefore, an EO comb with 10 GHz repetition rate is obtained, as shown in Fig. 3-9 (b). There are 43 comb modes in the generated EO comb. The simulated optical spectrum using same parameters is plotted as the orange curve in Fig. 3-9 (b), which is in good agreement with experiment result. The optical power of the EO comb is 0.4 mW. A home-made EDFA is used for power amplification. The optical power at the output of the EDFA is 30 mW. A piece of 580-m SMF is used for pulse compression. The autocorrelation trace of the pulse is shown in Fig. 3-9 (c), which is close to Fourier-transform-limited duration. Still, the length of SMF and the pulse width show high consistency with simulation.

In the following, the EO combs generated from one CW laser are called as single-color EO comb, in order to distinguish them from EO combs generated from more than one CW laser.

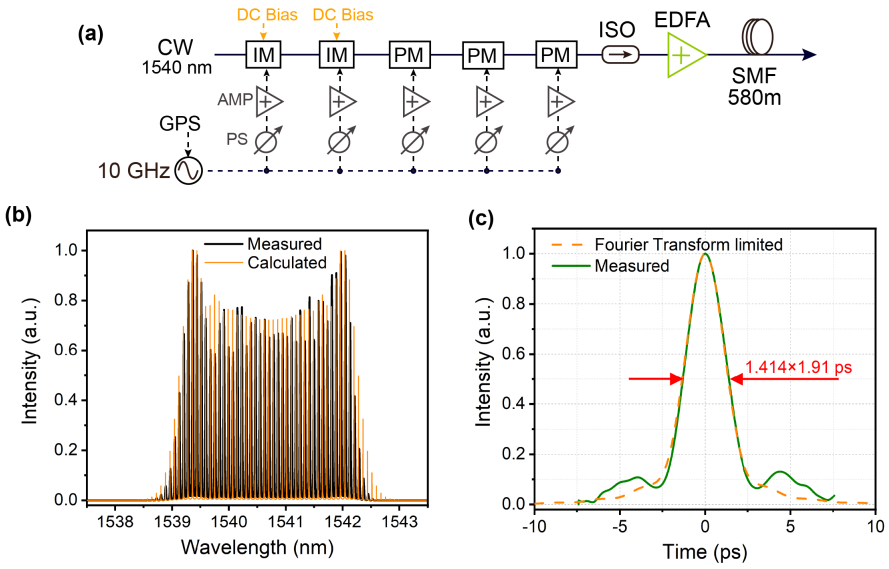

Fig. 3-9 (a) Experimental setup of single-color EO comb; CW: continuous-wave laser; AMP: amplifier; PS: phase shifter; IM: EO intensity modulator; PM: EO phase modulator; ISO: isolator; EDFA: Erbium-doped fiber amplifier; SMF: single-mode fiber. (b) Optical spectrum of EO comb. Black: measured data by optical spectrum analyzer (resolution: 0.02 nm); Orange: optical spectrum from simulation. (c) Autocorrelation trace of the compressed pulse. Solid green: measured trace; Dashed orange: Fourier transform limited trace calculated from measured optical spectrum in Fig, 3-9 (b).

3.2 Principle of coherently synthesized two-color EO comb

3.2.1 Limitations of EO combs

1. Narrow spectrum bandwidth

In an EO comb, the EO intensity modulators governs the pulse shape in time domain, while the equally spaced comb modes are generated by modulating the CW lasers with phase modulators [1]-[14]. The number of the comb modes is determined by the total modulation index of the EO phase modulators, i.e., $\pi V_{PM}/V_{\pi PM}$, where V_{PM} is the total peak voltage of the signal that drives EO phase modulators and $V_{\pi PM}$ is half-wave voltage of EO phase modulator. Therefore, the spectral bandwidth of an EO comb is determined by the number of comb modes multiplied with comb mode spacing (i.e., repetition rate). In other words, the higher modulation index, the broader spectrum. However, taking a commercial EO phase modulator with 10 GHz modulation frequency as an example, the lowest half wave voltage that manufacturers can achieve for now is around 3 V, while the maximum RF input power is around 36 dBm (corresponding to 20-V peak voltage). Therefore, the spectral bandwidth of an

EO comb is usually narrow. For instance, the typical spectrum bandwidth for a 10-GHz-repetition-rate EO comb is 3-5 nm. Although it is possible to extend the spectrum bandwidth by increasing the number of phase modulators[7], high cost and high insertion loss of these phase modulators is problematic. So far, the main method for spectrum broadening of EO combs is making use of highly nonlinear devices [1][2][13], such as highly nonlinear fiber, photonic crystal fiber, waveguide, etc.

2．Accumulated phase noise from RF oscillator

Since all the comb modes of an EO comb is generated by modulating a CW laser with EO phase modulators, the phase noise of the RF oscillator that drives the phase modulators will diffuse to the comb modes as well. Here the phase noise of comb modes that induced by RF oscillator is named as accumulated phase noise. The higher comb mode number, the higher accumulated phase noise in comb modes, as explained by equation (2-9). The slope of the accumulated phase noise with respect to comb mode number indicates the phase noise performance of the RF oscillator [4]. According to Fig. 2-8 (b), accumulated phase noise dominates the phase noise of comb modes at high Fourier frequency (> 1 kHz). Thus, it is hard to suppress the accumulated phase noise using phase-locked loop because of limited locking bandwidth. Therefore researchers often apply passive ways to suppress the accumulated phase noise. The most straightforward method is to drive the phase modulators using an RF oscillator with ultralow phase noise. A. Ishizawa *et al.* demonstrated that RF oscillators with different phase noise result in different accumulation slope [4]. In Ref. [13], the authors found that the SNR of the carrier-envelope offset frequency increases when utilizing RF oscillator with lower phase noise. The SNR of carrier-envelope offset frequency are 20 dB, 25 dB and 35 dB when using a synthesizer, a dielectric-resonator oscillator and a sapphire-cavity oscillator to drive the phase modulators, respectively. In addition, either a Fabry-Perot cavity after EO comb generation or a built-in Fabry-Perot cavity is a powerful tool to reduce the accumulate phase noise by taking advantage of the cavity's Lorentzian transmission [1][13][15]. In fact, a Fabry-Perot cavity is essential to detect carrier-envelope offset frequency of an EO comb. However, besides the high cost and high insertion loss of the Fabry-Perot cavity, the wide tuning range of EO combs' repetition rate is no longer allowed.

Therefore, it's urgent to come up with an uncomplicated method for EO comb spectrum broadening and suppression of accumulated phase noise. In this thesis, a

broad spectrum EO comb is generated by coherent synthesizing two EO combs to 'one' comb. Meanwhile, the accumulated phase noise of comb modes is suppressed by effectively reducing the mode numbers in the generated broadband comb. This method is simple since only one slow phase-locked loop is needed to coherently synthesize the two EO combs.

3.2.2 The principle of coherently synthesized two-color EO combs

In coherently synthesized two-color EO comb, two CW lasers with distinct wavelengths are combined and modulated by common EO modulators. The wavelengths of the two CW lasers should be within the operating bandwidth of all EO modulators. As a result, two EO combs with same spectrum shape and spectrum bandwidth but distinct center wavelengths are generated. Attributing to the relative drifting between the two CW lasers, the two EO combs are independent. So it's necessary to coherently synthesize the two EO combs in order to make them 'one' comb. Here the beat note between the two EO combs is detected and phase-locked to a low noise RF reference through current feedback to one of the CW lasers. The concept of coherently synthesized two-color EO comb is illustrated in Fig. 3-10.

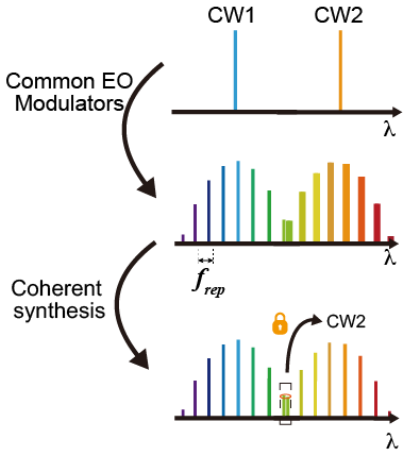

Fig. 3-10 Concept of coherently synthesized two-color EO comb. CW: continuous-wave laser.

The principle of spectrum broadening and accumulated phase noise suppression of coherently synthesized two-color EO combs is explained in two steps. First, why the coherent synthesis make two combs to one comb is explained. Then, spectrum bandwidth extension and suppression of accumulated phase noise of the coherently synthesized two-color EO comb are illustrated.

(i) Coherent synthesis of two EO combs to make them 'one' comb

In a typical single-color EO comb, the changes in repetition rate (e.g. becomes larger) lead to the changes of the optical frequencies of the comb modes in a synchronized motion as illustrated in Fig. 3-11 (a). The optical frequency of the 0^{th} comb doesn't change since it is only determined by the optical frequency of the CW laser. When there is Δf_{rep} in repetition rate, the optical frequencies of $\pm n^{\mathrm{th}}$ comb mode vary $\pm n \times \Delta f_{rep}$, as the red arrows shown in Fig. 3-11 (a), where n is the comb mode number. Therefore, it's reasonable to consider the optical frequency of 0^{th} comb mode as 'origin of coordinate'. In one OFC, there must be one and only one 'origin of coordinate'.

In two independent EO combs, the frequencies of comb modes in two EO combs changes in an independent motion, as shown in Fig. 3-11 (b). The optical frequency of the two 0^{th} comb modes don't change, while that of other comb modes vary with respect to their comb mode number. Since the optical frequencies of the two 0^{th} comb modes are independent, there are two 'origins of coordinate'. So the two independent EO combs cannot be considered as one frequency comb.

To make the two independent EO combs 'one' comb, the two EO combs should be coherently synthesized by phase locking their beat note, resulting in a coherently synthesized two-color EO comb. In this way, the optical frequency of the second 0^{th} comb mode changes when the repetition rate change. The optical frequencies of other comb modes change in a synchronized motion, as shown in Fig. 3-11 (c), which is same as that in a single-color EO comb. Consequently, the coherently synthesized two-color EO comb can be considered as one frequency comb since there is only one 'origin of coordinate'.

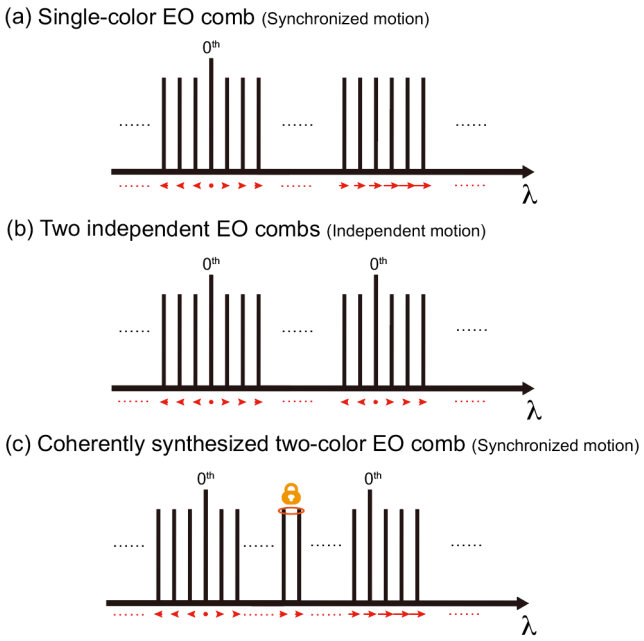

Fig. 3-11 The motion of comb modes' optical frequency in single-color EO comb (a), two independent EO combs (b) and coherently synthesized two-color EO comb (c).

(ii) Broadening the spectrum and obtainment of a low-noise EO comb by combining the low-noise comb modes

The benefit obtained from the coherently synthesized two-color EO comb is that the spectrum bandwidth is extended and the low-noise comb modes in the two EO combs are combined. In a coherently synthesized two-color EO comb, the number of comb modes is nearly twice than that in a single-color EO comb under the same experimental conditions. Therefore, the spectrum bandwidth of the coherently synthesized two-color EO comb is twice broader.

According to the analysis in Section 2.1.3, the accumulated phase noise of the comb modes in a single-color EO comb increases with respect to the comb mode number, as represented by the V-shaped red curve in Fig. 3-12 (a). However, in the coherently synthesized two-color EO comb, the comb mode number is calculated according to the comb mode's frequency away from the center frequencies. Since there are two center frequencies, the comb modes located near the second center frequency have much smaller comb mode number compared to those comb modes with same frequencies in a single-color EO comb. For instance, the 3rd comb mode in the coherently synthesized two-color EO comb has the same frequency as the nth comb mode in a single-color EO comb, as shown in Fig. 3-12. Here, n>>3. Therefore, all the comb modes that locate near the second center frequency have lower intrinsic

phase noise because of lower comb mode number. The accumulated phase noise of a coherently synthesized two-color EO comb is represented by the W-shaped red curve in Fig. 3-12 (b). Compared to that in a single-color EO comb, the phase noise accumulation from RF synthesizer is suppressed effectively by combining the low-noise comb modes in the coherently synthesized two-color EO comb.

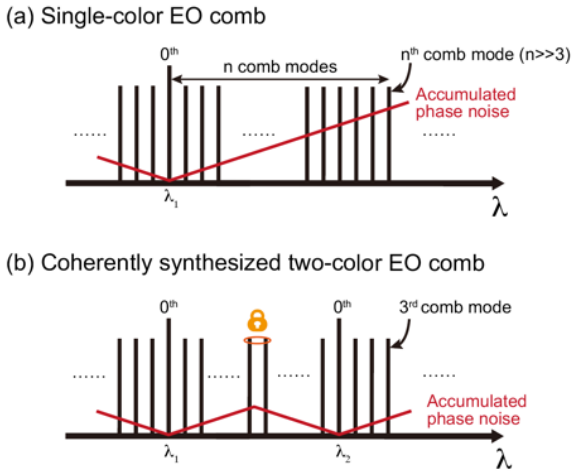

Fig. 3-12 Accumulated phase noise in single-color EO comb and coherently synthesized two-color EO comb. The center wavelength of the single-color EO comb is λ_1. The center wavelengths of the two-color EO comb are λ_1 and λ_2.

Moreover, if two EO combs with larger center wavelength separation are coherently synthesized, the phase noise of comb modes at the spectrum edge could be further suppressed, as explained in Fig. 3-13.

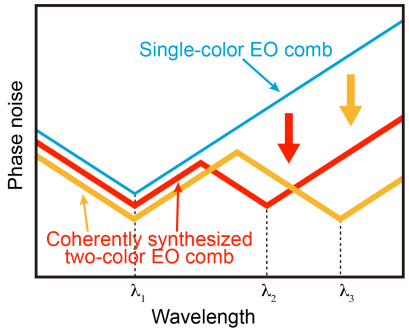

Fig. 3-13 Accumulated phase noise in single-color EO comb and coherently synthesized two-color EO comb.

3.2.3 Coherently synthesized multi-color EO combs

The concept of coherently synthesized two-color EO comb could be extended to coherently synthesized multi-color EO combs. As illustrated in Fig. 3-14, through

modulating three or more CW lasers with common EO modulators and synthesizing these EO combs, coherently synthesized multi-color EO comb could be generated. The wavelengths of these CW lasers must be within the operating wavelength range of all the EO modulators. In this case, further spectrum broadening is realized. Multi-color EO comb with >100 nm spectrum bandwidth is achievable through this method. However, more phase-locked loops are required to realize the coherent synthesis of multi EO combs, which will make the system complicate and costly. One need to be careful to meet the trade-off.

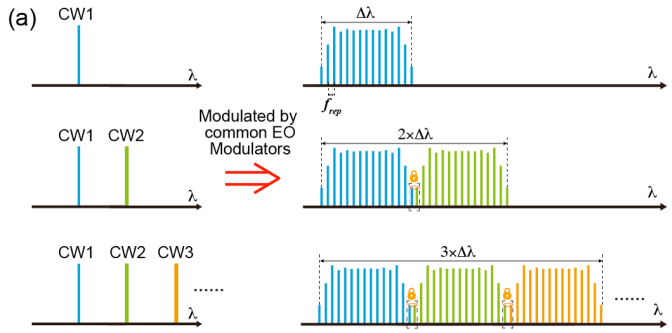

Fig. 3-14 Coherently synthesized multi-color EO comb

3.3 Coherently synthesized 1550/1560 nm two-color EO comb

3.3.1 Experimental setup and results

The experimental setup of the coherently synthesized two-color EO comb is shown in Fig. 3-15 (a). Two CW lasers (labeled as CW1 and CW2, RIO PLANEX, 5 kHz linewidth) centered at 1550 nm and 1560 nm are combined and modulated by two intensity modulators (iXblue, MXAN-LN-10-PD-P-P-FA-FA-LIL) and three phase modulators (iXblue, MPZ-LN-10-00-P-P-FA-FA-HEP). The output power of CW1 and CW2 is 19 mW and 20 mW, respectively. The detailed configuration of the EO comb is plotted in Fig. 3-15 (b). CW1 and CW2 are combined by a 3-dB optical coupler. The driven signals to the modulators are 10 GHz sinusoidal signals from a synthesizer (KEYSIGHT, E8257D). This synthesizer is referenced to a 10-MHz GPS-disciplined clock. To get enough power for each IM and PM, the output of the synthesizer is split into five path and amplified separately. Five phase shifters are inserted before the five RF amplifiers in order to guarantee the phase match between the driven signals. The RF power that applied to each IM corresponds to an amplitude of $V_{\pi IM}/2$, while the DC bias voltage of each IM is also $V_{\pi IM}/2$. Therefore, the EO

comb emits flat-topped pulses in time domain. The RF power applied to each PM is 33 dBm. Considering that the half-wave voltage of the PMs is around 6 V at 10 GHz, the total maximum modulation index to the PMs is about 7π. As a result, two EO combs with 10 GHz repetition rate are generated. There are 43 comb modes in each comb. The total output power of the two EO combs is 0.39 mW. An isolator is installed after the EO comb generation. So far, all the fiber pigtails are polarization-maintaining fiber. The optical spectrum of the two EO combs is shown in Fig. 3-15 (c). The 10-dB spectrum bandwidth of each EO comb is 3 nm, which is less than the wavelength separation between the two CW lasers. Therefore, there is no spectrum overlap between the two EO combs. In order to achieve the coherent synthesis of the two EO combs, power amplification, pulse compression and spectrum broadening are required.

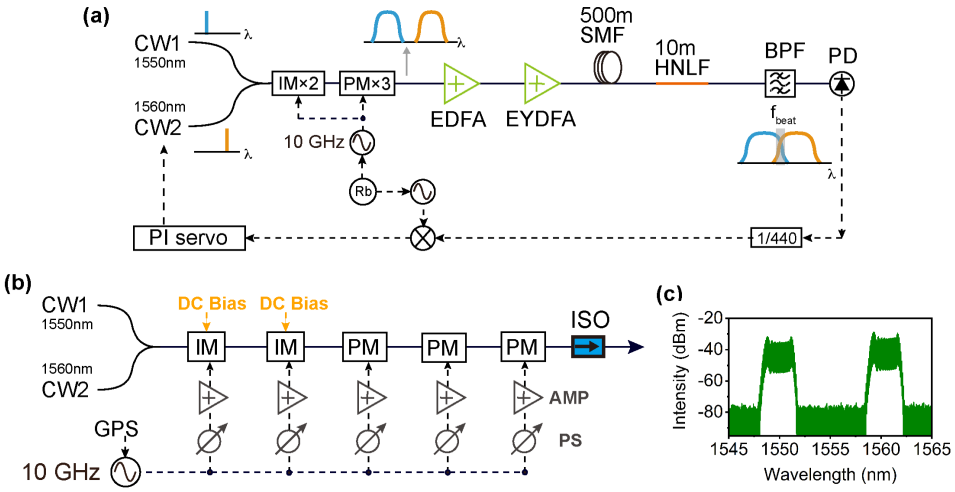

Fig. 3-15 (a): Experimental setup of coherently synthesized 1550/1560 nm two-color EO comb. IM: intensity modulator. PM: phase modulator. EDFA: Erbium-doped fiber amplifier. EYDFA: Erbium-Ytterbium co-doped fiber amplifier. SMF: single-mode fiber. HNLF: highly nonlinear fiber. BPF: bandpass filter. PD: photodetector. (b): Detailed configuration of the EO comb. ISO: isolator. (c): Optical spectrum of two EO combs.

The optical power is firstly amplified to 100 mW by a home-made Erbium-doped fiber amplifier (EDFA). The configuration of the EDFA is shown in Fig. 3-16 (a). All the fibers in EDFA are single-mode fiber. Since the seed power is weak, a piece of long EDF with low core absorption (single-mode EDF 30-4/125, Liekki, 3.3 m) is used to realize the power amplification gradually. The gain fiber is bi-directionally pumped by two single-mode pump laser diodes centered at 976 nm. The output power of EDFA with respect to pump current is shown in Fig. 3-16 (b). The green curve

indicates that only backward pump is turned on, while the red curve indicates that both backward and forward pump are turned on. The optical spectrum at the output of EDFA is given in Fig. 3-16 (d). The spectrum shape is almost same as that in Fig. 3-15 (c) besides the weak amplified spontaneous emission (ASE).

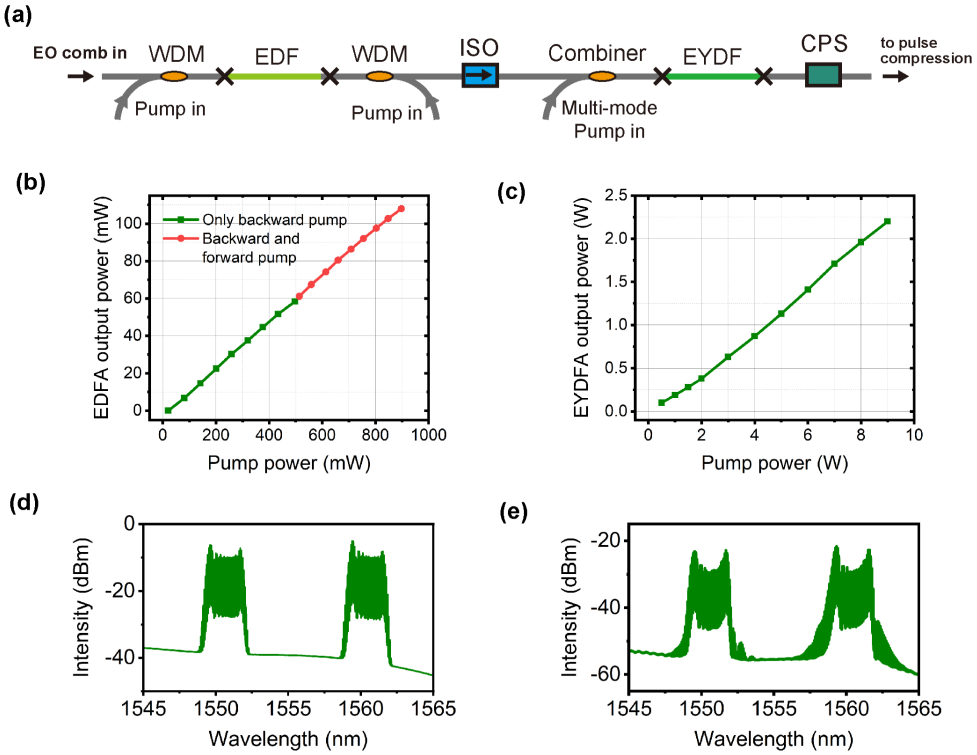

Fig. 3-16 (a): Experimental configuration of EDFA and EYDFA. WDM: wavelength division multiplexer. EDF: Erbium-doped fiber. ISO: isolator. Combiner: pump/signal combiner. EYDF: Erbium-Ytterbium co-doped fiber. CPS: cladding power stripper. (b): Output power of EDFA versus pump power. Green curve: the EDF is only pumped through backward direction. Red curve: the EDF is pumped bi-directionally. (c): Output power of EYDFA with respect to the pump power. (d): Optical spectrum of the two-color EO comb after EDFA. (e): Optical spectrum of the two-color EO comb after EYDFA and 500-m SMF.

Then, a home-made double clad Erbium-Ytterbium co-doped fiber amplifier (EYDFA) is utilized to further amplify the optical power. The structure of EYDFA is plotted in Fig. 3-16 (a). An isolator is inserted between EDFA and EYDFA, in order to protect the EDFA from back scattering. All the fibers in EYDFA are also single-mode fiber. The 2.8-meter-long EYDF (Coractive, DCF-EY-10/128) is pumped by a multi-mode laser diode operating at 976 nm. A combiner is used to coupling the pump laser into the EYDF. The remaining pump light is removed through a cladding power stripper (CPS). The output power versus the pump power is plotted in Fig. 3-16 (c).

The slope efficiency is 24.4%. It is found that seed saturates the input of the EYDFA. Actually, 70 mW input power is enough for the EYDFA. As a result, 30 percent output of the EDFA could be coupled out for other applications, such as distance measurement. The output of the EYDFA is directed into a piece of 500-m single mode fiber (SMF) for pulse compression. The pulse width is compressed to 1 ps, which is nearly Fourier transform-limited pulse duration. The length of the SMF is chosen according to simulation. The optical spectrum of the two-color EO comb after EYDFA and 500-m SMF is shown in Fig. 3-16 (e), indicating that the spectra of the two EO combs are both slightly broadened.

The compressed pulses then go into a piece of 10-m highly nonlinear fiber (HNLF) to broaden the spectrum. The dispersion and dispersion slope of the HNLF are -0.9 ps/nm/km and 0.025 ps/nm^2/km, respectively. The nonlinear coefficient is 23 W^{-1}·km^{-1}. At the output of the HNLF, the two EO combs are spectrum broadened, as shown in Fig. 3-17 (a). Part of the spectra of the two EO combs are overlapped. In this case, the pump power of the EYDFA is set to 5 W, resulting in 1.13 W output power. At higher pump power level, the pulses from the two EO combs will split, which is harmful for the spectrum broadening.

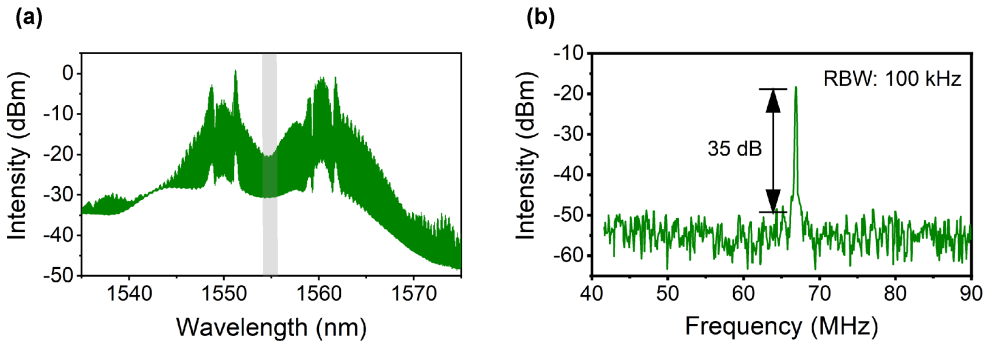

Fig. 3-17 (a): Optical spectrum of the two-color EO comb after spectrum broadening. (b): RF spectrum of the beat note between the two-color EO comb. The SNR of the beat note is 35 dB.

Then the overlapped comb modes is filtered out via a narrow bandpass filter with 1 nm full-width-at-half-maximum bandwidth. The pass band of the bandpass filter is displayed as the gray shaded area in Fig. 3-17 (a). The beat note between these comb modes (labeled as f_{beat}) is detected through a low-noise photo detector (New focus 1811). The RF spectrum of f_{beat} is shown in Fig. 3-17 (b). The signal-to-noise ratio (SNR) of f_{beat} is 35 dB at 100 kHz resolution bandwidth. Then f_{beat} is phase locked to a radio frequency reference through current feedback to CW2 after frequency dividing

by a factor of 440. After phase locking, the frequency fluctuation of f_{beat} is recorded within 20 min, as plotted in Fig. 3-18 (a). The standard deviation is 0.097 Hz. According to the Allan deviation of f_{beat} in Fig. 3-18 (b), the stability of f_{beat} is at 10^{-16} level in 1 s averaging time. The stability of f_{beat} gradually increases with longer averaging time. The phase noise power spectrum density (PSD) of f_{beat} before and after phase locking is measured through a phase noise analyzer [16], as shown in Fig. 3-18 (c). Within the 3-kHz locking bandwidth, the phase noise is reduced very well. Therefore, the two EO combs are coherently linked, resulting in a coherently synthesized two-color EO comb. Unfortunately, it is not able to phase lock f_{beat} without using the frequency divider. This is because of the large amount of accumulated phase noise.

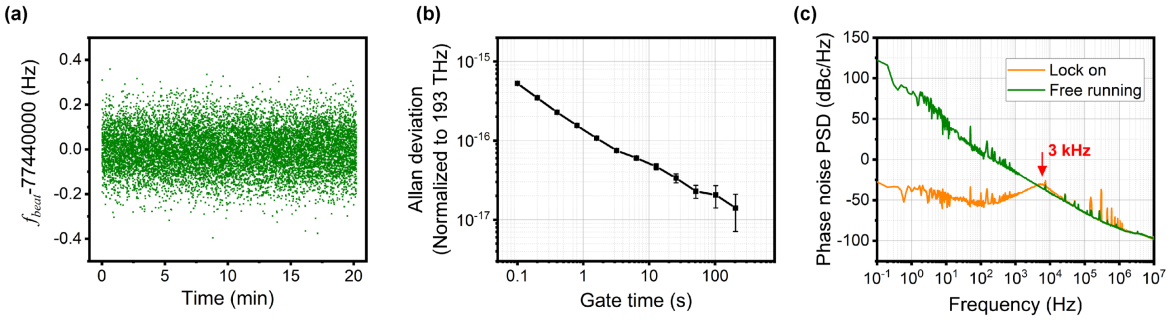

Fig. 3-18 (a) Frequency fluctuation of f_{beat}. (b): Allan deviation of f_{beat}. (c): Phase noise PSD of f_{beat} before and after phase locking.

It's worth to note that the two EO combs have a frequency offset in this case since f_{beat} is not zero. There are several possible methods to realize offset-free coherent synthesis between the two EO combs. For example, one can frequency shift one of the EO combs through an acousto-optic frequency shifter (AOFS). Then phase lock the beat note between the two EO combs to the driving frequency of the AOFS. Offset-free phase locking between the two EO combs is achieved at the laser output before the AOFS. This method is commonly utilized to realize zero carrier-envelope offset frequency phase locking in an optical frequency comb [17][18]. Another alternative is to beat the two EO combs with a third CW laser respectively, resulting in two beat notes that labeled as f_{beat1} and f_{beat2}, as shown in Fig. 3-19. By phase locking f_{beat1} and f_{beat2} to the same frequency, offset-free phase-locking of the two-color EO comb could be realized. However, this scheme is not demonstrated in this thesis because the small offset in the two-color EO comb has no effect to its application in absolute distance measurement.

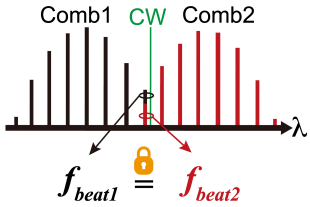

Fig. 3-19 A scheme of offset-free coherently synthesized two-color EO comb.

3.3.2 Suppression of accumulated phase noise

In order to experimentally verify the suppression of accumulated phase noise in coherently synthesized two-color EO comb, the phase noise PSDs of some comb modes are measured. The experimental setup is shown in Fig. 3-20 (a). At the output of HNLF, 50% power of the two-color EO comb is extracted and beat with a wavelength tunable CW laser (TOPTICA CTL1550), whose phase noise PSD is shown in Fig. 3-20 (b). The beat note between the tunable CW laser and the nearest comb mode in two-color EO comb (labeled as f_{beat2}) is detected by a low-noise photodetector (PD2, New focus 1414). The phase noise PSD of f_{beat2} is measured by a phase noise analyzer. The phase noise of this comb mode is evaluated according to the phase noise of f_{beat2}. By adjusting the wavelength of the tunable CW laser and beating it with different comb modes, a series of phase noise PSDs are obtained. As a result, the phase noise of all the comb modes can be investigated.

The process of comb mode phase noise evaluation is illustrated in Fig. 3-20 (c). The phase noise PSD of the beat note between 0^{th} comb mode and the tunable CW laser could be illustrated by the black curve in Fig. 3-20 (c), which includes the sum of 0^{th} comb mode and tunable CW laser's phase noise. It is expected that the phase noise PSD of the beat note between n^{th} comb mode and the tunable CW laser could be explained by the red curve. Compared to the black curve, the red curve is higher at high Fourier frequency because of accumulated phase noise. The phase noise of two curves at low Fourier frequency is due to the slow drift of the tunable CW laser.

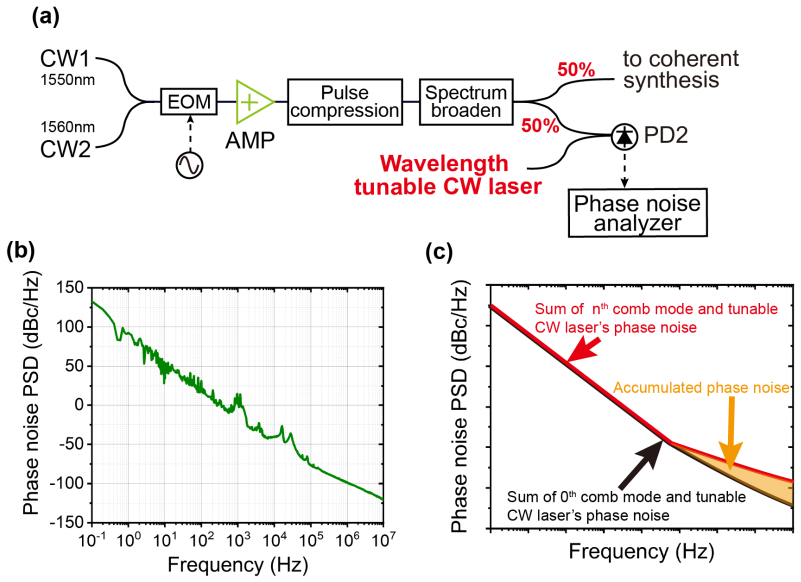

Fig. 3-20 (a) System setup of measuring the phase noise PSD of comb modes in coherently synthesized two-color EO comb. (b) Phase noise PSD of the wavelength tunable CW laser. (c) Illustration of phase noise PSD of the beat note between the comb modes in coherently synthesized two-color EO comb and the tunable CW laser.

In the measurement, the wavelength of the tunable CW laser is tuned from 1547.5 nm to 1565 nm with a 2.5-nm step. The phase noise performance of the comb modes that located from 1547.5 nm to 1565 nm with 2.5 nm step is shown in Fig. 3-21. Here only the phase noise PSD from 10 kHz to 10 MHz Fourier frequency is displayed for two reasons: (1) the accumulated phase noise from RF synthesizer dominates the phase noise of comb modes at this frequency range; (2) slow drift of the tunable CW laser dominates the phase noise PSD at low Fourier frequency. From Fig. 3-21, the comb modes at two center wavelengths (i.e., 1550 nm and 1560 nm) have the lowest phase noise PSD of all the comb modes. The phase noise PSD of other comb modes increases gradually as they are away from the center wavelengths, attributing to the phase noise accumulation from the RF synthesizer. The sharp spikes in the phase noise PSD of comb modes located at > 1555 nm are introduced by the phase-locked loop, since the coherent synthesis of the two EO combs is realized through feedback the error signal to the 1560-nm CW laser. Through optimizing the parameters of the phase-locked loop, these sharp spikes could be reduced to some extent.

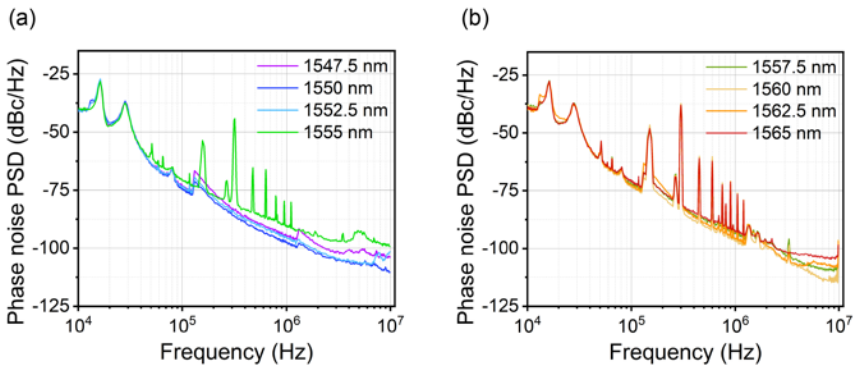

Fig. 3-21 (a): Phase noise PSDs of f_{beat2} when the tunable CW laser beats with the comb modes in two-color EO comb located from 1547.5 nm to 1555 nm; (b): phase noise PSDs of f_{beat2} when the tunable CW laser beats with the comb modes in two-color EO comb located from 1557.5 nm to 1565 nm.

Then the phase noise PSDs of the comb modes are compared with that in a single-color EO comb. The configuration of the single-color EO comb is shown in Fig. 3-22 (a). One CW laser centered at 1550 nm (the same CW1 as in Fig. 3-15) is modulated by the same EO modulators. The total modulation index to PMs is also about 7π. Two-stage EDFA, a piece of 500-m SMF and a piece of HNLF are utilized for power amplification, pulse compression and spectrum broadening, respectively. The power after EYDFA is 1W. The pulse width after 500-m SMF is 1 ps. The spectrum after HNLF is shown in Fig. 3-22 (b). The comb modes centered from 1547.5 nm to 1565 nm in the single-color EO comb beat with the wavelength tunable CW laser separately. The measured phase noise PSDs are shown in Fig. 3-22 (c). The phase noise PSD of the comb modes is remarkably growing from the center of the single-color EO comb.

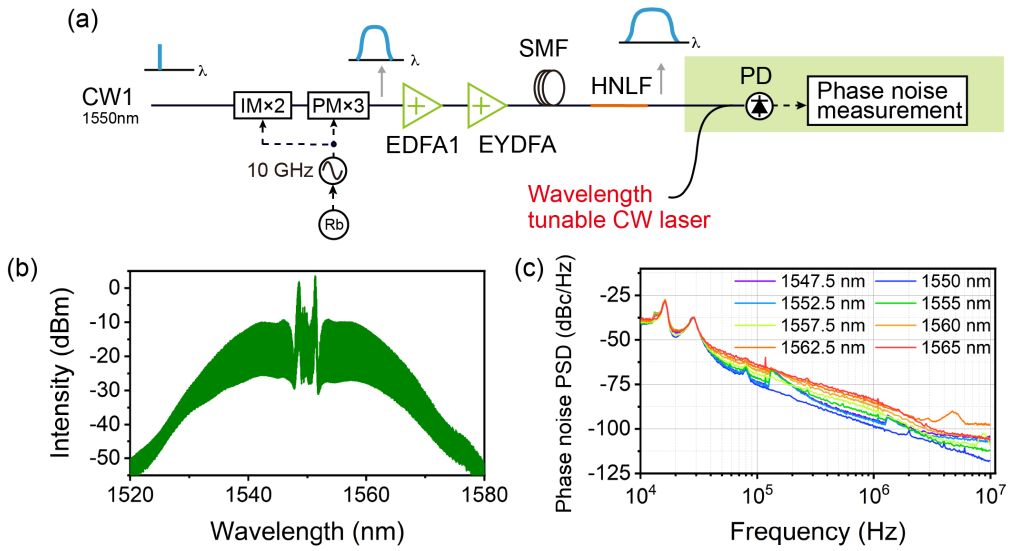

Fig. 3-22 (a): Experimental setup of single-color EO comb centered at 1550 nm. (b) Optical spectrum of single-color EO comb. (c) Phase noise PSDs of comb modes in the single-color EO comb.

The phase noise PSD at 1 MHz Fourier frequency of comb modes in single-color EO comb and two-color EO comb are plotted in Fig. 3-23 (a), as the blue curve and green curve. The blue curve has a "V" shape, where the comb mode at 1550 nm has the lowest phase noise PSD at 1 MHz Fourier frequency. As the wavelength separation between the comb mode and central comb mode increases, the phase noise PSD at 1 MHz Fourier frequency gradually increase. This is consistent with phase noise measurement results in Ref. [4]. The slope is related to the phase noise of the RF synthesizer. However, in two-color EO comb, the comb modes at 1550 nm and 1560 nm have the lowest phase noise PSD of all the comb modes because they are both the central comb modes. The green curve is W-shaped, which is same as the analysis in Chapter 3.2. The suppression of accumulated phase noise at > 1555 nm wavelength range is highlighted by the red arrow.

In addition, the phase noise PSDs are integrated from 10 MHz to 50 kHz and the integrated jitter is in Fig. 3-23 (b), where the blue curve and green curve correspond to single-color EO comb and two-color EO comb, respectively. The shapes of the two curves are similar as in Fig. 3-23 (a), indicating the suppression of accumulated phase noise at high Fourier frequency. To this end, the phase noise accumulation from RF oscillator at high Fourier frequency is suppressed effectively in the coherently synthesized two-color EO comb.

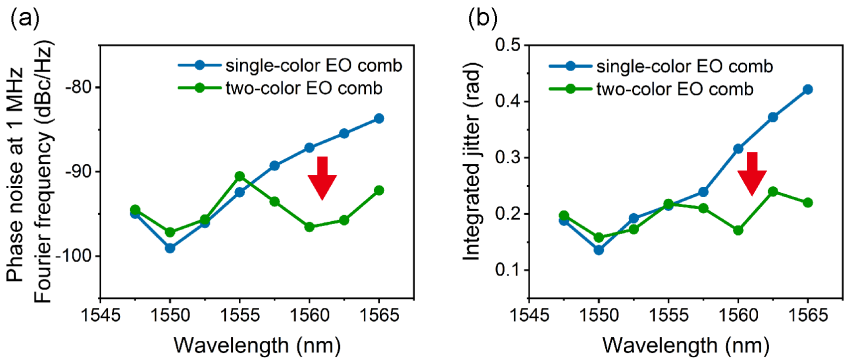

Fig. 3-23 Phase noise comparison between single-color EO comb and two-color EO comb. (a): Phase noise PSD at 1 MHz Fourier frequency. (b): Comparison of integrated jitter. Measured data are highlighted as filled dots.

3.4 Coherently synthesized 1535/1560 nm two-color EO comb

A broadband coherently synthesized two-color EO comb is demonstrated in this section. The experimental setup is shown in Fig. 3-24, which is similar to the setup in Fig. 3-15 (a). CW2 (RIO, PLANEX) and CW3 (TOPTICA, CTL1550) are single frequency continuous lasers that centered at 1560 nm and 1535 nm, respectively. The power of CW2 and CW3 is 19 mW and 8 mW, respectively. CW2 and CW3 are modulated by two intensity modulators and three phase modulators simultaneously. The repetition rate is 10 GHz. The total modulation index of PMs is 7π. A home-made EDFA is utilized amplify the power from 0.4 mW to 100 mW. The two EO combs are located 25 nm away from each other. The spectrum bandwidth of each EO comb is 3 nm. Therefore, the coherent synthesis of the two EO combs requires a broader spectrum of each EO comb with overlapped comb modes in between.

This means that Fourier transform-limited pulse durations of the two EO comb are both required at the input of HNLF. Therefore, a piece of common SMF is not suitable for pulse compression anymore, because of it has different group velocity dispersion (GVD) at the two center wavelengths. In fact, the dispersion of SMF-28 at 1535 nm is 16.577 ps/nm/km, while the dispersion is 18.038 ps/nm/km at 1560 nm [19]. According to the simulation demonstrated in Chapter 3.1, 470-m SMF28 is required to compress the pulse from 1560-nm EO comb with 1-W average power. Then, the optimized length of the SMF-28 for compressing the pulses from the 1535-nm EO comb should be 511 m (18.038 ps/nm/km×470 m/16.577 ps/nm/km =511 m).

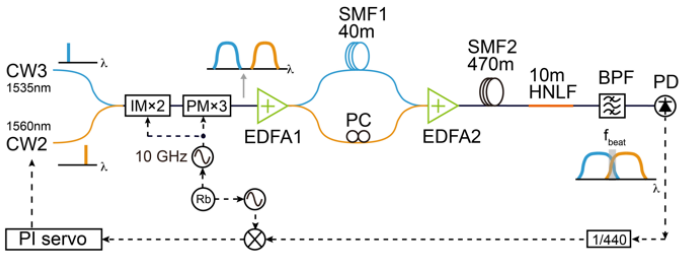

Fig. 3-24 Experimental setup for two-color EO comb with 25 nm center wavelength separation. PC: polarization controller.

To solve this problem, at the output of EDFA, the two-color EO comb is divided through a wavelength division multiplexer (WDM). A piece of SMF (SMF1) is inserted in the 1535-nm path for individual pulse compression. A polarization controller (PC) is inserted in the 1560-nm path for polarization adjusting. Due to the non-polarization maintaining configuration of the EDFA, the two EO combs have different polarization state at the output of EDFA. Therefore, the PC plays a significant role to ensure the same polarization state of the two EO combs, which is essential to get a beat note with enough SNR. The recombined 1535/1560-nm EO comb goes into EYDFA and SMF2. During the experiment, two steps are done to realize individual pulse compression: (1) adjusting the length of SMF2 until the pulse of 1560-nm EO comb is the shortest; (2) adjusting the length of SMF1 until the pulse of 1535-nm EO comb is the shortest. In this case, the length of SMF1 and SMF2 are 40 m and 470 m, respectively. The reason that the pulse is compressed after power scaling is to avoid high nonlinearity in the EYDFA.

The configuration of EDFA and EYDFA are previously illustrated in Fig. 3-16. However, take the higher net gain of the EYDFA at 1560 nm into consideration, the length of the gain fiber and the input power of the two EO combs to the EYDFA should be carefully chosen to balance the output power of the two EO combs. This is the reason why the power of CW3 is much lower than the power of CW2. The length of the EYDF is shorten to 2.58 m comparing to the 1550/1560 nm two-color EO comb. At the output of EYDFA, the power of the 1535-nm and 1560-nm EO comb is 0.90 W and 0.92 W when the pump power of EYDFA is 8 W, respectively. When the pump power of EYDFA is set to 9 W, the corresponding output power of 1535-nm and 1560-nm EO comb is 1.06 W and 0.97 W. The FWHM pulse width are 0.827 ps and 0.780 ps for 1535-nm EO comb and 1560-nm EO comb when the pump power of EYDFA is 9 W, respectively, as shown in Fig. 3-25. The pulse width is a little bit

broader when the pump power of EYDFA is set to 8 W. These parameters are listed in Table 1.

Table 1 Pulse width and output power of 1535-nm and 1560-nm EO comb

Pump power of EYDFA (W)		8	9
1535-nm EO comb	Pulse width (ps)	0.856	0.827
	Output power (W)	0.90	1.06
1560-nm EO comb	Pulse width (ps)	0.840	0.780
	Output power (W)	0.92	0.97

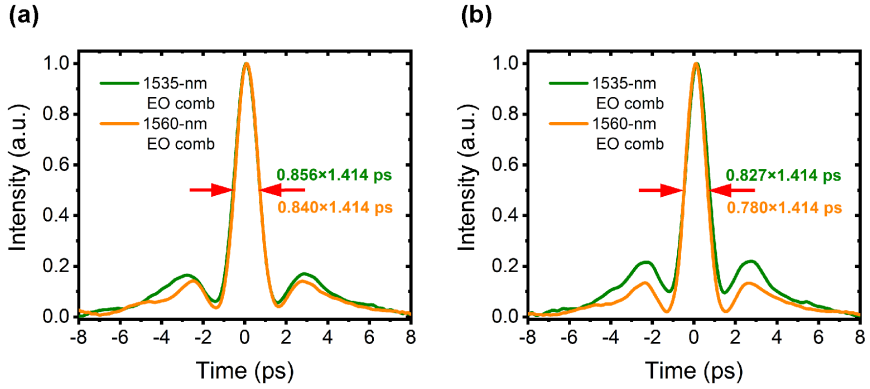

Fig. 3-25 Autocorrelation trace of 1535-nm EO comb and 1560-nm EO comb. (a): Pump power of EYDFA is 8 W. (b): Pump power of EYDFA is 9 W.

Finally, two broadened optical spectra with overlapped comb modes are obtained at the output of 10-m HNLF, as shown in Fig. 3-26 (a). The spectrum range of this 1535/1560 nm two-color EO comb reaches to 60 nm, which is much broader than the 1550/1560 nm two-color EO comb.

Same as Chapter 3.3.1, the overlapped comb modes are filtered in the 1535/1560 nm two-color EO comb through a bandpass filter, as illustrated by the orange curve in Fig. 3-26 (a). The beat note between the overlapped comb modes is detected by a photodetector. The beat signal is phase locked to a radio frequency reference through current feedback to CW2. The frequency fluctuation of f_{beat} within 20 min is shown in Fig. 3-26 (b). The gate time is 100 ms. The standard deviation of f_{beat} is 0.167 Hz. The Allan deviation of f_{beat} is shown in Fig. 3-26 (c). The stability of f_{beat} is 3×10^{-16} in 1 s averaging time. The standard deviation and Allan deviation of f_{beat} are a little bit worse than those of 1550/1560 nm two-color EO comb, which could be attributed to the noisier f_{beat} signal due to more accumulated phase noise. The phase noise PSD of f_{beat} before and after phase locking are plotted in Fig. 3-26 (d), as the green curve and

orange curve. The locking bandwidth is about 3 kHz. The phase noise within locking bandwidth is effectively suppressed by the phase lock loop. Compared to Fig. 3-18 (c), there are some spikes from 500 Hz to 50 kHz offset frequency in the phase noise PSD spectrum of f_{beat} in Fig. 3-26 (d). This is caused by acoustic noise which CW3 is very sensitive to. According to the analysis in Chapter 3.2.2, in this 1535/1560 nm two-color EO comb, more phase noise of comb modes is suppressed than the previous case with 1550/1560 nm two-color EO comb.

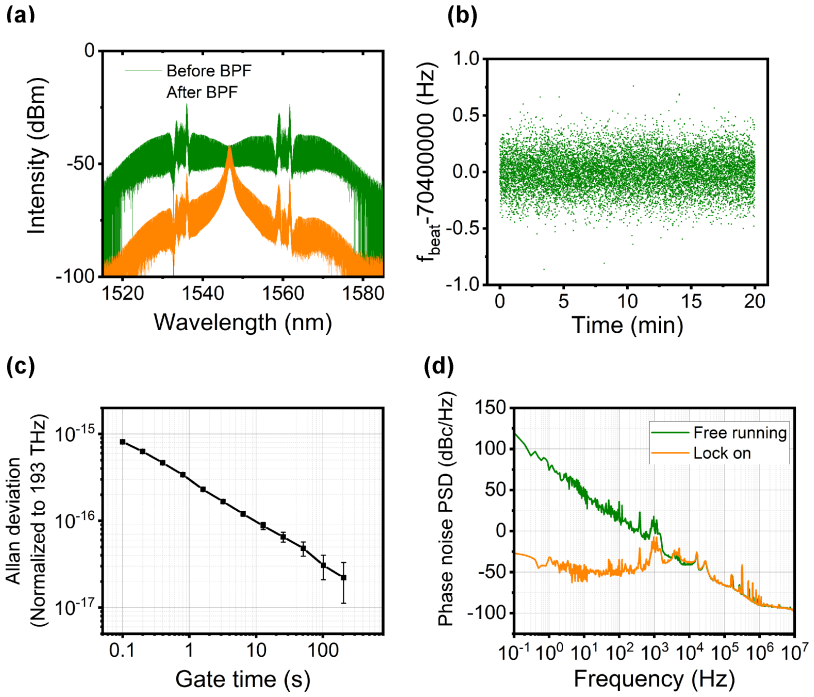

Fig. 3-26 (a): Optical spectrum of after HNLF of two-color EO comb with 25 nm center wavelength separation (green curve). Optical spectrum of the bandpass-filtered 1535/1560 nm coherently synthesized two-color EO comb (orange curve). (b): Frequency fluctuation of f_{beat} in 20 min. (c): Allan deviation of f_{beat}. (d): Phase noise PSD of f_{beat} before and after phase locking.

In the broadband coherently synthesized two-color EO comb, the largest wavelength separation between the two CW lasers is restricted by the gain spectrum of EDFA. With larger wavelength separation, the optimization of EDFA becomes more difficult to realize power amplification simultaneously of the two EO combs. Besides, the phase locking of the beat note between the two EO combs becomes harder due to accumulated phase noise and decreased SNR.

3.5 Compact coherently synthesized two-color EO comb

After constructing two coherently synthesized two-color EO combs and finishing

proof-of-principle experiments, a compact aluminum box is designed for the coherently synthesized two-color EO comb. There are three floors inside the box, containing the optical devices before EYDFA in Fig. 3-24. Detailed information of each floor is shown as follows:

1. First floor: the experimental setup on the first floor is shown in Fig. 3-27 (a). It contains a WDM, two EO intensity modulators, three EO phase modulators, an isolator and an optical coupler. The WDM is used to combine the outputs from the two CW lasers. The two channels of the WDM have operating wavelengths of 1530 nm to 1545 nm and 1547 nm to 1570 nm, respectively, as shown in Fig. 3-28. The isolation of the two channels are 30 dB and 45 dB, respectively. The two IMs are both modulated by 10-GHz RF signals with $V_{\pi IM}/2$ amplitude and DC biased at $V_{\pi IM}/2$. Considering that the half wave voltage of each IM is slightly different, the amplitude of the driven signals and the bias voltage are slightly different. For example, the bias voltages for IM1 and IM2 are 6.9 V and -3.2 V, respectively. The three PMs are both driven by 10-GHz RF signals with 33 dBm power. The ISO is used to guarantee the uni-directional propagation. 1% of the output is extracted by an optical coupler, which serves as monitor output. All the fibers on the first floor are polarization maintaining fiber.

Fig. 3-27 (b) gives the photo of first floor. The inputs and outputs are marked by red arrows. The bottom board of the first floor is made of copper for thermal dissipation. A 10 k-ohm thermistor is sticked on the floor for temperature control.

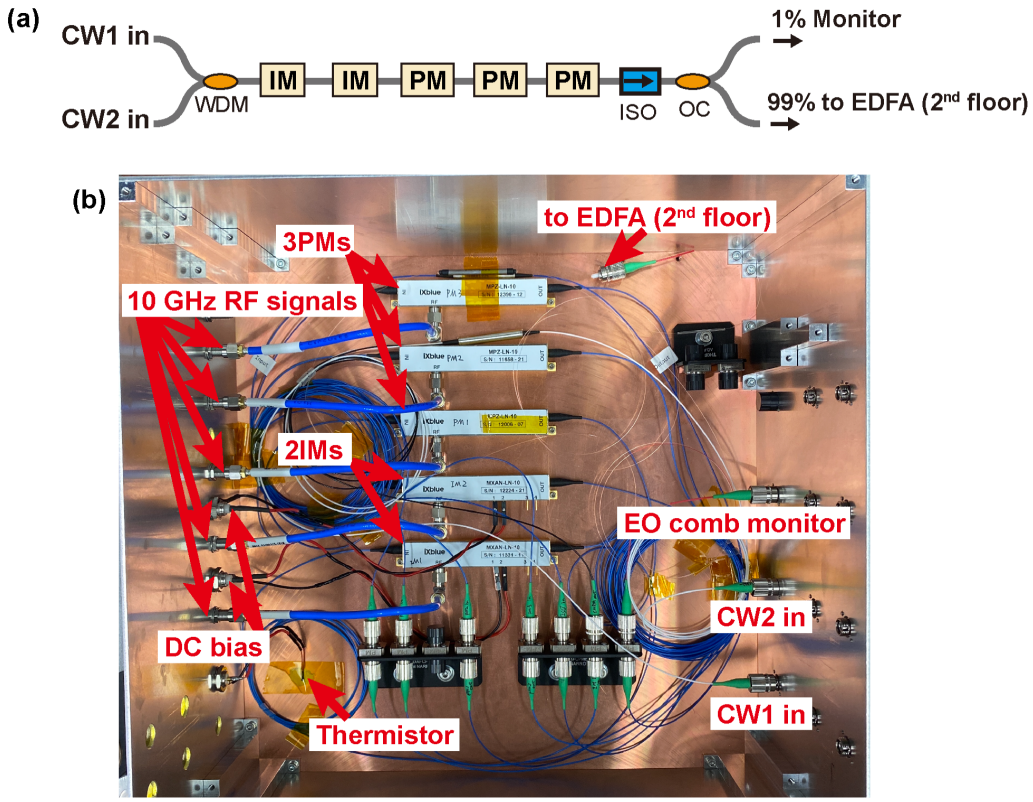

Fig. 3-27 (a): Experimental scheme of first floor. (b): Photo of first floor.

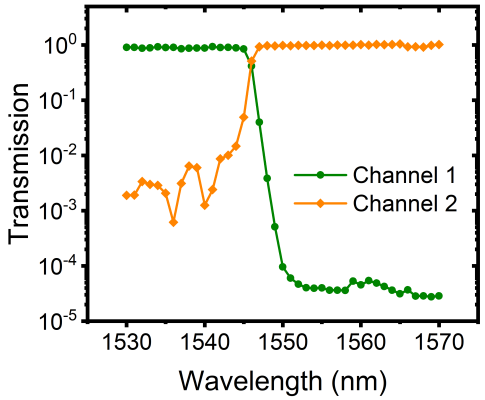

Fig. 3-28 Transmission of the WDM. Green curve: channel 1; Orange curve: channel 2.

2. Second floor: the experimental setup on the second floor is shown in Fig. 3-29 (a). It contains an EDFA, an isolator and an optical coupler. The fiber patch cord from the first floor passes through the gap at the top right of the box and connects to the input patch cord of the EDFA. The configuration of the EDFA is illustrated in Fig. 3-16. The ISO is used to ensure the uni-directional propagation of the EO comb and to protect the EDFA against the back scatter light from EYDFA. At the output of the ISO,

30 percent power is extracted through an optical coupler. This part could be used for applications, such as distance measurement, low noise microwave generation, THz generation, and so on. The photo of the second floor is shown in Fig. 3-29 (b). The bottom board of the second floor is also made of copper. On the second floor, all the fibers are non-polarization maintaining fiber.

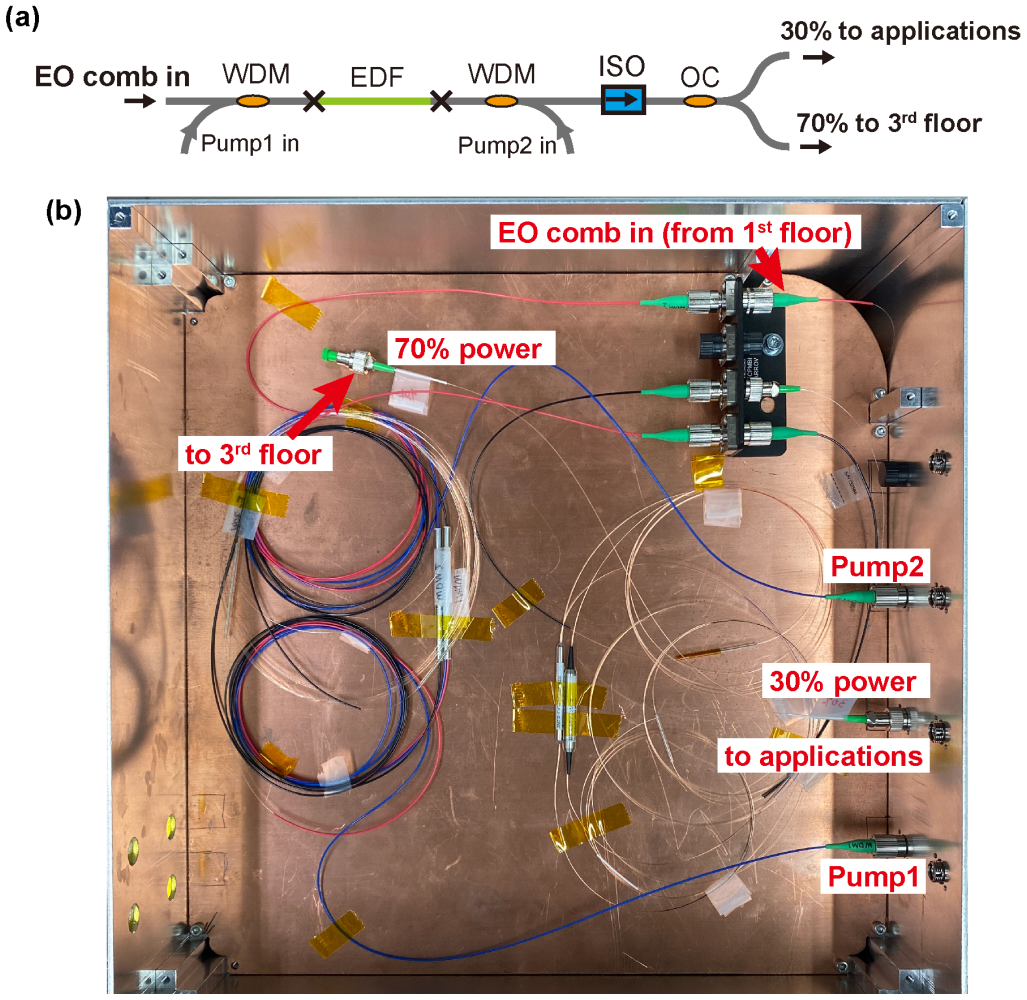

Fig. 3-29 (a): Experimental scheme of second floor. (b): Photo of second floor.

3. Third floor: the experimental setup on the third floor is shown in Fig. 3-30 (a). It comprises two WDMs, a piece of single-mode fiber and two waveplates sandwiched in between, and an isolator. The purpose of these optical components is to realize the dispersion compensation of the two EO combs at distinct center wavelengths. The two WDMs have same specifications with the WDM shown in Fig. 3-28, except that the two WDMs have non-polarization maintaining fiber pigtails. The length of the SMF1 is 40 m. According to the GVD of SMF-28, this piece of SMF should be in the optical path of the EO comb with shorter center wavelength. The

polarization controller (made of a half waveplate and a quarter waveplate) is used to adjust the polarization state. The ISO is utilized to reject backward reflections. The photo of the third floor is shown in Fig. 3-30 (b). The fiber connection between the second floor and the third floor is realized through the same way as the fiber connection between the bottom two floors. The bottom board of the third floor is made of copper, too.

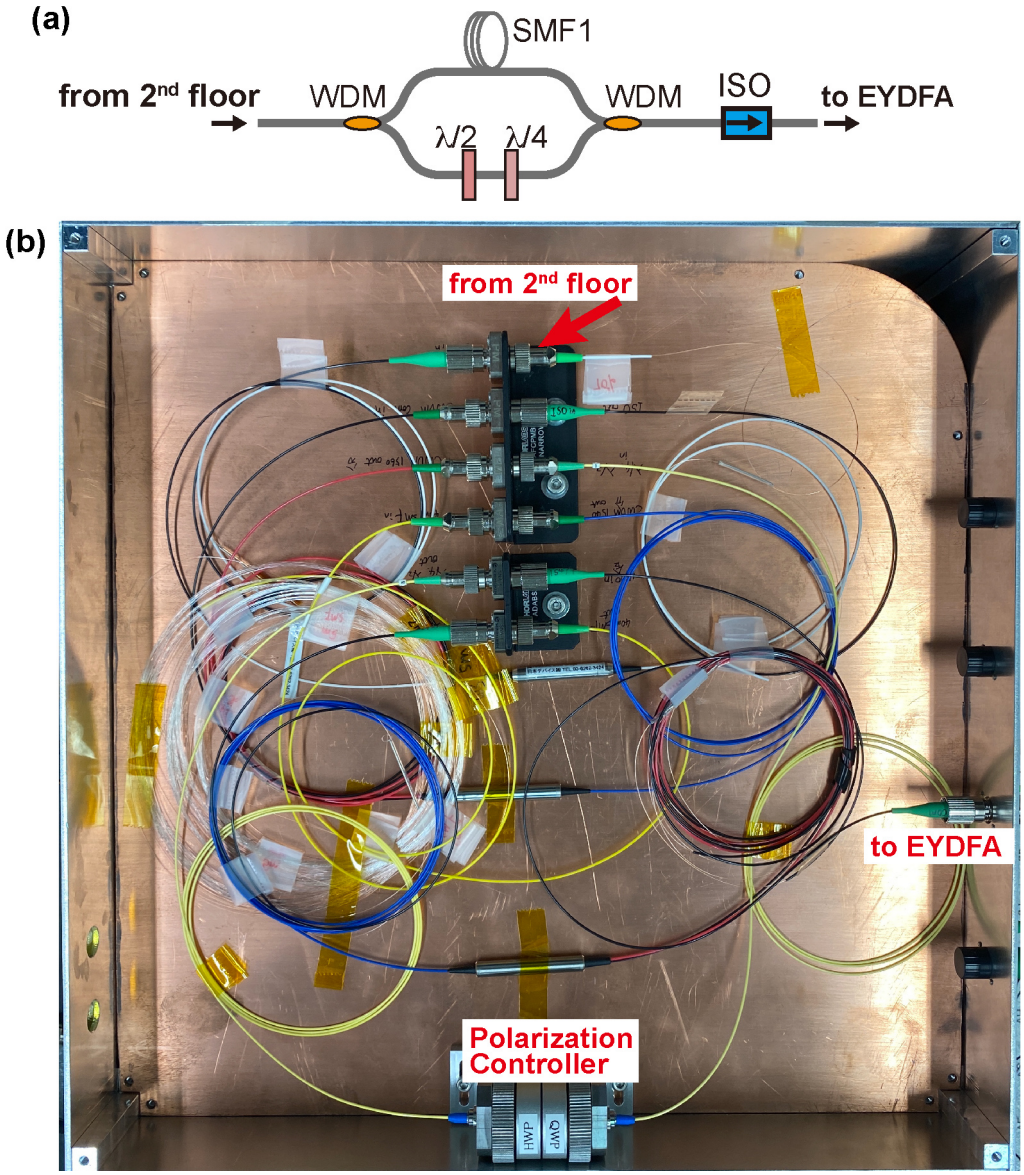

Fig. 3-30 (a): Experimental scheme of third floor. (b): Photo of third floor.

The overall look of the box is shown in Fig. 3-31.

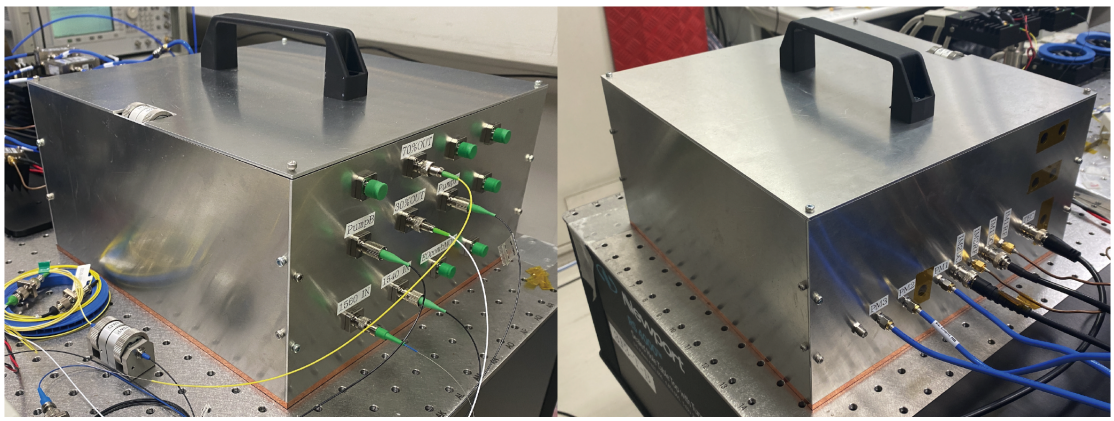

Fig. 3-31 The overall look of the box.

3.6 Summary of this chapter

The simulations of EO comb generation and EO pulse compression are performed in the beginning of this chapter. In the simulation, the performance of the EO combs and the key points that should be taken into consideration are illustrated.

Then the principle of coherently synthesized two-color EO comb is explained, showing the advantages of broad spectrum and low phase noise. Two coherently synthesized two-color EO combs centered at 1550/1560 nm and 1535/1560 nm are constructed, to demonstrate the advantages. The suppression of accumulated phase noise is experimentally verified in the 1550/1560 nm coherently synthesized two-color EO comb. In the coherently synthesized 1535/1560 nm two-color EO comb, the spectrum range reaches 60 nm.

Finally, the coherently synthesized two-color EO comb is compacted in a self-designed mechanical box.

3.7 References

[1] D. R. Carlson, D. D. Hickstein, W. Zhang, A. J. Metcalf, F. Quinlan, S. A. Diddams and S. B. Papp. Ultrafast electro-optic light with subcycle control[J]. Science, 2018, 361(6409): 1358-1363.

[2] D. C. Cole, K. M. Beha, S. A. Diddams and S. B. Papp. Octave-spanning supercontinuum generation via microwave frequency multiplication[C]//Journal of Physics: Conference Series. IOP Publishing, 2016, 723(1): 012035.

[3] A. Ishizawa, T. Nishikawa, A. Mizutori, H. Takara, H. Nakano, T. Sogawa, A. Takada, and M. Koga, Generation of 120-fs laser pulses at 1-GHz repetition rate

derived from continuous wave laser diode[J]. Optics express, 2011, 19(23): 22402-22409.

[4] A. Ishizawa, T. Nishikawa, A. Mizutori, H. Takara, A. Takada, T. Sogawa, and M. Koga, Phase-noise characteristics of a 25-GHz-spaced optical frequency comb based on a phase-and intensity-modulated laser[J]. Optics express, 2013, 21(24): 29186-29194.

[5] A. J. Metcalf, V. T. Company, D. E. Leaird, and A. M. Weiner, High-power broadly tunable electrooptic frequency comb generator[J]. IEEE Journal of Selected Topics in Quantum Electronics, 2013, 19(6): 231-236.

[6] A. J. Metcalf, C. D. Fredrick, R. C. Terrien, S. B. Papp, and S. A. Diddams. 30 GHz electro-optic frequency comb spanning 300 THz in the near infrared and visible[J]. Optics Letters, 2019, 44(11): 2673-2676.

[7] A. Ishizawa, T. Nishikawa, K. Hara, K. Hitachi, T. Sogawa, and H. Gotoh, "Carrier-envelope-offset locking of 25-GHz EOM comb based on a free-running CW Laser Diode," in Conference on Lasers and Electro-Optics, 2018, paper SM4L.5.

[8] J. M. Dudley, G. Genty, S. Coen. Supercontinuum generation in photonic crystal fiber[J]. Reviews of modern physics, 2006, 78(4): 1135.

[9] R. Wu, V. R. Supradeepa, C. M. Long, D. E. Leaird, and A. M. Weiner. Generation of very flat optical frequency combs from continuous-wave lasers using cascaded intensity and phase modulators driven by tailored radio frequency waveforms[J]. Optics letters, 2010, 35(19): 3234-3236.

[10] V. T. Company, J. Lancis, P. Andrés. Lossless equalization of frequency combs[J]. Optics letters, 2008, 33(16): 1822-1824.

[11] R. Wu, D. E. Leaird, A. M. Weiner. Supercontinuum-based 10-GHz flat-topped optical frequency comb generation[J]. Optics express, 2013, 21(5): 6045-6052.

[12] X. Zhang, J. Zhang, K. Yin, Y. Li, X. Zheng, and T. Jiang. Sub-100 fs all-fiber broadband electro-optic optical frequency comb at 1.5 μm[J]. Optics Express, 2020, 28(23): 34761-34771.

[13] K. Beha, D. C. Cole, P. Del'Haye, A. Coillet, S. A. Diddams, and S. B. Papp. Electronic synthesis of light[J]. Optica, 2017, 4(4): 406-411.

[14] A. Parriaux, K. Hammani, G. Millot. Electro-optic frequency combs[J]. Advances in Optics and Photonics, 2020, 12(1): 223-287.

[15] J. Kim, D. J. Richardson, R. Slavík. Cavity-induced phase noise suppression in a Fabry–Perot modulator-based optical frequency comb[J]. Optics Letters, 2017, 42(8): 1536-1539.

[16] W. Kokuyama, H. Nozato, T. R. Schibli. Phase meter based on zero-crossing counting of digitized signals[J]. arXiv preprint arXiv:2009.01137, 2020.

[17] D. J. Jones, S. A. Diddams, J. K. Ranka, A. Stentz, R. S. Windeler, J. L. Hall, and S. T. Cundiff. Carrier-envelope phase control of femtosecond mode-locked lasers

and direct optical frequency synthesis[J]. Science, 2000, 288(5466): 635-639.
[18] S. Koke, C. Grebing, H. Frei, A. Anderson, A. Assion, and G. Steinmeyer. Direct frequency comb synthesis with arbitrary offset and shot-noise-limited phase noise[J]. Nature Photonics, 2010, 4(7): 462-465.
[19] http://www.photonics.byu.edu/FiberOpticConnectors.parts/images/smf28.pdf

Chapter 4. Absolute distance measurement based on a fiber type interferometer and a coherently synthesized two-color EO comb

In this chapter, the coherently synthesized two-color EO comb is applied to distance measurement. This distance measurement system is based on a fiber-type interferometer. The single wavelength interferometry and synthetic wavelength technique are used in the measurement, resulting in high resolution distance measurement in extended non-ambiguity range. Benefiting from the low phase noise characteristic of the two-color EO comb and the high comb mode power, nm-level resolution is achieved. The dead path error, cyclic error and acoustic noise in the system are evaluated systematically. The proof-of-principle experiment is realized, including absolute distance measurement and fast displacement measurement.

4.1 Method and Experimental setup

The coherently synthesized two-color EO comb that demonstrated in Chapter 3 is applied to absolute distance measurement. In the following, the coherently synthesized two-color EO comb is abbreviated to CSEOC. The center wavelengths of the CSEOC are 1540 nm and 1560 nm. As illustrated in Fig. 3-29, 30 percent power (30 mW) of the CSEOC is extracted for distance measurement. Then, a piece of 560-m single-mode-fiber is used to realize pulse compression. The pulse width is 2 ps after compression, which is nearly transform-limited duration. This pulse train is directed to the absolute distance measurement system.

The experimental setup of the absolute distance measurement system is shown in Fig. 4-1. This system is based on a fiber type interferometer. The advantage of fiber type interferometer is its capability of integration. A 2×2 coupler divides the CSEOC into the reference arm and the target arm. An acousto-optic frequency shifter (AOFS) with 80 MHz center frequency is inserted in the reference path. This AOFS is fiber-pigtailed. A Faraday rotator mirror (FRM) is used as the reference mirror. A fiber collimator in the target arm couple the laser into free space. A target gold mirror is installed on a motorized stage (Suruga Seiki, KS102-100-2). The length of the fiber in

the reference arm and target arm is the same, which are 5 meters. The fibers in reference arm and target arm are put together to minimize the impact of their length fluctuation on the measurement results. The path length difference between the reference path and the target path is set to four times of the distance separation between adjacent pulses. Hence the pulses reflected from the reference arm and the target arm are overlapped and interfere at the output of 2×2 coupler. After the reflected pulses are separated by a WDM, two heterodyne signals, which are contributes by the comb modes near the two center wavelengths, are detected by two photodetectors (Newport 1611). The two heterodyne signals are labeled as 1560-nm heterodyne signal and 1540-nm heterodyne signal, respectively. Due to double pass of the AOFS, the frequency of the heterodyne signals is 160 MHz. The phase (φ) of the 1560-nm heterodyne signal is detected by a lock-in-amplifier (Stanford Research Systems, SR844). As a result, the distance under-test, D_p, could be obtained through $D_p = \varphi\lambda/4\pi n_p + N_1\lambda/2n_p$, where λ is 1560 nm, N_1 is an integer and n_p is phase refractive index of air. This method is so-called single-wavelength interferometry, which is explained in Section 2.2.1. The non-ambiguity range of the single-wavelength interferometry is $\lambda/2 = 780\ nm$.

Meanwhile, the phase difference between the two heterodyne signals is detected through another lock-in-amplifier, resulting in phase measurement of synthetic-wavelength interferometry. The measurement result of synthetic-wavelength interferometry is expressed by $D_g = \Phi\Lambda/4\pi n_g + N_2\Lambda/2n_g$, where Φ is the phase difference between the two heterodyne signals, $\Lambda = (\lambda_1 - \lambda_2)/(\lambda_1 \cdot \lambda_2) = 120\ \mu m$ is the synthetic wavelength, N_2 is an integer and n_g is group refractive index of air. The non-ambiguity range of the synthetic-wavelength interferometer is $\Lambda/2 = 60\ \mu m$. By combining D_p and D_g measurement, the integer N_1 is obtained, leading to the extension of non-ambiguity range from 780 nm to 60 μm. The integer N_2 could be determined through other methods with larger non-ambiguity range. Note that the D_p and D_g are related to the phase and group refractive index of air, respectively. Benefiting to the small difference between phase and group refractive index, self-correction of air refractive index could be realized through two-color method in the future [1][2][3].

The distance measurement result from a commercial HeNe interferometer (Keysight, 5517C) serves as the reference. Its target mirror is mounted on the same motorized stage, as shown in Fig. 4-1.

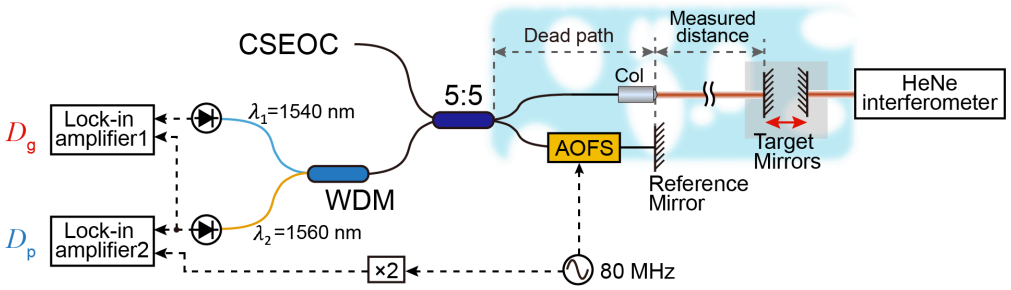

Fig. 4-1 Experimental setup of absolute distance measurement system based on a fiber interferometer and coherently synthesized two-color EO comb. CSEOC: coherently synthesized two-color EO comb; Col: collimator; WDM: wavelength division multiplexer; AOFS: acousto-optic frequency shifter.

4.2 System error and performance

In this section, the system performances are investigated, including the dead path error, the short-term and long-term stability of D_p and D_g, the linearity and the cyclic error.

4.2.1 Dead path error

In distance measurement, the zero point is the point where target path equals to reference path. The path before the zero point is called as dead path, as explained in Fig. 4-2. The length uncertainty of the dead path leads to the uncertainty of zero point's position, hence deteriorates the measurement results. The length uncertainty of the dead path is called as dead path error.

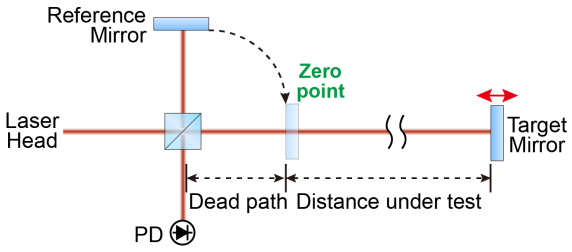

Fig. 4-2 Schematic of zero point and dead path in distance measurement system.

Corresponding to the system setup in Fig. 4-1, the dead path error contains the fiber length fluctuation in reference path and target path, which is attributed to environmental parameters fluctuation. Particularly, in a single-mode fiber with $n = 1.4679$, $\alpha_L \approx 0.5 \times 10^{-6}\,K^{-1}$, $dn/dT \approx 10^{-5}\,K^{-1}$, the temperature induced

relative optical path length change can be quantified as: $(\Delta D/\Delta T)/L = 10.7\ \mu m/(K \cdot m)$ [4][5][6]. The dead path error is investigated by measuring length fluctuation of reference path. At first, the length of fiber in reference path and target path are 5 m and 0.3 m, respectively, as shown in Fig. 4-3 (a). Since the fiber in target path is much shorter than that in reference path, D_p mainly reflects the length fluctuation of reference path, as the green curve in Fig. 4-4. Here, D_p is calculated from unwrapped phase of the heterodyne signal. Although 13 hours are spent for system warming up, the length of fiber is still drifting. The length fluctuation of the fiber in reference path is 15 μm within 40 min. Meanwhile, the temperature fluctuation near the reference path is recorded using a thermometer (Fluke, 1560), which is around 0.16 ℃. This corresponds well with the length fluctuation of the double-passed 5-m fiber.

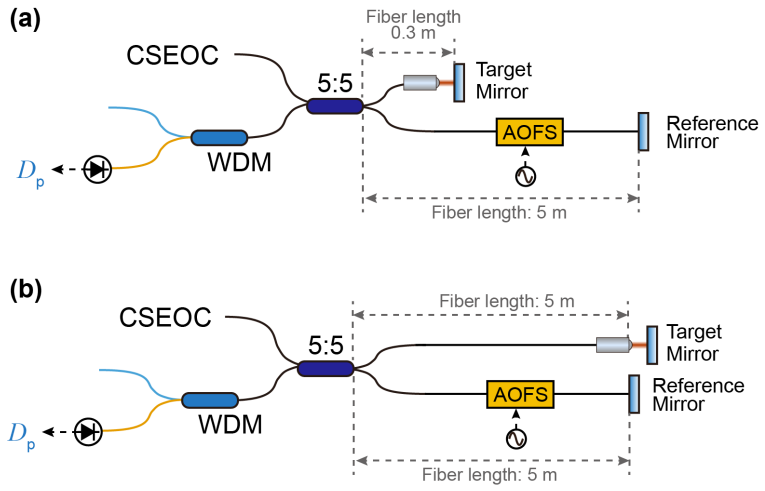

Fig. 4-3 Experimental setup of investigating the dead path error. (a): The length of fiber in target path is 0.3 m. (b): The length of fiber in target path is same as that in reference path. The fiber in target path and reference path are put together.

As a comparison, the length of fiber in reference path and target path are both set to 5 m, as illustrated in Fig. 4-3 (b). The fibers are wrapped together to minimize the environmental influence. The measured D_p indicates the relative length fluctuation between the two paths. As shown in Fig. 4-4, the relative path length fluctuation is less than 6 μm within 40 min. The system warm-up time is 5 h. Although the length of fiber is still fluctuation, the drift becomes smaller. Thus less warm-up time is required.

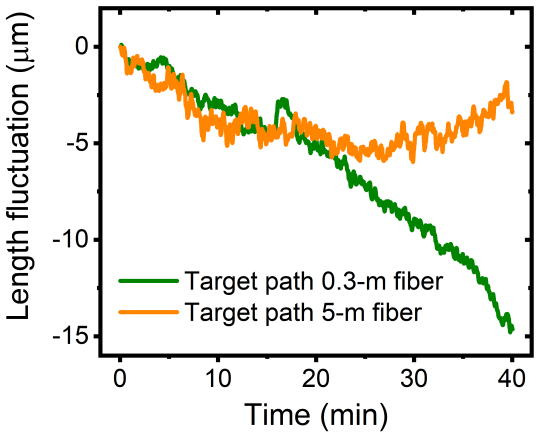

Fig. 4-4 Dead path error induced by environmental instability. Green curve and orange curve correspond to the measurement results through system setup in Fig. 4-3 (a) and (b), respectively.

Besides dead path error induced by the fiber length fluctuation due to temperature drifting, air flow is another important factor that affects the dead path error, since the temperature of the fiber could change rapidly due to the air flow. In laboratory environment, air flow is mainly caused by air conditioning and ventilation system. To verify this, the system setup in Fig. 4-3 (b) is implemented. For the sake of comparison, the measured D_p in three situations are shown in Fig. 4-5. These three situations are in open air, not well covered by a styrofoam box and well covered by a styrofoam box, respectively. Apparently, there is a period of ~500 s in the red curve and the orange curve. Compare to the open air situation, both the amplitude of the periodic fluctuation and the slow drifting are much smaller when the system is not very well covered by a styrofoam box. Moreover, this period disappears when the system is well covered by a styrofoam box, as the green curve. In the following experiment, the system is placed in a styrofoam box in order to isolated temperature fluctuation and air flow as much as possible.

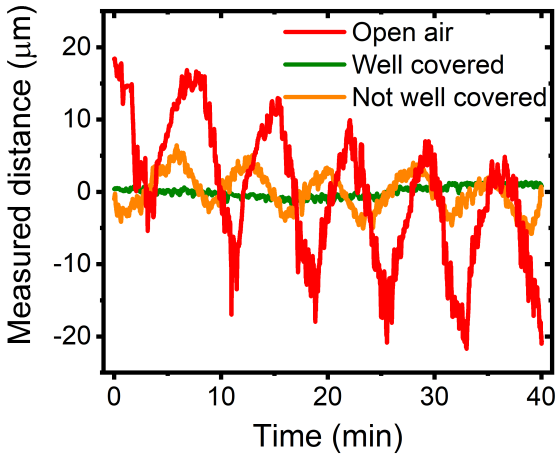

Fig. 4-5 The dead path error induced by air flow. Red curve: the system is in open air. Orange curve: the system is not well covered by a styrofoam box. Green curve, the system is very well covered by a styrofoam box. The periodic fluctuation disappears when the system is well covered by a Styrofoam box.

4.2.2 System error due to acoustic noise

Acoustic noise can cause weak vibration of air, which also affects the system performance. The frequency of acoustic noise is usually from 10 to 1000 Hz. In the CSEOC, the acoustic noise of the multi-mode pump laser for EYDFA is very high. This acoustic noise deteriorates the distance measurement precision, which is investigated in the following.

Considering that coherent synthesis of the two-color EO comb requires the EYDFA, the investigation of acoustic noise contains three measurements: 1) the pump laser is turned on and the two-color EO comb is coherently synthesized; 2) the pump laser is turned on and the two-color EO comb is not coherently synthesized; 3) the pump laser is turned off and the two-color EO comb is not coherently synthesized. The update rate of the measurement is 10 kHz. The fast Fourier transform spectra of the measured distance are shown in Fig. 4-6 (a). Obviously, there are two bumps around 390 Hz and 530 Hz. The intensity of the bumps gets very strong when the multi-mode pump is turned on. Through filtering out the bumps digitally, the distance measurement error due to the acoustic noise is revealed, as shown in Fig. 4-6 (b). The amplitude of this error is around $\pm$ 5 nm. This system error is possible to be reduced by utilizing a pump laser with smaller acoustic noise.

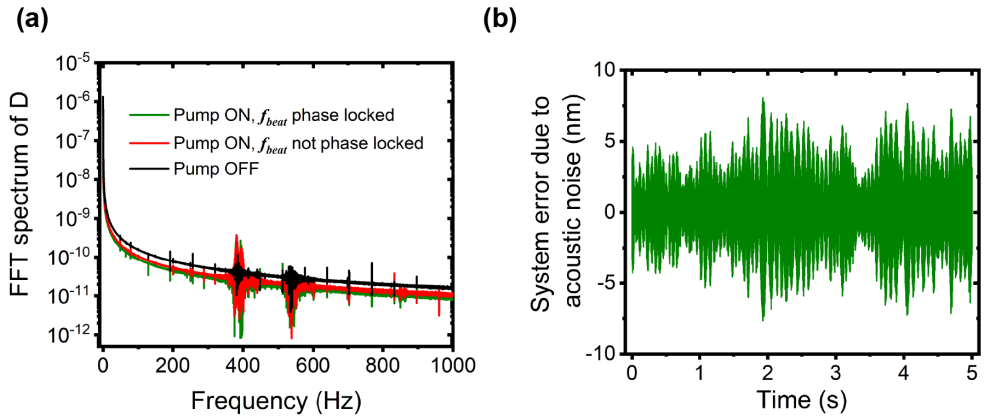

Fig. 4-6 (a): The FFT spectrum of measured distance. Green curve: the multi-mode pump is turned on and the two-color EO comb is coherently synthesized. Red curve: the multi-mode pump is turned on, but the two-color EO comb is not coherently synthesized. Black curve: the multi-mode pump is turned off. (b) The system error due to acoustic noise is around ± 5 nm.

4.2.3 Short-term stability and long-term stability

In absolute distance measurement based on cascaded measurements, it's necessary and significant to resolve the integer of precise measurement through coarse measurement. Generally speaking, the standard deviation of coarse measurement should be smaller than the non-ambiguity range of precise measurement. In this case, 68 % of coarse measurement data is valid to resolve the integer of precise measurement. To estimate the capability of realizing absolute distance measurement, investigations of short-term and long-term stability of both precise measurement and coarse measurement are required. Allan deviation (ADEV) is an excellent tool for the evaluations.

In the aforementioned system, D_p measurement is precise measurement and the D_g measurement is coarse measurement. For the evaluation of short-term stability, the fluctuations of D_p and D_g within 5 s are shown in Fig. 4-7 (a). The update rate is 10 kHz. The D_p and D_g have same drifting tendency. It is distinguishable that there are small modulations in measured D_p, which are due to the acoustic noise. The ADEV of D_p and D_g are given in Fig. 4-7 (b). The ADEV of D_p reaches the minimum value in 3 ms averaging time, which is 0.5 nm. The bump at shorter averaging time is attributed to the system acoustic noise. The increasing of ADEV at longer averaging time is due to environmental drifting. As for the D_g, the ADEV gradually decrease and then increases with the averaging time.

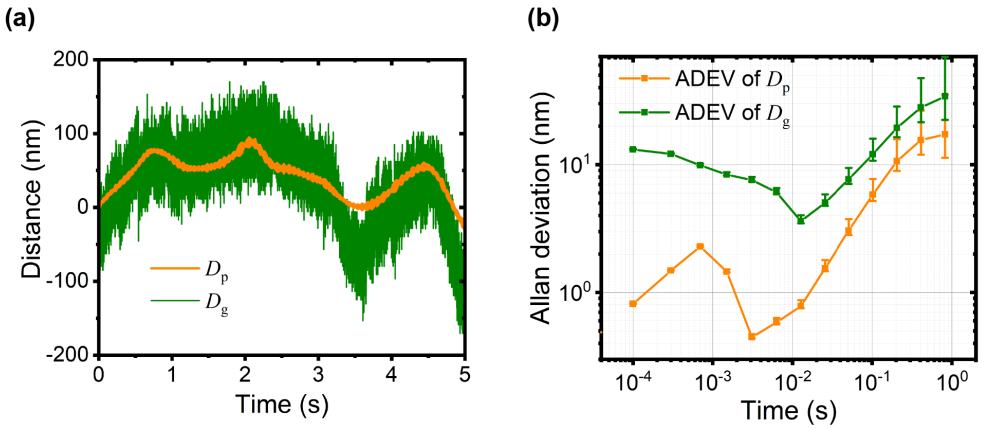

Fig. 4-7 Short-term stability of D_p and D_g. (a): Original data. (b): ADEV of D_p and D_g.

To investigate the long-term stability, the update rate is set to 100 Hz. The fluctuations and ADEV of D_p and D_g within 40 min are shown in Fig. 4-8. The ADEV of D_p and D_g are both increasing with averaging time, indicating the random drift due to environmental condition. It's worth to note that the ADEVs in Fig. 4-7 (b) and Fig. 4-8 (b) match with each other from 10 ms to 1 s averaging time. This indicates the reliability of the experimental results.

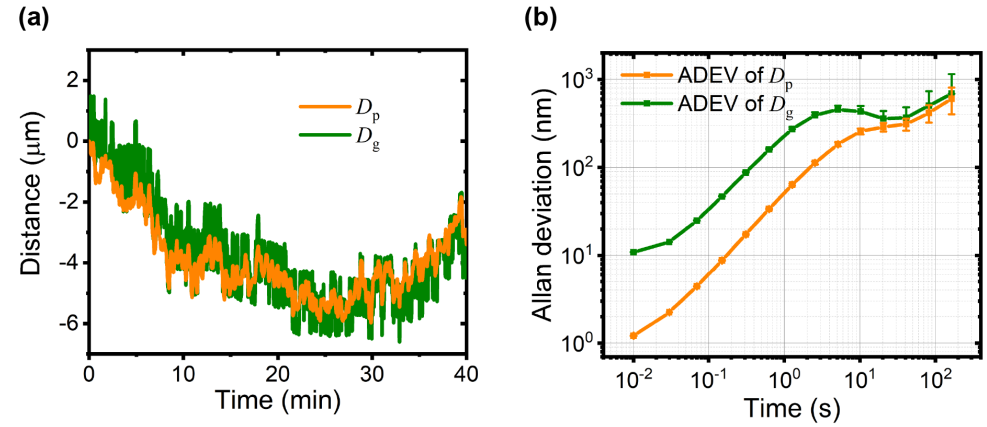

Fig. 4-8 Long-term stability of D_p and D_g. (a): Original data. (b) ADEV of D_p and D_g.

According to Fig. 4-7 (b) and Fig. 4-8 (b), the ADEV of D_g is well below the NAR of D_p. Therefore, absolute distance measurement is feasible in this system.

4.2.4 Linearity

In distance measurement based on phase detection, the cyclic error is a major problem that impacts the system linearity. Cyclic error is a phenomenon that the phase

of the signal to be measured is affected by a weak crosstalk signal [7]. Cyclic error exhibits periodic characteristics. There are many possible reasons that may induce cyclic error. For example, the polarization cross coupling between two laser beams will cause optical-crosstalk-induced cyclic error. Finite polarization extinction ratio of a polarization beam splitter may result in such optical crosstalk. This cyclic error that induced by polarization cross coupling can be minimized by polarization compensation [8] and careful polarization management [9]. Besides, some active methods are demonstrated to reduce the cyclic error, like applying some algorithms [10][11], applying phase modulation to the laser sources [12], adding another path to detect the heterodyne signal [13], spatial separating the laser beams [14][15], etc. Besides, a weak pseudo-reflection may be detected, resulting an optical crosstalk. In addition, electromagnetic contamination or electrical leakage leads to electrical-crosstalk-induced cyclic error. In one specific system, cyclic errors that induced by optical crosstalk and electrical crosstalk may exist simultaneously. In the aforementioned distance measurement system, the precise measurement is realized by detecting the phase of one heterodyne signal, while the coarse measurement is realized by detecting the phase difference between the two heterodyne signals. Therefore, the linearities of both precise and coarse measurement are affected by cyclic error. In this section, the impacts of cyclic error on precise measurement and coarse measurement are numerically simulated at first. Then the linearity of the system is analyzed through experiment.

Cyclic error of D_p. When assuming the AOFS is single passed, the heterodyne signal could be represented by $\overrightarrow{V_{w/o}}(t) = A_{w/o} \times \sin\left(2\pi f_m t + \varphi_{w/o}\right)$ in the ideal case, where $A_{w/o}$ is the amplitude of the heterodyne signal, f_m is the modulation of AOFS, $\varphi_{w/o} = 4\pi nD/\lambda$ is its phase, D is the distance under test, λ is the optical wavelength, n is air refractive index. A vector in a phasor diagram, as shown in Fig. 4-9 (a), can be used to describe the heterodyne signal. The length of the vector corresponds to the amplitude of the heterodyne signal, while the angle between the vector and the horizontal axis corresponds to the phase of the heterodyne signal. In ideal case, when the distance under test changes, the vector rotates along the starting point. The trajectory of the vector endpoint is a circle.

However, in practice, weak crosstalk signals may be detected by the photodetectors along with the heterodyne signal. The crosstalk signal could be represented by $\overrightarrow{V_{crosstalk}}(t) = A_{crosstalk} \times \sin\left(2\pi f_m t + \varphi_{crosstalk}\right)$, where

$A_{crosstalk}$ is its amplitude and $\varphi_{crosstalk}$ is its phase. For the sake of simplicity, the phase of crosstalk signal is considered as a constant. Therefore, this crosstalk is irrelevant to the heterodyne signal, as the black vector shown in Fig. 4-9 (b). The signal detected by PD becomes $\overrightarrow{V_{with}}(t) = \overrightarrow{V_{w/o}}(t) + \overrightarrow{V_{crosstalk}}(t)$, as the red vector in Fig. 4-9 (b). As a result, the phase of the detected signal deviates from ideal case due to the crosstalk. This deviation is periodical and therefore causes cyclic error.

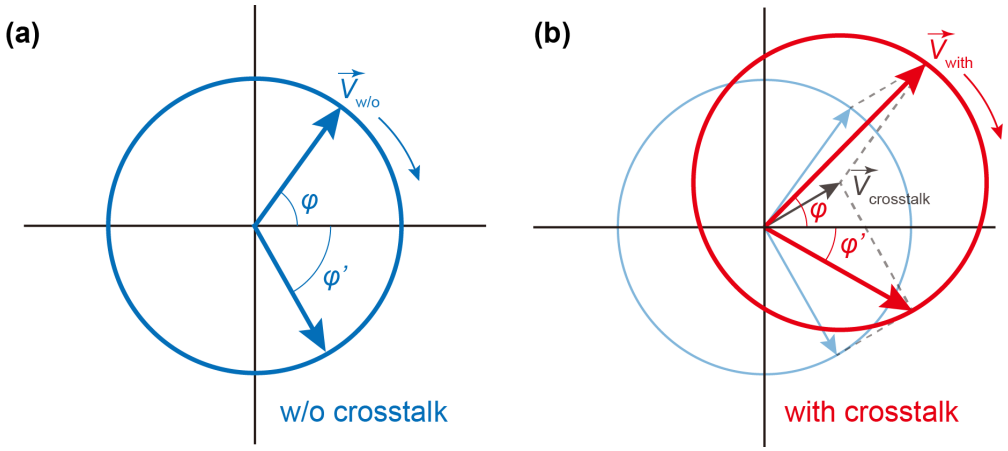

Fig. 4-9 Phasor diagram. (a): without crosstalk; (b): with crosstalk. $\overrightarrow{V_{w/o}}$, $\overrightarrow{V_{crosstalk}}$ and $\overrightarrow{V_{with}}$ correspond to the heterodyne signal without crosstalk, the crosstalk, and the heterodyne signal with crosstalk, respectively.

A simulation of the impact of cyclic error is firstly implemented. In the simulation, the power of the crosstalk is 0 dB ~ 70 dB lower than the heterodyne signal. The distance under test increases linearly. The phase of $\overrightarrow{V_{w/o}}(t)$ and $\overrightarrow{V_{with}}(t)$ are retrieved by IQ demodulation and unwrapped. Fig. 4-10 (a) shows the retrieved phase with and without the crosstalk, where the power of the crosstalk is equal to the power of heterodyne signal. The retrieved phase increases periodically by the impact of crosstalk, leading to the degradation of the linearity. The residuals between the retrieved phase of $\overrightarrow{V_{w/o}}(t)$ and $\overrightarrow{V_{with}}(t)$ with different intensity of crosstalk are shown in Fig. 4-10 (b), which indicates the cyclic error. The higher crosstalk, the severer residual. The period of the residuals equals to the period of $mod(\varphi_{w/o}, 2\pi)$. Although the cyclic error is given in the unit of rad in Fig. 4-10 (b), the distance measurement error can be easily obtained through $\Delta D = \varphi_{residual} \times \lambda/(4\pi n)$, where $\varphi_{residual}$ is the residual phase, λ is the optical wavelength and n is air refractive index. The Fourier transform spectra of the residuals in Fig. 4-10 (b) are shown in Fig. 4-10 (c). The fundamental harmonics are zoomed in. The relationship between the

amplitude of fundamental harmonics and the power of crosstalk is shown in Fig. 4-10 (d), which exhibits exponential decay with respect to the power ratio between the crosstalk and heterodyne signal. Besides fundamental harmonic, high order harmonics occur when the power of the crosstalk becomes comparable to the heterodyne signal. The residual phase severely distorts from sine waves consequently. From this simulation, it's better to ensure that the power of the crosstalk is at least 40 dB lower than the heterodyne signal.

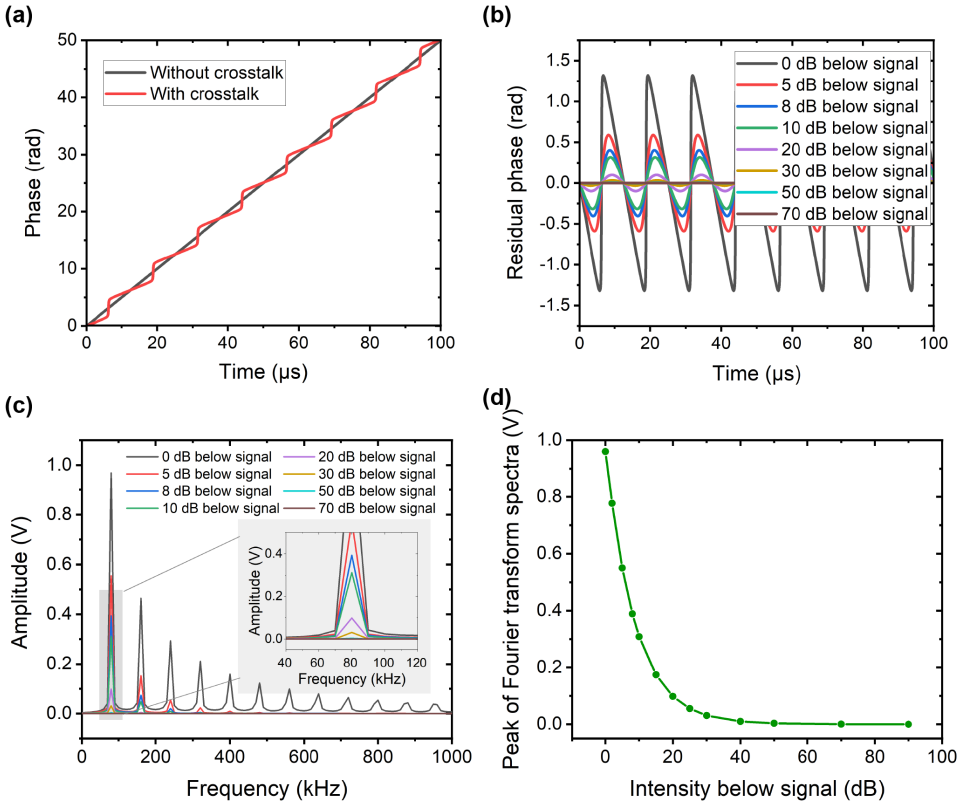

Fig. 4-10 (a) Retrieved phase from $\overrightarrow{V_{w/o}}(t)$ and $\overrightarrow{V_{with}}(t)$. The power of the crosstalk and the heterodyne signal is the same. (b) Residual phase with different intensity of crosstalk. (c) Fourier transform spectra of the residual phase in Fig. 4-10 (b). Inset: zoom-in of the fundamental harmonic. (d) Amplitudes of the fundamental harmonics in Fig. 4-10 (c) with respect to the power ratio between the crosstalk and heterodyne signal.

Cyclic error of D_g. In the above system, D_g measurement is obtained through synthetic wavelength technique. Its phase is measured by subtracting the phase of the two heterodyne signals. Therefore, any crosstalk that accompanied with the two heterodyne signals causes the cyclic error of D_g. Since the optical fields that contribute to the two heterodyne signals are in common path, it's reasonable to

assume that the crosstalk of the two heterodyne signals is the same. Suppose the power of the crosstalk is 10 dB lower than heterodyne signals and the under-test distance increases linearly, the retrieved phases of the coarse measurement with and without crosstalk are shown in Fig. 4-11 (a). The residual between these two curves is the cyclic error, as displayed in Fig. 4-11 (b). The envelope of the cyclic error has a period that same as the period of $mod((\varphi_1 - \varphi_2), 2\pi)$, where $\varphi_1 = 4\pi nD/\lambda_1$ and $\varphi_2 = 4\pi nD/\lambda_2$ are the phase of the two heterodyne signals, λ_1 and λ_2 are the optical wavelengths of the comb modes that contributes to the two heterodyne signals, D is the under-test distance and n is air refractive index. Comparing to the green curve in Fig. 4-10 (b), the amplitude of the cyclic error of residual phase of D_g is two times larger. D_g measurement error induced by the cyclic error can be obtained from the residual phase and synthetic wavelength by $\Delta D_g = \varphi_{residual} \times \Lambda/(4\pi n)$, where $\varphi_{residual}$ is the residual phase, Λ is the synthetic wavelength and n is air refractive index. As a result, the cyclic error of the precise measurement is magnified by a factor of $2 \times \Lambda/\lambda$ in the coarse measurement. Since the coarse measurement gives the information of the integer of precise measurement, it is very important to reduce the cyclic error in order to resolve the integer of precise measurement without mistake, especially in dynamic measurement. Note that the envelope of the cyclic error is not a clean sine curve. This varies under different power of crosstalk, since high order harmonics may occur.

From another point of view, the cyclic error of D_g measurment can be regarded as the result of the beat between the two crosstalk signals that accompanied with the two heterodyne signals. Since the cyclic errors of the two heterodyne signals have slightly different period, their period difference determines the period of coarse measurement's cyclic error.

It is worth to emphasis that the magnification of the cyclic error from precise measurement to coarse measurement has an important prerequisite: the coarse measurement is implemented according to the results of the precise measurement. For example, the coarse measurement and the precise measurement in Fig. 4-1 are both realized by measuring the phase of heterodyne signals. If the coarse measurement and the precise measurement are obtained from totally different signals and measurements , there is no magnification of the cyclic error.

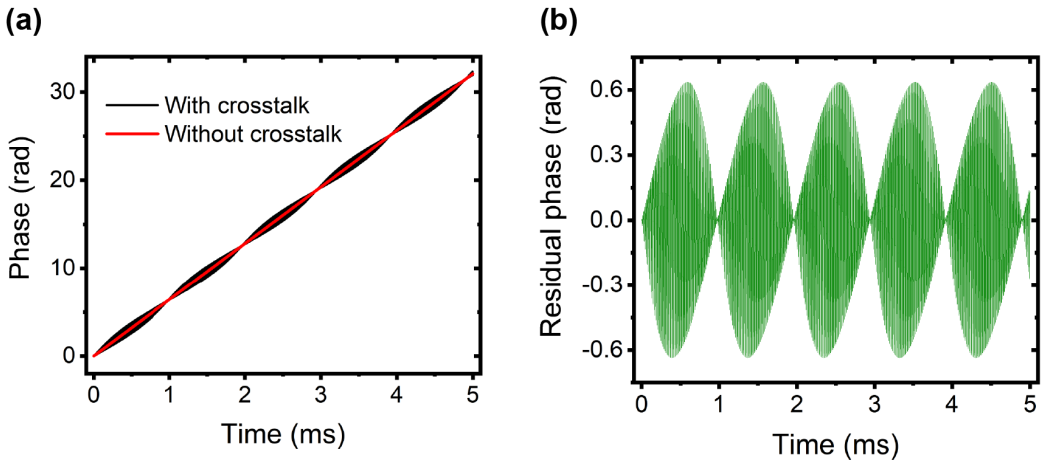

Fig. 4-11 Simulation of cyclic error of D_g. (a) Retrieved phase of coarse measurement with and without crosstalk. The power of the crosstalk is 10 dB lower than the power of the heterodyne signal. (b) Residual phase.

The linearity of D_p and D_g measurement is investigated in experiment separately.

Linearity of D_p. By controlling the motorized stage, the target mirror is moved with a displacement of 180 μm at 20 μm/s speed. The measured D_p from unwrapped phase is shown as the red curve in Fig. 4-12 (a). The linear fit of D_p is also displayed as the black curve, which is shifted downward for clarity. The residual between the measured D_p and its linear fit is within $\pm$ 200 nm in the 9-s measurement time, as the green curve in Fig. 4-12 (a). There are two main reasons for the residual: a) the slow drifting of the dead path due to environmental instability; b) the nonlinear moving of the motorized stage. The slow drifting of the dead path can be confirmed from Fig. 4-4. The Allan deviation of D_p is several hundreds of nm at 10-s averaging time, which agrees with the amount of residual. As for the nonlinearity of the motorized stage, one can subtract the nonlinearity by comparing the measurement results with that from a reference interferometer.

The FFT spectrum of the residual is shown in Fig. 4-12 (b). From the FFT spectrum, one can clearly recognize the acoustic noise and some resonance frequencies of the stage. These resonance frequencies, which are integer multiples of 20 Hz, are attributed to the alternating current (AC) servo of the stage. It's worth to note that the resonance frequencies vary with the moving speed of the target mirror.

According to the above simulation, the period of cyclic error is related to the

moving speed of the target mirror. Assume the moving speed of the target mirror is v and the optical wavelength is λ, the fundamental frequency of cyclic error is $f = 2v/\lambda$. As a result, the cyclic error should have a frequency of $f = 2v/\lambda = 2 \times 20/1.56\,Hz \approx 25.64\,Hz$ when the target mirror moves at a speed of 20 μm/s. This cyclic error is emphasized by a red arrow in the inset of Fig. 4-12 (b), which shows well agreement with expected value. By digitally bandpass filtering the residual of D_p, only the influence of cyclic error is remained, as illustrated in Fig. 4-12 (c). The cyclic error of D_p is within $\pm$ 1 nm, which is much smaller than the acoustic noise and the resonance of the stage.

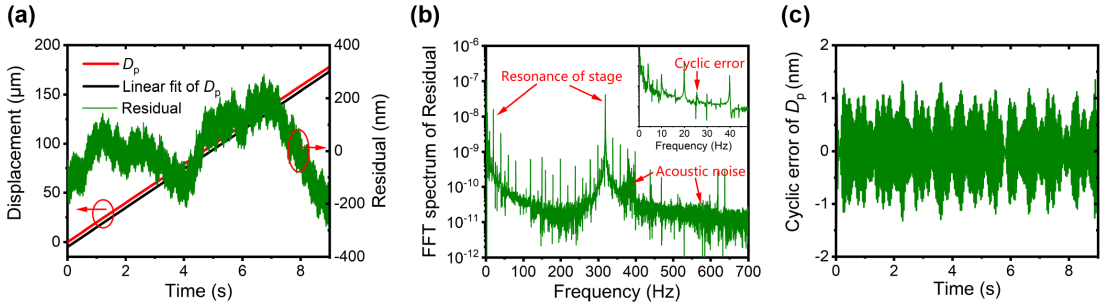

Fig. 4-12 (a) Linearity of D_p. Red curve: experimentally measured D_p. Black curve: linear fit of D_p, which is downward shifted for clarity. Green curve: the residual between the measured D_p and its linear fit, which corresponds to the right axis. (b) FFT spectrum of the residual. Inset: zoom in of the FFT spectrum. (c) Cyclic error of D_p.

Linearity of D_g. The measured D_g when target mirror moves 180 μm with 20-μm/s speed is shown in Fig. 4-13 (a). The displacement is three times of the 60-μm non-ambiguity range. The linear fit of D_g is plotted as the black curve, which is also downward shifted for clarity. The residual between the measured D_g and its linear fit is plotted as the green curve in Fig. 4-13 (a). There is some periodical structure in the residual. The possible reasons of these contain the nonlinearity of the lock-in-amplifier, etc. Through subtracting these periods with their fit curves, the integer of the precise D_p measurement can be retrieved without aliasing. The FFT spectrum of the residual is shown in Fig. 4-13 (b). From the FFT spectrum, one can recognize the resonance frequencies that induced by the motorized stage and the cyclic error. The frequency of cyclic error is around 25 Hz. Then a digital bandpass filter is utilized to filter out the cyclic error. The result is shown in Fig. 4-13 (c). This cyclic error exhibits similar shape with the simulation in Fig. 4-11 (b). Considering

the 0.5-nm cyclic error of D_p in Fig. 4-12 (c) and the magnification factor of 2×120/1.56, the cyclic error of D_g should be around 77 nm theoretically. The amplitude of the cyclic error is ~55 nm, which agrees well with theoretical value.

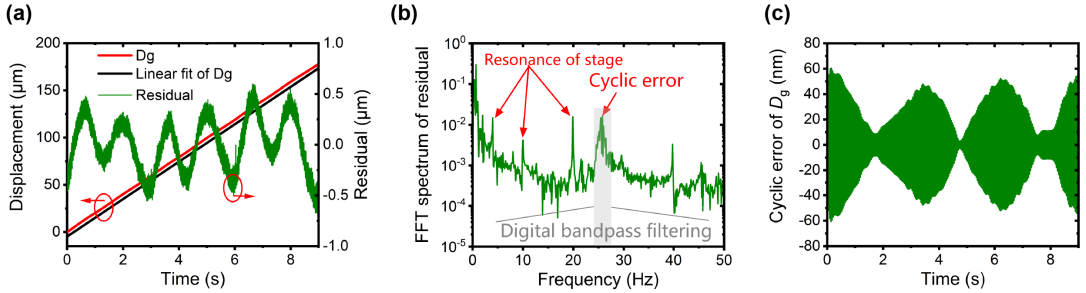

Fig. 4-13 (a) Linearity of D_g. Red curve: experimentally measured D_g. Black curve: linear fit of D_g, which is downward shifted for clarity. Green curve: the residual between the measured D_g and its linear fit, which corresponds to the right axis. (b) Cyclic error of D_g.

4.3 Absolute distance measurement

In this section, absolute distance measurement with extended non-ambiguity range is achieved by combining the precise measurement and coarse measurement. The integer of the precise measurement is decided by coarse measurement. As a result, the absolute distance measurement has the advantage of wider non-ambiguity range and high precision. The measurement results are compared with that from a commercial HeNe interferometer, as illustrated in Fig. 4-1. The target paths of the HeNe interferometer and the fiber interferometer are collinear and in opposite direction, aiming to minimize the cosine error and sine error. The measurement results show high linearity between HeNe interferometer and the fiber interferometer with a correlation factor of R^2 = 0.99999, as shown in Fig. 4-14. The residual difference between the two measurements is less than 200 nm with a 93 nm standard deviation. The residual difference may be due to the environmental instability during the 3-s measurement time.

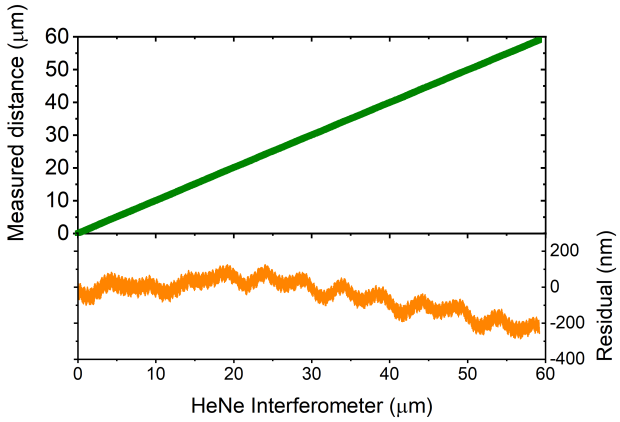

Fig. 4-14 Experimental results of the absolute distance measurement compared with a commercial HeNe laser interferometer.

4.4 Fast displacement measurement

According to the above analysis, it is found that the slow drifting of the dead path is problematic for long-term measurement. The precision and accuracy of the measurement is hard to be guaranteed in long-term measurement. However, this is no longer an issue in fast displacement measurement. In other words, this system is especially suitable for fast displacement measurement.

The experimental setup for fast displacement measurement is illustrated in Fig. 4-15. A PZT (Thorlabs, PC4QR) is bonded on the fiber in the target path, which is driven by an external signal. The measurement method of D_p and D_g is same as above. Of course, it's possible to experimentally verify fast measurement by rapidly moving the target mirror, which could be mounted on a PZT. Here a PZT bonded on the fiber is applied because of smaller load mass.

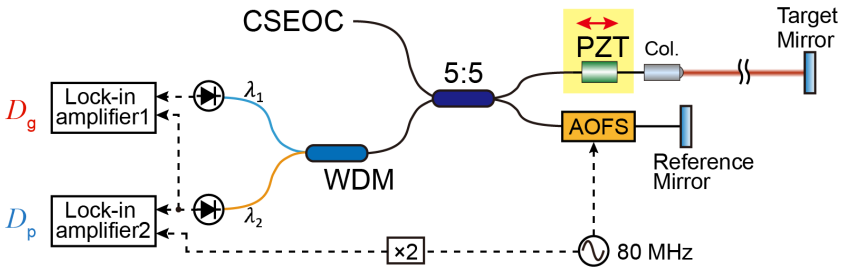

Fig. 4-15 Experimental setup for fast displacement measurement.

When the PZT is driven by a sinusoidal signal with frequency varies from 10 Hz to 500 Hz, the measurement results are shown in Fig. 4-16. The amplitude of the driven signal is 1.875 V. The update rate of the measurement is 10 kHz, which is

limited by the integration time of the lock-in-amplifier. The measured displacement is displayed as orange dots, while the sine fit is plotted as the blue curve. The amplitude of the length vibration induced by the PZT is ~100 nm. This indicates that this system is capable of capturing fast and weak vibrations. The residual between the measured data and its sine fit is shown as the gray dots. The residuals exhibit periodic structure, which is due to the aforementioned acoustic noise. The standard deviations of these residuals gradually increase from 3.44 nm to 3.96 nm with the modulation frequency. This could be attributed to the reduced samples in each period.

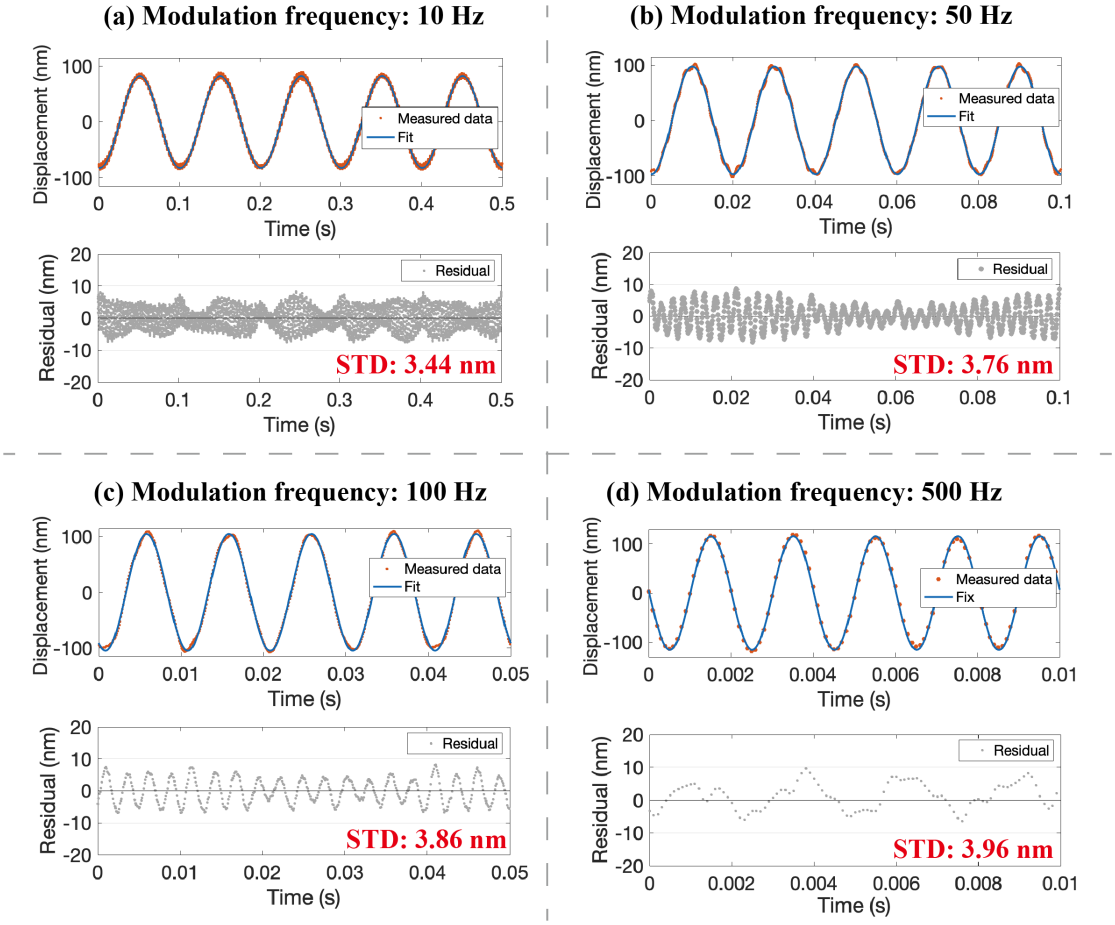

Fig. 4-16 Fast displacement measurement at different modulation frequencies of PZT. The measured displacement (orange dots), the fit curve of the measured data (blue curve) and the residual (gray dots) are displayed. (a): 10 Hz. (b): 50 Hz. (c): 100 Hz. (d):500 Hz.

Then the modulation frequency is increased to 1 kHz. The measurement results are shown in Fig. 4-17, including the measured data, the sine fit and the residual. The standard deviation of the residual is 4.88 nm. This value is larger than those in Fig. 4-16, since there are only 10 samples in each period. Reduction of the residual could

be realized by improving the update rate through detecting the phase of heterodyne signal with FPGA.

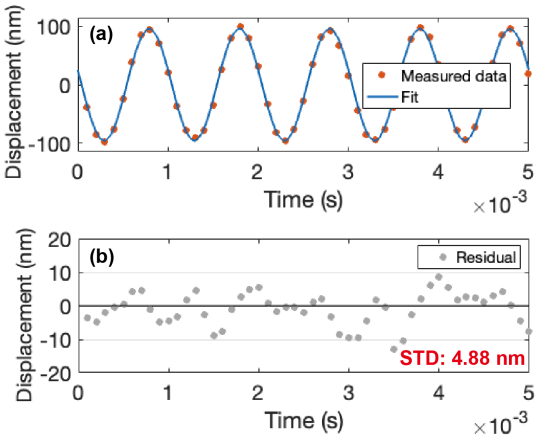

Fig. 4-17 Fast displacement measurement. The modulation frequency of PZT is 1 kHz. (a): Measured displacement (orange dots) and the fit curve (blue curve); (b): Residuals between the measured data and fit.

4.5 Summary of this chapter

In this chapter, a distance measurement system is constructed on the basic of the coherently synthesized two-color EO comb. This distance measurement system contains a fiber-type Michelson interferometer. Both single wavelength interferometry and synthetic wavelength technique are employed in the system. Therefore, high precision measurement in extended range is achieved. The system performance is systematically evaluated, including the dead path error, acoustic noise, short-term stability, long-term stability, cyclic error and linearity.

The proof-of-principle experiments are implemented, including absolute distance measurement and fast displacement measurement. In absolute distance measurement, the measurement results are compared with the results from a commercial HeNe interferometer, indicating well consistency. The non-ambiguity range is extended to 60 μm by combining synthetic wavelength technique and single wavelength interferometry. In the fast displacement measurement, the path length vibration at 1 kHz with 100-nm amplitude is recognizable.

These proof-of-principle experiments indicates that the coherently synthesized two-color EO comb is well suitable to distance measurements, attributing to the high comb mode power, low phase noise, simple configuration, turnkey operation and so on.

4.6 References

[1] G. Wu, M. Takahashi, K. Arai, H. Inaba, K. Minoshima. Extremely high-accuracy correction of air refractive index using two-colour optical frequency combs[J]. Scientific Reports, 2013, 3(1): 1-6.

[2] K. Minoshima, K. Arai, H. Inaba. High-accuracy self-correction of refractive index of air using two-color interferometry of optical frequency combs[J]. Optics Express, 2011, 19(27): 26095-26105.

[3] T. Tanaka, K. Akuzawa, T. Kato, and K. Minoshima. Shape Measurement Technique with Self-correction of Air Refractive Using a Single-color Comb Interferometer[C]//Conference on Lasers and Electro-Optics/Pacific Rim. Optica Publishing Group, 2022: CThA6D_03.

[4] R. E. Bartolo, A. B. Tveten, A. Dandridge. Thermal phase noise measurements in optical fiber interferometers[J]. IEEE Journal of Quantum Electronics, 2012, 48(5): 720-727.

[5] https://www.corning.com/media/worldwide/coc/documents/Fiber/product-information-sheets/PI1463_07-14_English.pdf

[6] C. E. Lee, J. J. Alcoz, Y. Yeh, W. N. Gibler, R. A. Atkins, and H. F. Taylor. Optical fiber Fabry-Perot sensors for smart structures[J]. Smart Materials and Structures, 1992, 1(2): 123.

[7] C. Wu and C. Su. Nonlinearity in measurements of length by optical interferometry. Measurement Science and Technology, 1996, 7(1), 62.

[8] O. P. Lay and S. Dubovitsky. Polarization compensation: a passive approach to a reducing heterodyne interferometer nonlinearity. Optics Letters, 2002, 27(10), 797.

[9] T. G. McRae, M. T. L. Hsu, C. H. Freund, D. A. Shaddock, J. Herrmann, and M. B. Gray. Linearization and minimization of cyclic error with heterodyne laser interferometry. Optics letters, 2012, 37(13), 2448.

[10] P. Hu, J. Zhu, X. Guo, and J. Tan, Compensation for the variable cyclic error in homodyne laser interferometers. Sensors, 2015, 15(2), 3090.

[11] T. B. Eom, T. Y. Choi, K. H. Lee, H. S. Choi, and S. K. Lee. A simple method for the compensation of the nonlinearity in the heterodyne interferometer. Measurement Science and Technology, 2002, 13(2), 222.

[12] S. Dubovitsky. Heterodyne interferometer with phase-modulated carrier. NASA Tech. Briefs, 2001, 25(2).

[13] W. Hou and G. Wilkening. Investigation and compensation of the nonlinearity of heterodyne interferometers. Precision engineering, 1992, 14(2), 91.

[14] S. Yokoyama, Y. Hori, T. Yokoyama, and A. Hirai. A heterodyne interferometer constructed in an integrated optics and its metrological evaluation of a

picometre-order periodic error. Precision Engineering, 2018, 54, 206.
[15] K. N. Joo, E. Clark, Y. Zhang, J. D. Ellis, and F. Guzmán. A compact high-precision periodic-error-free heterodyne interferometer. Journal of the Optical Society of America A, 2020, 37(9), B11.

Chapter 5. Absolute distance measurement based on free space interferometer and coherently synthesized two-color EO comb

It is found that the fiber length fluctuation degrades the precision of measured distance in the system demonstrated in Chapter 4. To solve this problem, two distance measurement systems based on free space interferometer are constructed in this chapter. The long-term stability is greatly improved compared to that of the system in Chapter 4. The main difference between the two free-space distance measurement system is the presence or absence of a monitor arm. Through experimental results, it is found that the length fluctuation of the frequency shifter and air flow can be partially compensated by introducing the monitor arm. Moreover, distance measurement through microwave phase detection is enabled. The non-ambiguity range is extended to 15 mm consequently. Through comparing the measurement results with a HeNe interferometer, deviation less than ± 25 nm is realized.

5.1 Absolute distance measurement without monitor arm

5.1.1 Experimental setup

The experimental configuration is displayed in Fig. 5-1. The CSEOC is from the 30% output of the EDFA as illustrated in Fig. 3-29. A piece of 560-m SMF is used to compress the pulse to 2 ps before directing to free space. Two waveplates and a polarizing beam splitter are used to polarize the laser beam. The distance measurement system is based on an asymmetric Michelson interferometer with a reference arm and a target arm. An acousto-optic frequency shifter (AOFS, Gooch & Housego, 3165-1) with 165 MHz center frequency is inserted in the reference arm. A 165-MHz sinusoidal signal from a RF oscillator that amplified to 36 dBm is used to drive the AOFS. The 1st order diffraction beam from the AOFS is reflected by reference mirrors and combined with the beam from target arm. The reference mirrors are fixed while the target mirrors are installed on a motorized stage (Suruga Seiki, KS102-100-2). The path length difference between reference arm and target arm is preset to be 0.42 m, corresponding to 14 times the pulse separation (0.03 m). Hence

the pulses from the two paths are overlapped in time domain when they are detected. After passing through two bandpass filters with 1540 nm and 1560 nm center wavelengths, two heterodyne signals are detected by two low noise photo detectors (Newport 1611). Two lock-in amplifiers (Stanford Research Systems, SR844) are used to detect the phase of the heterodyne signals. The reference signals of the lock-in amplifiers and the driven signal of the AOFS come from the same RF oscillator. As a result, two optical distances, D_{p1} and D_{p2}, that follow the phase refractive index of the air at 1540 nm and 1560 nm, could be calculated from the detected phase φ through $D_p = \varphi\lambda/4\pi n$, where n is phase refractive index of air, λ are 1540 nm and 1560 nm for D_{p1} and D_{p2}, respectively.

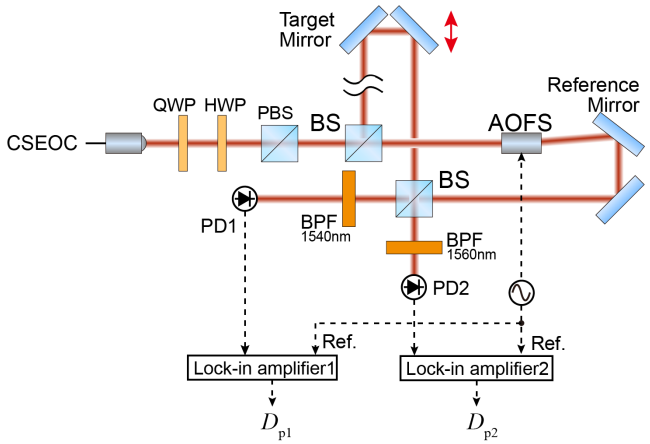

Fig. 5-1 Experimental configuration. CSEOC: coherently synthesized two-color EO comb; QWP: quarter wave plate; HWP: half-wave plate; PBS: polarizing beam splitter; BS: beam splitter; BPF: band pass filter; AOFS: acoustic-optic frequency shifter; PD: photo detector.

5.1.2 Measurement results of D_{p1} and D_{p2}

The measurement results of D_{p1} and D_{p2} are shown in Fig. 5-2. The whole system is warmed up for 7 hours. Fig. 5-2 (a) shows the fluctuation of D_{p1} and D_{p2} within 30 min when the target mirror stays still. D_{p1} and D_{p2} drift ~200 nm within 30 min due to environmental instability. This drift is due to the thermal effect of the heated AOFS and the consequently heated air.

Benefiting to the coherently synthesized two-color EO comb, D_{p1} and D_{p2} have the same drifting tendency. The difference between D_{p1} and D_{p2} is within ±5 nm, as the orange curve in Fig. 5-2 (a), indicating the high synchronization between D_{p1} and D_{p2}. The standard deviation of D_{p1} and D_{p2} are 53.91 nm and 56.53 nm,

corresponding to 0.128 ppm and 0.134 ppm for 0.42-m distance, respectively. The Allan deviations of D_{p1} and D_{p2} increase with averaging time, as plotted in Fig. 5-2 (b). At 1 s averaging time, the Allan deviation is around 20 nm. The Allan deviation of $D_{p1} - D_{p2}$ is shown as orange curve in Fig. 5-2 (b), which is 1 nm at 1 s averaging time.

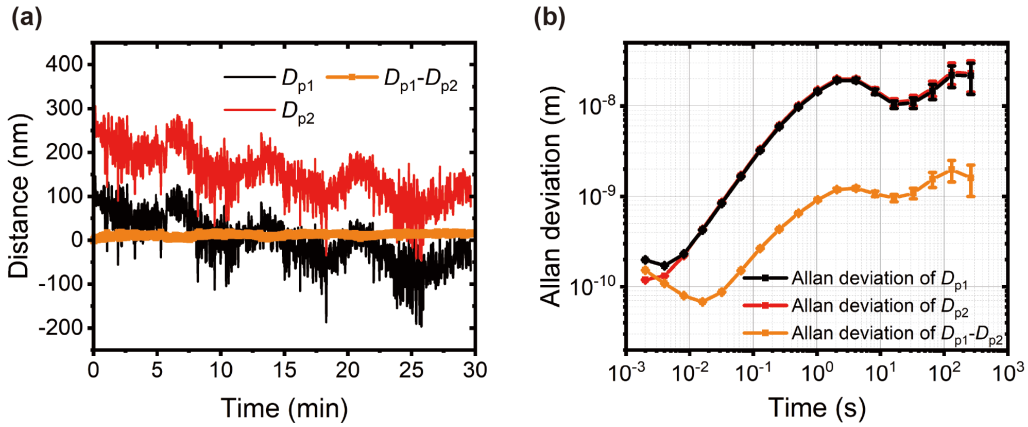

Fig. 5-2 Measurement results of D_{p1} and D_{p2}. (a): The fluctuation of D_{p1} (black curve) and D_{p2} (red curve) when the target mirrors stay still, D_{p2} is upward shifted for clarity. Orange curve: the difference between D_{p1} and D_{p2}. (b): Allan deviation of D_{p1}, D_{p2} and $D_{p1} - D_{p2}$ in Fig. 5-2 (a).

Fig. 5-3 shows the distance measurement results when moving the target mirror of 5 μm with 1 μm moving step. The steps are obviously distinguished. The standard deviation of D_{p1} at the third stop is 0.55 nm, as displayed in Fig. 5-3.

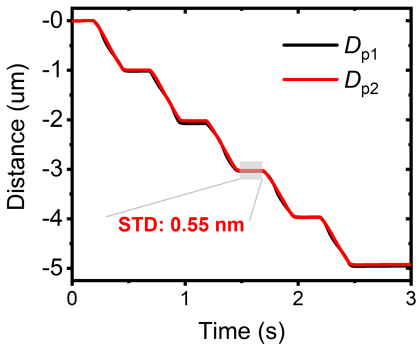

Fig. 5-3 Measured D_{p1} and D_{p2} when target mirror is moved 5 μm with 1μm step.

5.1.3 Cyclic error and its reduction

During the measurement, a small leakage signal of the driven signal to the AOFS

is detected by the photodetectors, with -44 dBm power. The frequency of the leakage signal is 165 MHz, same as the driven signal of AOFS. According to the analysis in Section 4.2.4, this leakage signal results in the crosstalk, hence the cyclic error. This electromagnetic-contamination-induced cyclic error is investigated in this section. Only D_{p1} is measured here.

The heterodyne signal is detected with -36 dBm power. So the power of crosstalk is 8 dB lower than that of the heterodyne signal. The detected signal is amplified to 0 dBm before inputted to the lock-in amplifier. The target mirrors are moved at a speed of 1.25 μm/s. Based on the simulation in Section 4.2.4, this will induce a cyclic error in phase measurement with 0.404-rad amplitude. Taken the center wavelength of 1540 nm into consideration, this corresponds to distance measurement error with 49.51-nm amplitude.

The lock-in-amplifier outputs the phase of the detected signal, as the green curve in Fig. 5-4 (a). The black curve and the red curve are the unwrapped phase and its linear fit, respectively. The residual between the unwrapped phase and its linear fit is plotted in Fig. 5-4 (b), which indicates a period of $mod(\varphi_{w/o}, 2\pi)$. The amplitude of the residual phase is around ± 0.4 rad, corresponding to ± 49 nm in distance, which is consistent with the simulation.

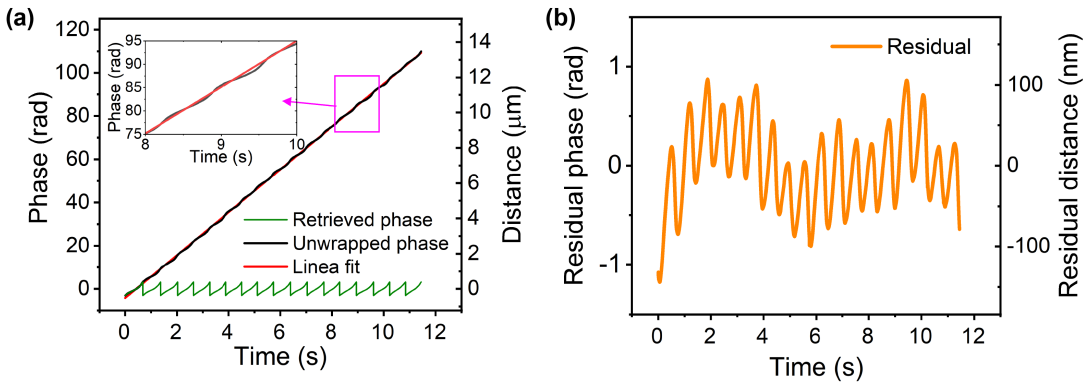

Fig. 5-4 (a) Green curve: measured phase of the detected heterodyne signal. Black curve: unwrap of the measured phase. Red curve: linear fit of the unwrapped phase. The right axis is distance calculated according to equation 2-10. Inset: zoom in. (b) Residual phase between the unwrapped phase and its linear fit. The right axis is the calculated residual distance.

Of course, it is possible to reduce the cyclic error by increasing the power of the heterodyne signal. But here, the cyclic error is reduced through better isolating the optical components from the electrical components. To achieve better isolation, the

electrical parts (including PD, AMP and the lock-in amplifier) are moved to the second room (labeled as Room2), as shown in Fig. 5-5 (a). The reference signal of the lock-in-amplifier is from a function generator that shares the same clock with AOFS's driver. A piece of 20-m single-mode-fiber is utilized to connect the optical parts and electrical parts. Since the pulse trains that reflected from the reference arm and target arm propagate in the 20-m fiber simultaneously, the influence of the fiber length fluctuation to the optical phase between the two pulse trains is common. This means the impact of fiber length fluctuation on distance measurement is negligible. In this case, no 165 MHz contamination signal is detected by PD. The power of the heterodyne signal is -36 dBm. The experimental results are shown in Fig. 5-5 (b) and (c). Compared with Fig. 5-4 (b), there is no clear period for the residual phase, indicating the reduction of the cyclic error. To some extent, the system become bulky in this case. This could be dealt by carefully enclosing the optical parts and electrical parts into metallic boxes and then connecting them with a piece of fiber.

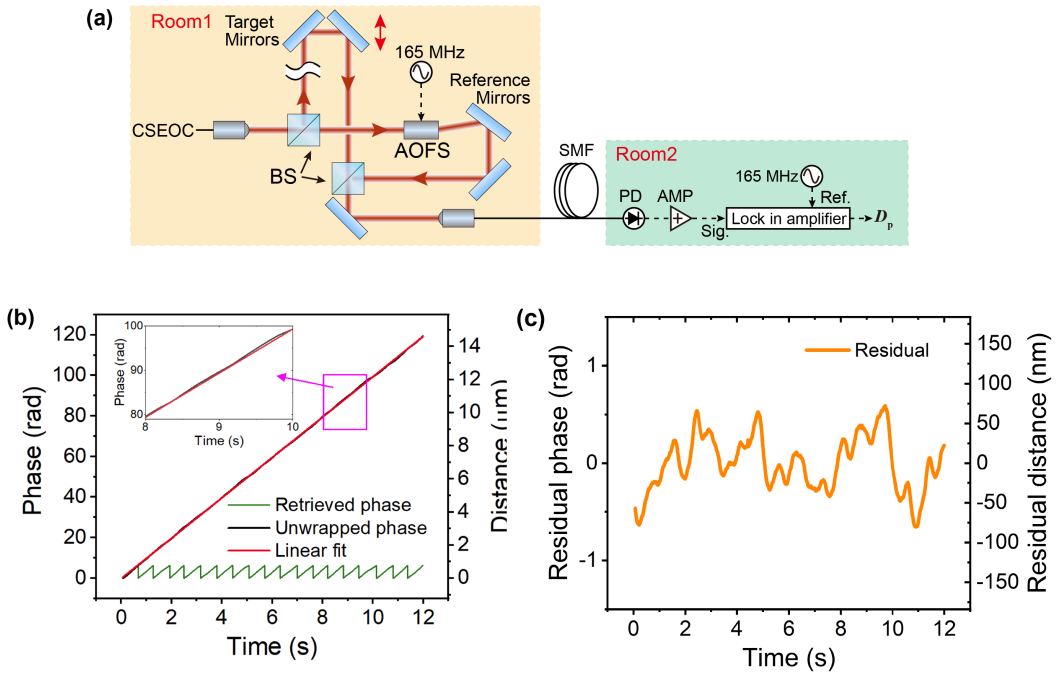

Fig. 5-5 (a) Experimental setup. The optical part and electrical part are separated into two rooms. A piece of 20-m SMF is used to connect the optical part and electrical part. (b) Green curve: measured phase of detected signal. Black curve: unwrap of the measured phase. Red curve: linear fit of the unwrapped phase. Inset: zoom in. The right axis is the calculated distance according to equation 2-10. (c) Residual phase between the unwrapped phase and its linear fit. The right axis is the calculated residual distance.

Beside isolating the optical part and electrical part very well, there are many other methods to reduce the cyclic error, depending on the causes of cyclic error. For example, one can set the frequency of the frequency shifter (f_m) larger than half repetition rate ($f_{rep}/2$) of the optical frequency comb [1]. In this case, the frequency of heterodyne signal is $mod(|f_{rep} - f_m|, f_{rep})$, which is different from the frequency of the shifter, preventing the electrical crosstalk due to electromagnetic contamination. In addition, the reference beam can be frequency shifted by two cascaded frequency shifters with distinct frequency. As a result, the frequency of the heterodyne signal is separate from the frequency of driven signals. Hence the electromagnetic contamination is avoided. To reduce optical crosstalk induced cyclic error such as polarization cross coupling, linearly polarized light is recommended. In fact, the waveplates and the PBS in Fig. 5-1 are used to polarize the light. Moreover, cube beam splitter and cube polarizing beam splitter should be avoided in the system, in order to prevent the pseudo-reflection from the surface of the cube beam splitter. Plate beam splitters with non-zero angle of incidence are recommended.

5.2 Absolute distance measurement with monitor arm

In this section, the system configuration is upgraded by introducing a monitor arm and applying microwave phase detection. The length fluctuation in the reference beam path that induced by the AOFS is compensated through measuring it. The NAR is further extended by the microwave phase detection method. Then, the system performances are investigated, including the short-term and long-term stability, linearity, etc.

5.2.1 Experimental setup

Basic configuration. The basic configuration of the distance measurement setup with monitor arm is shown in Fig. 5-6. The CSEOC is split into three parts, including the monitor beam, the reference beam and the probe beam. The path lengths of the monitor beam and the reference beam are fixed, while the path length of the probe beam is under test. The reference beam is frequency-shifted. Then, the monitor beam and the reference beam are recombined. Since there are two center wavelengths in the CSEOC, two heterodyne signals between the two beams are detected. One is contributed from the comb modes near λ_1. The other is contributed from the comb

modes near λ_2. Similarly, the probe beam is also combined with the reference beam. Hence, two heterodyne signals are detected.

By comparing the phase of the heterodyne signals that contributed from the comb modes near λ_1, single wavelength interferometry is implemented. The measurement result through this method is labeled as D_p. By comparing the phase of the two heterodyne signals that contributed from probe beam and reference beam, synthetic wavelength technique is implemented. The synthetic wavelength is 120 μm. The measurement result is labeled as D_g. Meanwhile, the repetition rate of the monitor beam and probe beam are detected. By subtracting the phase of f_{rep} signal, microwave phase detection is implemented. The wavelength of the microwave is 15 mm. The result is labeled as D_m. These three methods are applied to measure the same distance, from precise measurement to coarse measurement.

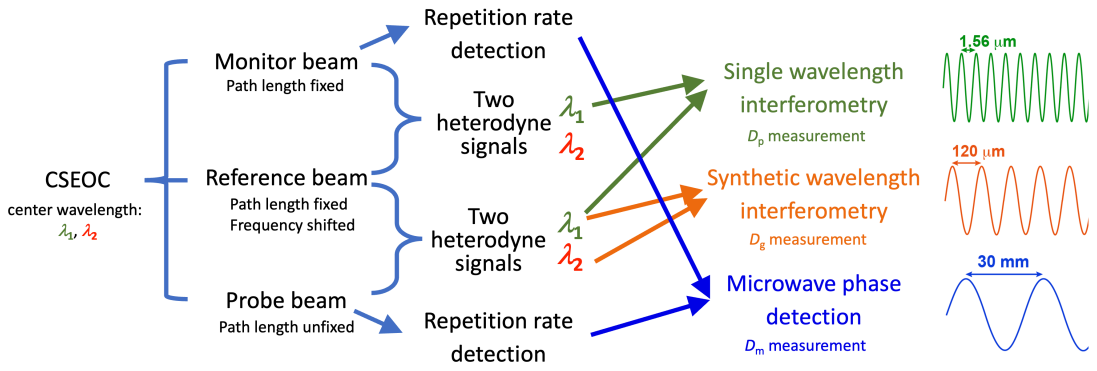

Fig. 5-6 The basic configuration of the distance measurement system with monitor arm. CSEOC: coherently synthesized two-color EO comb.

Experimental setup. The experimental scheme is shown in Fig. 5-7. First, two waveplates and a polarizing beam splitter (PBS) is used to polarize CSEOC for the reason that linear polarized beam is favored in distance measurement. The center wavelengths of CSEOC are 1540 nm and 1560 nm. Attributing to the non-polarization-maintain configuration of the EDFA, the comb modes located near 1540 nm and 1560 nm have different polarization. Therefore, the angle of the quarter waveplate and the half waveplate should be carefully adjusted in order to balance the transmitted power of these comb modes. In this setup, the optical power of the CSEOC for distance measurement is 33 mW, which is 30% of the power at the output of EDFA (see Fig. 3-16 and Fig. 3-29). The transmitted power after the PBS is 23 mW, including 12.65 mW for 1540-nm EO comb and 10.35 mW for 1560-nm EO comb.

The power ratio between the 1540-nm EO comb and the 1560-nm EO comb is 1.1:0.9. The reflected beam of the PBS is coupled into a piece of single-mode fiber (not shown in Fig. 5-7). A high-speed photo detector (Newport 1414) is used to detect the repetition rate, which will be discussed later.

Then the transmitted beam from the PBS is split into reference beam, monitor beam and probe beam through two beam splitters (BS1 and BS2). The reference beam is frequency-shifted for 165 MHz through an acousto-optic frequency shifter (AOFS, Gooch & Housego 3165-1). The single-passed AOFS is driven by a 165-MHz sinusoidal signal with 36 dBm power. The driven signal is reference to a 10 MHz GPS-disciplined clock. The diffraction efficiency of the AOFS is 50%. The reference beam is reflected by the fixed reference mirrors. The monitor beam is reflected by monitor mirror, which is mounted on a manual stage. After reflected by the monitor mirror, the monitor beam is combined with the reference beam at BS6. Two bandpass filters with center wavelengths of 1540 nm and 1560 nm (Thorlabs, FBH1540-12 and FBH1560-12) are placed at the transmission port and reflection port of BS6, respectively. Therefore, the comb modes located near 1540 nm and 1560 nm are separated. The path length difference between the monitor path and reference path is set to 10 times of the distance between adjacent pulses. This is easily realized by adjusting the position of the monitor mirror. Then two heterodyne signals are detected by two photodetectors (PD3 and PD5, Newport 1611), respectively.

The probe mirrors are mounted on a motorized stage (Suruga Seiki, KS102-100-2). After reflected by the probe mirrors, the probe beam combines with the reference beam at BS4. Therefore, two heterodyne signals at 1540 nm and 1560 nm are generated between the probe beam and reference beam. PD2 and PD4 (Newport, 1611) are used to detect the heterodyne signals, respectively. To summarize, four heterodyne signals are detected by four photodetectors separately, including a pair of heterodyne signals that contributed by comb modes near 1540 nm and a pair of heterodyne signals that contributed by comb modes near 1560 nm.

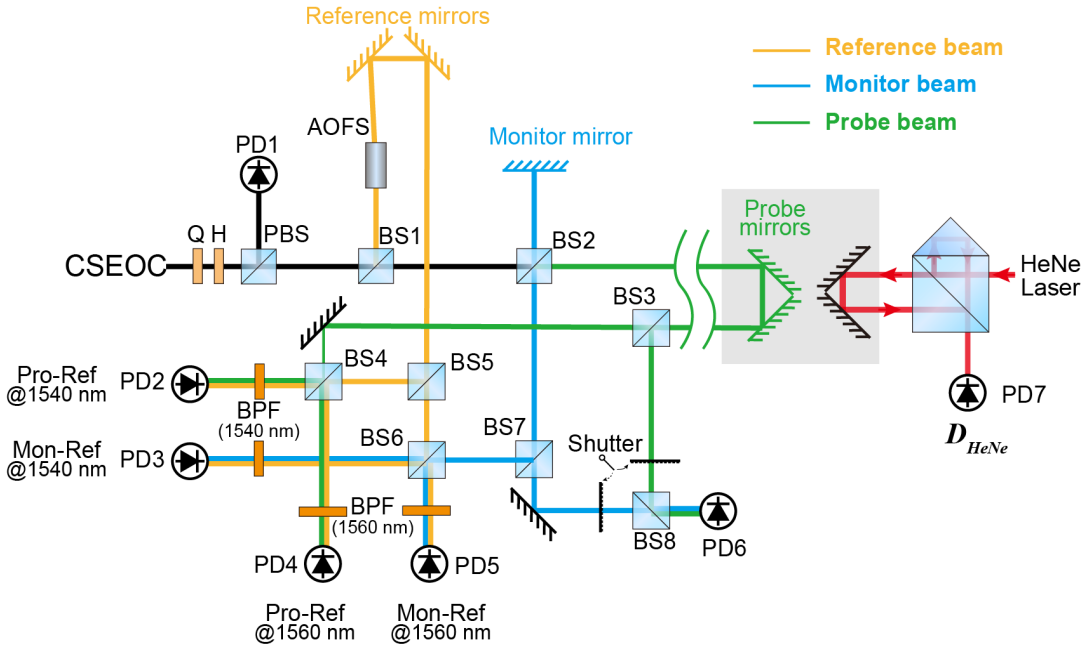

Fig. 5-7 Experimental scheme of distance measurement with monitor arm. CSEOC: coherently synthesized two-color EO comb; Q: quarter waveplate; H: half waveplate; PBS: polarizing beam splitter; AOFS: acousto-optic frequency shifter; BS: beam splitter; BPF: band pass filter; PD: photodetector.

There are two ways to detect the phase of these heterodyne signals, as illustrated in Fig. 5-8. On the one hand, the phase difference (φ_1) between the pair of heterodyne signals that contributed by comb modes near 1560 nm is detected by a lock-in amplifier (SRS,844), as shown in Fig. 5-8 (a). The phase difference (φ_2) between another pair of heterodyne signals that contributed from comb modes near 1540 nm is obtained by the second lock-in amplifier. Therefore, two optical distances, D_{p1} and D_{p2}, are obtained according to φ_1 and φ_2, respectively. Here D_{p1} and D_{p2} are the measured distance from two single wavelength interferometers at 1560 nm and 1540 nm. Then, D_g is obtained according to equation (2-12), where $\Phi = \varphi_1 - \varphi_2$. On the other hand, the synthetic phase (Φ) could be directly measured by detecting the phase difference between two heterodyne signals that contributed by probe beam and reference beam, as shown in Fig. 5-8 (b).

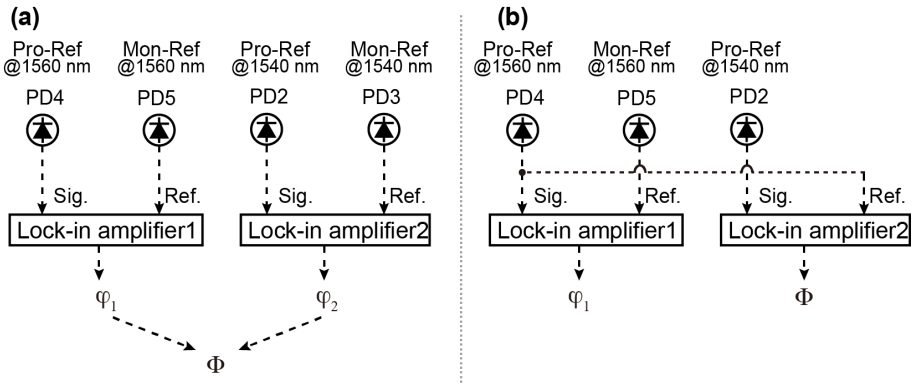

Fig. 5-8 Two configurations to detect the phase of the heterodyne signals. PD2 detects the heterodyne signal at 1540 nm between reference beam and probe beam. PD3 detects the heterodyne signal at 1540 nm between reference beam and monitor beam. PD4 detects the heterodyne signal at 1560 nm between reference beam and probe beam. PD5 detects the heterodyne signal at 1560 nm between reference beam and monitor beam.

The advantage of the second configuration is that the measurement error is smaller. Assume the measurement error of φ_1 and φ_2 are σ_1 and σ_2, respectively. The measurement error of Φ is $\sqrt{\sigma_1^2+\sigma_2^2}$ in the first configuration, while is $\sqrt{\sigma_1^2-\sigma_2^2}$ in the second configuration. Considering that the accuracy and precision of D_g measurement is quite important to estimate the integer of the D_p, the second configuration is applied in the following measurement and analysis.

Besides the single wavelength interferometry and synthetic wavelength technique, microwave phase detection is also employed for distance measurement in order to further extent NAR. 10 % power of the probe beam and 10 % power of the monitor beam are extracted by BS3 and BS7, respectively. The extracted two beams are combined at BS8 and coupled into a piece of single-mode fiber. Two shutters are placed before BS8. Therefore, either monitor beam or probe beam is detected by PD6 (Newport, 1414). To measure the phase of the fundamental repetition frequency, the detected signal is down-converted to 10 MHz by mixing with a 10.01-GHz sinusoidal signal, as shown in Fig. 5-9. This sinusoidal signal comes from a RF synthesizer that is also referenced to the 10 MHz GPS-disciplined clock. In the same manner, the signal from PD1 is also down-converted by mixing with the same sinusoidal signal. The two down-converted signals are band-pass filtered, amplified and connected to the phase meter (HP 8508A). The phase resolution of the phase meter (HP 8508A) is 0.03 degree. In the experiment, the microwave phase detection is implemented by two steps. First, the probe beam is blocked by the shutter and only the monitor beam is detected by the PD6. The phase is recorded by the phase meter. Then the monitor

beam is blocked and only the probe beam is detected by PD6. The phase is recorded again. The distance (D_m) is calculated from the phase difference in the two measurements.

The picture of this setup is shown in Fig. 5-10.

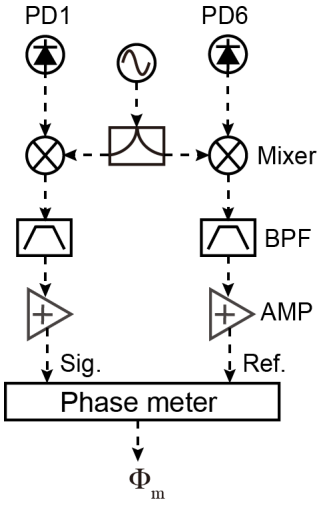

Fig. 5-9 Electrical components for microwave phase detection.

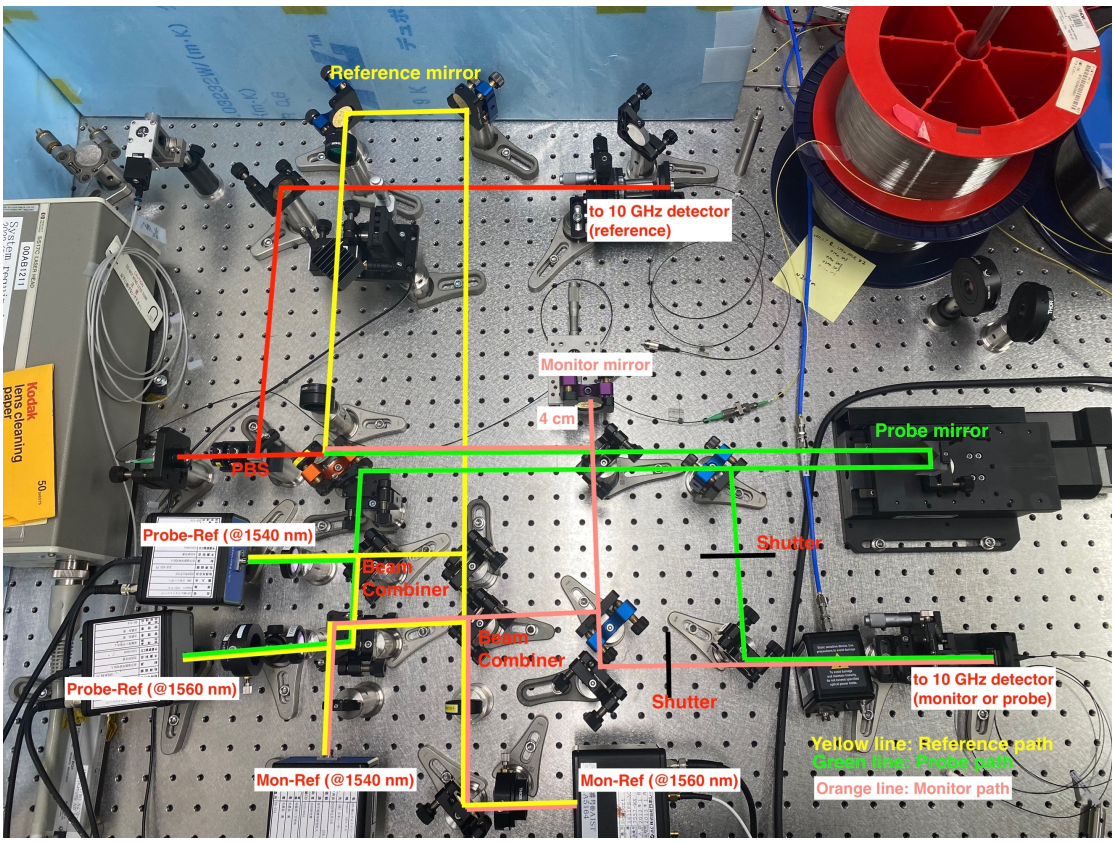

Fig. 5-10 Photo of the experimental setup

5.2.2 Advantage of introducing monitor arm

The advantage of introducing the monitor arm is illustrated in this section [2]. The scheme of the two lock-in amplifiers is shown in Fig. 5-11. The reference signals of the two lock-in amplifiers are both 165-MHz sinusoidal signals. The output of the PD4 and PD2 is connected to the signal ports of lock-in amplifier 1 and lock-in-amplifier 2, respectively. As a result, the path length difference between the monitor arm and reference arm is obtained, as well as the path length difference between the probe arm and the reference arm. The measurement results are labeled as $D_{pro-ref}$ and $D_{mon-ref}$, respectively.

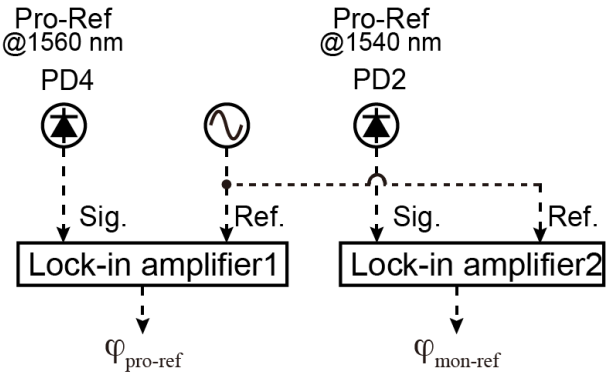

Fig. 5-11 Configuration of lock-in amplifiers.

The measurement is recorded for 10 hours, as shown in Fig. 5-12. Because of the thermal effects of AOFS in reference arm, both $D_{pro-ref}$ and $D_{mon-ref}$ change rapidly in the first two hours. The upper inset shows zoom-in of the path length fluctuation in the first 6 minutes after the system is powered on. The monitor arm is stabilized earlier than the probe arm, since the monitor arm is located closer to the reference arm. According to Fig. 5-12, it takes several hours to fully stabilize the air environment around the system because of the low coefficient of thermal expansion of air.

The lower inset shows zoom-in of the path length variation in 8-10 h. Both $D_{pro-ref}$ and $D_{mon-ref}$ indicate period variation, which is attributed to the air conditioning and ventilation system. The difference between $D_{pro-ref}$ and $D_{mon-ref}$ is much smaller than the amplitude of the period variation.

From Fig. 5-12, it is found that the path length fluctuation of the reference arm and the length fluctuation due to air flow can be partially compensated by introducing the monitor arm. This is one of the advantages of introducing the monitor arm. The

other advantage of having monitor arm is that further non-ambiguity range extension is realized through microwave phase detection. More importantly, the zero point of the absolute distance measurement is set by the monitor arm rather than by reference arm, since the path length of reference arm is canceled out. In other words, the distance measurements based on the three methods share the same zero point, which is very important for absolute distance measurement.

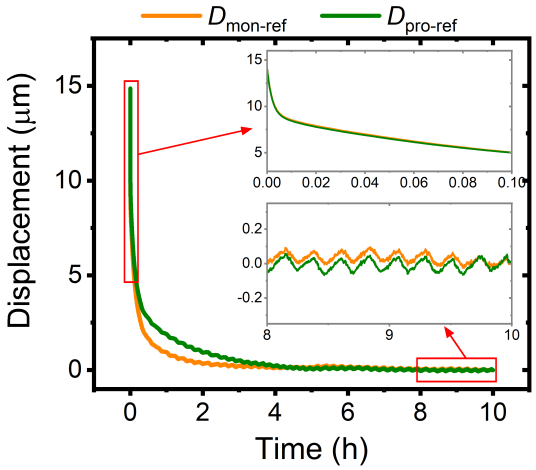

Fig. 5-12 Path length fluctuation in the first 10 hours after the system is turned on. This indicates that the path length fluctuation of the reference arm and the length fluctuation due to air flow can be partially compensated by introducing the monitor arm. Orange curve: the relative path length fluctuation between the monitor arm and reference arm. Green curve: the relative path length fluctuation between the probe arm and reference arm. Upper and lower inset: zoom-in of $D_{pro-ref}$ and $D_{mon-ref}$ in 0-0.1 h and 8-10 h, respectively.

5.2.3 Short-term stability and long-term stability of D_p, D_g, D_m

Similarly to Section 4.2.3, the short-term stability and long-term stability of D_p, D_g and D_m are investigated.

For the short-term stability, the fluctuations of D_p, D_g and D_m within 50 s are shown in Fig. 5-13 (a). The update rate is 10 kHz. The D_p and D_g have same drifting tendency. The D_m fluctuates between $\pm$ 10 μm. Obviously, from D_m to D_g and D_p, the resolution increases. The Allan deviation of D_p, D_g and D_m are given in Fig. 5-13 (b). The Allan deviation of D_p reaches the minimum value, 0.05 nm, at 10 ms averaging time. The increase of the Allan deviation at around 1 ms averaging time is attributed to the system acoustic noise. Due to environmental

drifting, the Allan deviation of D_p increase at longer averaging time. At 1 s averaging time, the Allan deviation of D_p is 2 nm, which is one order of magnitude better than that in Fig. 5-2. This indicates the advantages of introducing monitor arm. The Allan deviation of D_g gradually decreases and then increases with the averaging time. The Allan deviation of D_m gradually decreases. Eventually, the Allan deviation of D_p, D_g and D_m will converge at longer averaging time.

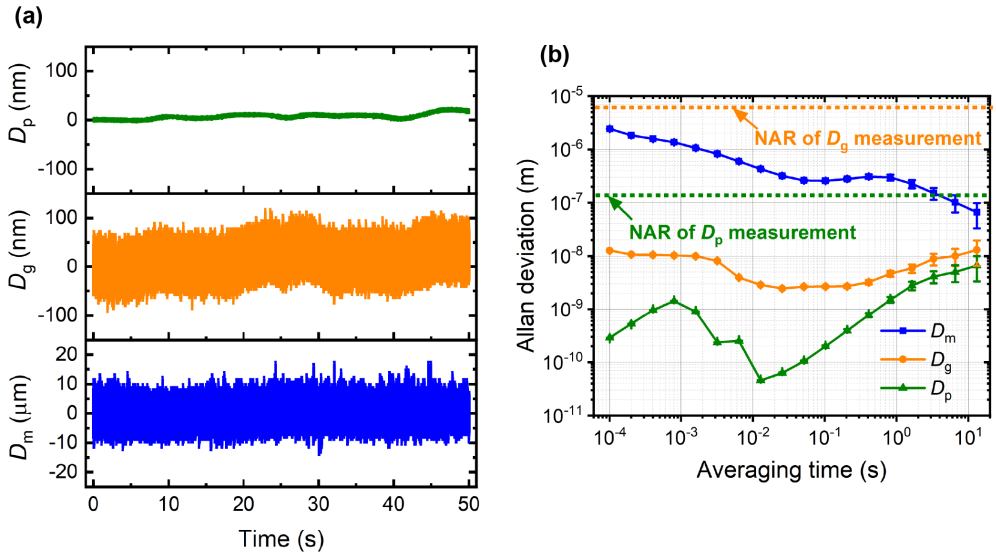

Fig. 5-13 Short-term stability of D_p, D_g and D_m. (a): Original data. (b) Allan deviation of D_p, D_g and D_m.

To investigate the long-term stability, the update rate is set to 100 Hz. The fluctuations and Allan deviation of D_p, D_g and D_m within 40 min are shown in Fig. 5-14. These Allan deviation decreases and then increases as the averaging time increases, attributing to white noise and random environmental drifting respectively. In long averaging time, the three curves gradually converge. It's worth to note that the Allan deviation in Fig. 5-13 (b) and Fig. 5-14 (b) matches with each other from 10 ms to 1 s averaging time. This indicates the reliability of the experimental results.

According to the short-term stability and long-term stability, it is found that the resolution of D_m is higher than the non-ambiguity range of D_g. The resolution of D_g is also higher than the non-ambiguity range of D_p. This means that it is possible to determine the integer of precise measurement from coarse measurement, which is the prerequisite for absolute distance measurement.

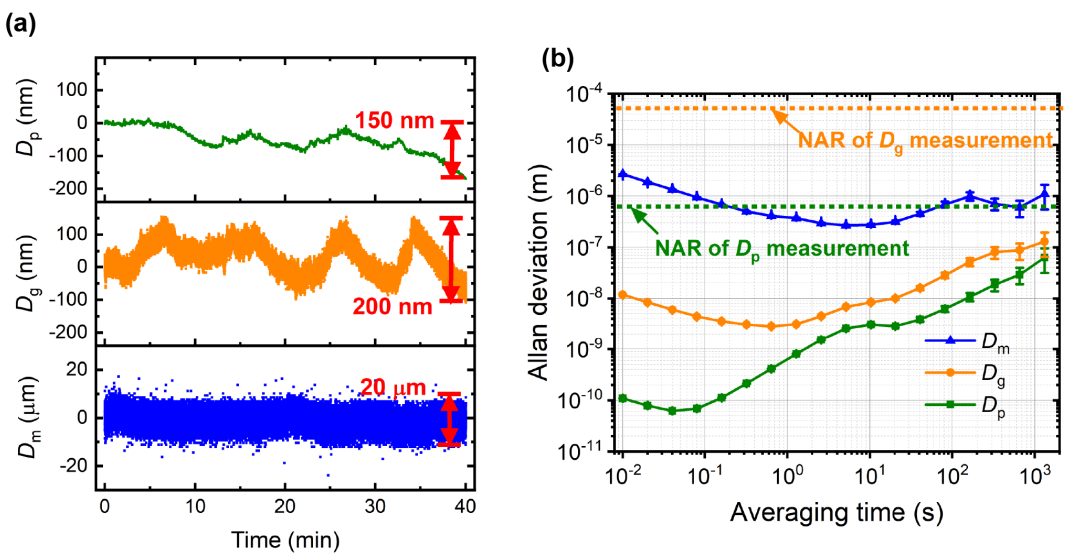

Fig. 5-14 Long-term stability of D_p, D_g and D_m. (a): Original data. (b) Allan deviation of D_p, D_g and D_m.

5.2.4 Linearity

Linearity of D_p. The linearity of D_p is investigated and compared with that from HeNe interferometer, as shown in Fig. 5-15. During the measurement, the probe mirrors are moved at a speed of 20 μm/s. The measured D_p from unwrapped phase is shown as the black curve in Fig. 5-15 (a). The linear fit of D_p is displayed as the red curve, which is downward shifted for clarity. The residual between the measured D_p and its linear fit is within $\pm$ 300 nm, as the orange curve in Fig. 5-15. The residual between the measured D_{HeNe} and its linear fitting is displayed as the green curve. Apparently, the residuals of D_p and D_{HeNe} have same shape. This indicates that the nonlinear moving of the motorized stage is the main reason for the residuals.

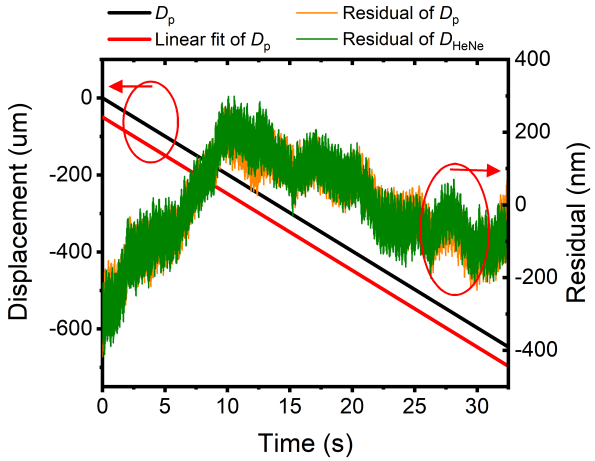

Fig. 5-15 Linearity of D_p. Black curve: measured D_p. Red curve: linear fit of D_p, which is downward shifted for clarity. Orange curve: residual of D_p between the measured data and linear fit. Green curve: residual of D_{HeNe} between the measured data and its linear fit.

The FFT spectra of the residuals is shown in Fig. 5-16 (b). The D_p and D_{HeNe} are both affected by system acoustic noise and resonance of the stage. Due to the alternating current (AC) servo of the motorized stage, the stage resonances at some frequencies. In this case, the resonance at 320-Hz frequency is very strong. The resonance frequencies change at different moving speeds of the stage. For example, the resonance frequencies are integers of 20 Hz when the moving speed is 20 μm/s. The resonance frequencies may vary a lot with different motorized stages.

From the orange curve in Fig. 5-16, it is found that there is cyclic error in the measurement of D_p, which is emphasized by red circles. The frequency of cyclic error is 25.8 Hz, which agrees well with the theoretical value of $2v/\lambda = 2 \times 20/1.56\,Hz \approx 25.64\,Hz$. Here, v and λ are the moving speed of probe mirrors and the center wavelength of the comb modes that contributes the heterodyne signal, respectively. The second harmonic of cyclic error is visible in Fig. 5-16, with frequency of 51.7 Hz. The intensity of the second harmonic of cyclic error is much weaker than the fundamental harmonic. By digitally bandpass filtering the residual of D_p, only the influence of cyclic error is remained, as illustrated in Fig. 5-17. The cyclic error of D_p is within $\pm$ 1.6 nm, which is much smaller than the acoustic noise and the resonance of the stage. In this system, there are two main reasons that contribute the cyclic error: 1) the electromagnetic contamination due to the driven signal of AOFS, as already demonstrated in Section 4.2.4; 2) limited optical density of

the bandpass filters located before photodetectors. The optical density of the bandpass filters utilized here (Thorlabs, FBH1540-12 and FBH1560-12) is around 6. Two bandpass filters are cascaded before PD2 to PD5 in order to increase the optical density. As a result, the cyclic error due to limited optical density is negligible compared to the cyclic error due to electromagnetic contamination in this system.

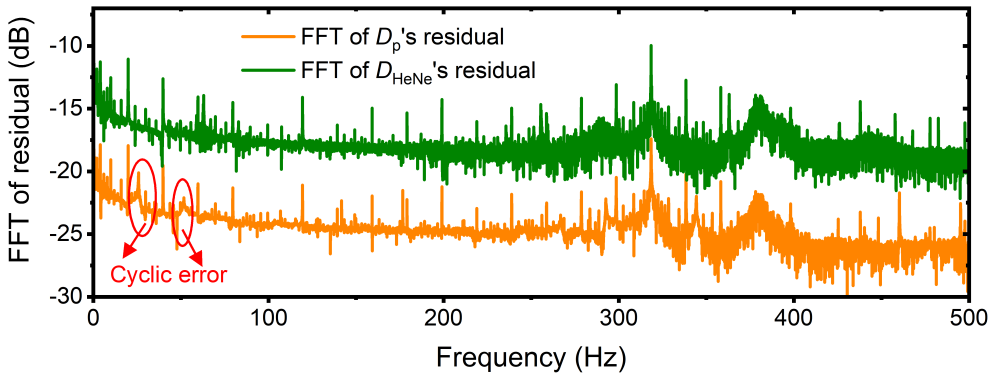

Fig. 5-16 FFT spectra of D_p's residual (orange curve) and D_{HeNe}'s residual (green curve).

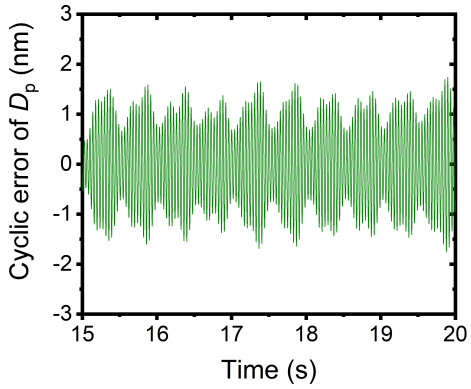

Fig. 5-17 Cyclic error of D_p.

Linearity of D_g. The linearity of D_g measurement is displayed in Fig. 5-18. The black curve and the red curve are the measured D_g and its linear fit. The residual between them is displayed as the green curve. The residual increases at the beginning and the end of the movement. This is attributed to the reduction of power of the heterodyne signals. The cyclic error of D_g is shown in Fig. 5-18 (b), which is obtained by digitally bandpass filtering the residual of D_g. The amplitude of the cyclic error is 270 nm, indicating well agreement with the theoretical value of $1.6\times2\times120/1.56\approx246$ nm. This theoretical value is calculated according to the magnification factor of $2\times\Lambda/\lambda$ and the cyclic error of D_p.

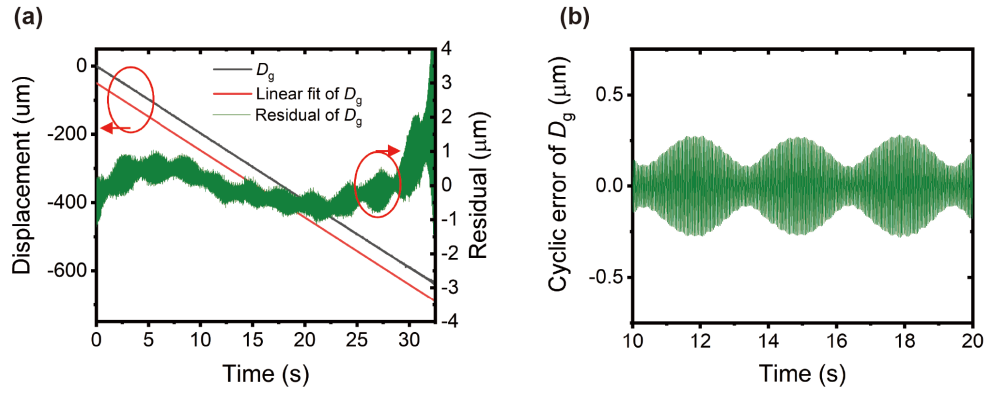

Fig. 5-18 (a): Linearity of D_g measurement. Black curve: measured D_g. Red curve: linear fit of D_g, which is downward shifted for clarity. Green curve: residual of D_g between the measured data and linear fit. (b): Cyclic error of D_g.

The performances of the three methods are listed in Table 2, including Allan deviation, cyclic error and the non-ambiguity range. Although the phase resolution of HP 8508A that utilized in microwave phase detection is 0.03 degree, the Allan deviation of 0.5 μm at 1 s averaging time is realized through average. By using the three methods to measure the same under-test distance, high precision with extended non-ambiguity range is achievable.

Table 2 Performances of distance measurement using the three methods

Methods	Allan deviation (1s averaging time)	Cyclic error (Amplitude)	Non-ambiguity range
Single wavelength interferometry	0.8 nm	1.6 nm	780 nm
Synthetic wavelength technique	5 nm	270 nm	60 μm
Microwave phase detection	0.5 μm	Not investigated	15 mm

5.2.5 Absolute distance measurement

By combining the single-wavelength interferometry, synthetic-wavelength interferometry and microwave phase detection, absolute distance measurement with extended non-ambiguity range and high precision is achieved. In this measurement, the probe mirrors move 600 μm with 25 μm per step. The measurement update rate is

10 kHz. The measurement results are compared with that from the HeNe interferometer, as shown in Fig. 5-19. Each data is the mean value of 10,000 measurement results. The measurement is repeated for three times, as the black, red and green curves shown. The measurement results indicate high linearity between HeNe interferometer and the home-made system with a correlation factor of $R^2 > 0.99999$. The residual between the HeNe interferometer and the home-made system is within $\pm$ 25 nm. This indicates the high reproducibility and high accuracy of this system. It's worth to note that the difference between measured data and that from HeNe interferometer is compared in Fig. 5-19, while the measured data and its linear fit is compared in Fig. 5-15. This difference explains why the residual in Fig. 5-15 is much larger than the residual in Fig. 5-19. Thus the measurement results in Fig. 5-19 is in consistent with that in Fig. 5-15.

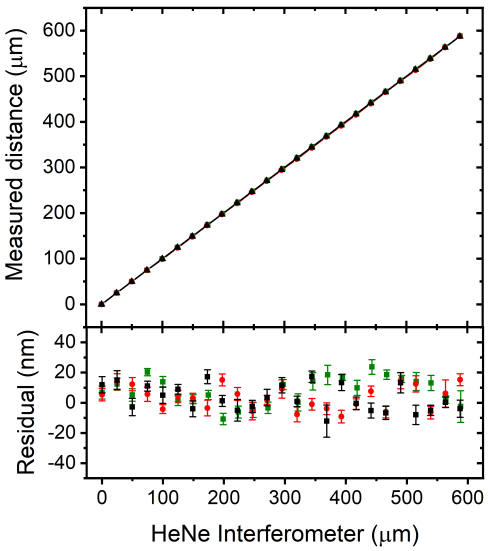

Fig. 5-19 Experimental results of the absolute distance measurement with comparison of a commercial HeNe laser interferometer. Black curve, red curve and green curve correspond to three independent measurements, respectively.

5.3 Summary of this chapter

In this chapter, two distance measurement systems are constructed based on free space interferometer and CSEOC. The measurement performances of the first system are investigated, including the stability and resolution. The cyclic error that induced

by electromagnetic contamination is also studied. By separating the optical part and electrical part in the system, this cyclic error is greatly reduced.

Different from the first system, a monitor arm is introduced to the second system. Through introducing the monitor arm, not only the length fluctuation of the reference arm is able to be measured in real time, but also the microwave phase detection could be applied to extend the non-ambiguity range. As a result, the resolution is improved by ten times comparing to that in the first system. The non-ambiguity range is extended to 15 mm. After investigating the linearity, short-term and long-term stability, absolute distance measurement is implemented. The measurement results are compared with a commercial HeNe interferometer. The difference between them is within ± 25 nm. As a result, an absolute distance measurement system with ultrahigh precision in extended non-ambiguity range is realized. This system could be applied to LIDAR, manufacturing, three dimensional profilometry, and so on.

5.4 References

[1] G. Wu, K. Arai, M. Takahashi, H. Inaba, and K. Minoshima. High-accuracy correction of air refractive index by using two-color heterodyne interferometry of optical frequency combs[J]. Measurement Science and Technology, 2012, 24(1): 015203.

[2] G. Wu, M. Takahashi, K. Arai, H. Inaba, and K. Minoshima. Extremely high-accuracy correction of air refractive index using two-colour optical frequency combs[J]. Scientific Reports, 2013, 3(1): 1-6.

Chapter 6. Summary and outlook

6.1 Summary

In this thesis, a low-noise broadband coherently synthesized two-color EO comb is proposed and applied in absolute distance measurement. In the coherently synthesized two-color EO comb, the accumulated phase noise that is induced by the electrical fields applied to EO modulators is effectively suppressed. Spectrum range of 60 nm is achieved in the coherently synthesized two-color EO comb. Considering the high comb mode power and high repetition rate of the coherently synthesized two-color EO comb, the coherently synthesized two-color EO comb is a perfect optical source to realize absolute distance measurement. Measurement precision of ± 25 nm is achieved in the extended non-ambiguity range.

The research work in this thesis is concretely summarized as follows:

1. The generation of EO combs and compression of pulses from an EO comb are numerically simulated. This simulation provides great guidance to experiment. Low noise coherently synthesized two-color EO combs are demonstrated. Two steps are required to generate the coherently synthesized two-color EO comb: obtain two EO combs with distinct center wavelength and coherent synthesize them. It is found that the accumulated phase noise of the comb modes is greatly suppressed. Then a broadband coherently synthesized two-color EO comb with center wavelength of 1535 nm and 1560 nm is constructed. The spectrum range reaches 60 nm after spectrum broadening. Finally, the optical devices in the two-color EO comb are integrated into an aluminum box.

2. The previously demonstrated coherently synthesized two-color EO comb is applied to absolute distance measurement. A fiber type interferometer is constructed for distance measurement. The measurement error is investigated, including the dead path error, the cyclic error and the measurement error induced by acoustic noise. The short-term stability, long-term stability and linearity of the system are also studied, revealing the resolution of static measurement and the capability of dynamic measurement. Absolute distance measurement and fast displacement measurement with 10-kHz update rate are realized. However, in this distance measurement system

based on fiber type interferometer, the dead path error that due to fiber length fluctuation prevents the measurement with < 100 nm precision in > s averaging time. To deal with this issue, distance measurement with free space interferometer is preferred.

3. An absolute distance measurement based on free space interferometer is constructed. In this system, a third arm, named monitor arm, is introduced. By comparing the performance with and without the monitor arm, it is found that the length fluctuation of the reference arm and length fluctuation induced by air flow is partly compensated when the monitor arm is introduced, resulting in better measurement precision. Three methods, including single wavelength interferometry, synthetic wavelength technique and microwave phase detection, are utilized to measure the distance under test simultaneously, from precise measurement to coarse measurement. Therefore, nanometer precision in extended non-ambiguity range is realized. Through comparing the measurement results with those from a commercial HeNe interferometer, residual of less than ±25 nm is achieved.

6.2 Outlook

The outlooks of this work mainly include the following points:

1. Although the coherently synthesized two-color EO comb is constructed, there is a frequency offset between the comb modes from the two combs. In the future, some efforts could be made to realize offset free coherently synthesized two-color EO comb. This could be realized by two steps. Firstly, the frequency offset between the two EO combs should be zero. There are some methods to realize this. For example, frequency shift one of the EO combs and then phase lock the beat frequency to the shifted frequency. Secondly, the phase of the comb modes with same frequency should be the same. This could be achieved through inserting a delay line in the optical path of one comb. The length of the delay line should be locked according to the phase difference between the comb modes with same frequency.

2. In the absolute distance measurement system demonstrated in Chapter 5, the dead zone is an issue. Only when the pulses from the probe arm overlap with the pulses from the reference arm, the distance under test could be measured. This means the dead zone is large. Some methods could be applied to decrease the dead zone. For instance, one can link the repetition rate of the EO comb to the distance under test. In

this case, the repetition rate changes according to the distance under test. As a result, the distance under test could be read out from the repetition rate. As long as the path length between the probe arm and reference arm is larger enough, dead zone disappears.

3. The coherently synthesized two-color EO comb is well suitable to be used as astrocombs in the future, attributing to the high repetition rate, high power per mode and broad spectrum. By utilizing the coherently synthesized two-color EO comb as optical source, high precision and accuracy distance and velocity measurement can be realized. This enables hunting for exoplanets by radial velocity method, as well as detecting cosmic acceleration. Besides, astronomical spectrograph calibration can be implemented by high accuracy spectroscopy based on coherently synthesized two-color EO comb and dual-comb technique.

4. The coherently synthesized two-color EO comb is also well suitable to many other applications, like THz wave generation, non-contact measurement, optical communication, etc. Taking the THz wave generation as an example, the generation efficiency of THz wave could be high benefiting from the high power per mode in the coherently synthesized two-color EO comb. Meanwhile, the wavelength of the THz wave could be tuned by adjusting the center wavelengths of the coherently synthesized two-color EO comb. It would be wonderful to apply the generated THz wave to imaging, spectroscopy, non-destructive testing, and so on.

List of Publications

Journal papers：

[1] **Runmin Li**, Haochen Tian, Takashi Kato, Akifumi Asahara and Kaoru Minoshima, Coherently synthesized two-color electro-optic frequency combs with phase noise suppression. **Applied Physics Express**, 2023, 16, 012005.

[2] **Runmin Li**, Haochen Tian and Kaoru Minoshima, Reduction of cyclic error induced by electromagnetic contamination in an EO-comb based distance measurement system. **Results in Optics**, 2022, 9, 100308.

[3] Haochen Tian, **Runmin Li**, Takeru Endo, Takashi Kato, Akifumi Asahara, Lukasz A. Sterczewski and Kaoru Minoshima, Dual-comb spectroscopy using free-running mechanical sharing dual-comb fiber lasers[J]. Applied Physics Letters, 2022, 121(21): 211104.

[4] Haochen Tian, **Runmin Li**, Lukasz A. Sterczewski, Takashi Kato, Akifumi Asahara and Kaoru Minoshima, Quasi-real-time dual-comb spectroscopy with 750-MHz Yb: fiber combs[J]. Optics Express, 2022, 30(16): 28427-28437.

[5] Yihan Pi, Haochen Tian, **Runmin Li**, Youjian Song, and Minglie Hu. Timing jitter and intensity noise characterization of a 122-MHz all-PM NALM mode-locked laser [J]. IEEE Photonics Technology Letters, 2021, 33(24): 1439.

International Conferences：

[1] **Runmin Li**, et al. High Precision and Extended Non-ambiguity Range Absolute Distance Measurement Based on a Coherently Synthesized Two-Color Electro-Optic Frequency Comb[C]. Advanced Lasers and Photon Sources Conference (ALPS). 2023, 25-02.

[2] **Runmin Li**, et al. Absolute distance measurement based on a coherently synthesized two-color electro-optic frequency comb[C]. UFO XIII, 2023.

[3] **Runmin Li**, et al. Distance measurement based on a coherently synthesized two-color EO comb towards air-refractive index self-correction[C]. CLEO-PR, 2022, CThP6F-06.

[4] **Runmin Li**, et al. Low noise coherently synthesized two-color Electro-Optic frequency comb[C]. CLEO: Science and Innovations. 2022: JW3B.98.

[5] **Runmin Li**, et al. Broadband coherently synthesized two-color electro-optic frequency comb[C]. Advanced Lasers and Photon Sources Conference (ALPS). 2022,14-03.

Domestic Conferences:

[1] R. Li, et al. Phase locking of two-color Electro-optic frequency combs generated with common modulators for coherent synthesis[C]. In JSAP-OSA Joint Symposia, 13a_N404_3. Optical Society of America, 2021.

Acknowledges

I would like to take this opportunity to express my deepest gratitude and appreciation to all those who have contributed to the completion of this doctoral dissertation. This journey would not have been possible without the invaluable support, guidance, and encouragement from them, and I am profoundly grateful for their contributions.

First and foremost, I would like to extend my heartfelt gratitude to my advisor, Prof. Kaoru Minoshima. Her expertise, patience, and commitment to academic excellence have been instrumental in shaping this research and guiding me towards new insights. Her guidance and mentorship have challenged me to push the boundaries of my knowledge and have greatly contributed to the quality and rigor of this dissertation. Thanks to the support from Prof. Minoshima, I have been fortunate to participate in many academic conferences, which have provided me with valuable opportunities to connect with researchers and receive constructive feedback. I am incredibly grateful for these opportunities that have enriched my academic journey.

I am grateful to my husband, Haochen Tian, who is my research supervisor and an excellent teammate in my life. His insightful discussions, intellectual curiosity, and invaluable feedback have shaped the development of my ideas and strengthened the quality of this dissertation. His ability to offer fresh perspectives and constructive criticism has pushed me to refine my arguments and strive for greater excellence. Throughout my three-year stay in Japan, I really appreciated him cooking for me every day, a gesture that I hold in deep appreciate.

I am immensely grateful to Prof. Thomas R. Schibli. During his two-month visit in UEC, I got a lot of suggestions and comments from him. His expertise and diverse perspectives have greatly enhanced the depth and breadth of this research. I am grateful for his time, dedication, and willingness to share knowledge.

I would like to acknowledge the colleagues and fellow researchers who have shared their insights, provided valuable discussions, and offered their assistance whenever needed. To Takashi Kato-san and Akifumi Asahara-san, I want to appreciate the cooperation with them and the positive feedback provided during the revision of this dissertation. To Prasad Kovori-san, I want to thank his support and fruitful

discussion. To Ruichen Zhu-san, I am very grateful to her life assistance and Japanese support whenever I need. Their collaboration and support have been invaluable in shaping my ideas, strengthening the research outcomes and making my life colorful.

I am immensely grateful to the members of my dissertation committee, Prof. Masayuki Katsuragawa, Prof. Mitsuru Musha, Prof. Eriko Watanabe and Assistant Prof. Akifumi Asahara, for their invaluable insights and constructive feedback throughout the various stages of this research. Their expertise and thoughtful suggestions have greatly enriched the quality and depth of this dissertation.

I am indebted to my family for their unwavering love, encouragement, and unwavering support throughout this journey. Their belief in my abilities and constant motivation have been my driving force. I would not have been complete my PhD study without their support. I am forever grateful for their sacrifices and understanding during the demanding phases of my research.

I would also like to express my sincere appreciation to the faculty and staff at UEC for providing a stimulating academic environment and the necessary resources for my research. The opportunity to engage in discussions, attend seminars, and collaborate with fellow researchers has been an enriching experience, and I am grateful for the support I received from the institution.

Last but not least, I would like to express my heartfelt gratitude to the Japan Society for the Promotion of Science (JSPS) for their generous financial support in daily life and scientific research throughout my doctoral studies. Their funding has played a crucial role in enabling me to pursue my research and achieve my academic goals. I am truly thankful for their unwavering support, which has greatly contributed to the successful completion of my PhD program and has laid a strong foundation for my future endeavors in the field.

In conclusion, I am profoundly grateful to each and every individual who has contributed to the completion of this dissertation. Their support, guidance, and belief in my abilities have been instrumental in achieving this significant milestone. I am truly humbled and honored to have had the privilege of working with such exceptional individuals.

Thank you all!

Runmin Li

July 15th, 2023